Expanding the Toolbox for Positron Emission Tomography

–

Radiotracer Development from PARP to Reporter Genes

Dissertation

der Mathematisch-Naturwissenschaftlichen Fakultät

der Eberhard Karls Universität Tübingen

zur Erlangung des Grades eines

Doktors der Naturwissenschaften

(Dr. rer. nat.)

vorgelegt von

Sophie Stotz

aus Heilbronn

Tübingen

2023

STATEMENT OF ORIGINALITY

Ich erkläre hiermit, dass ich die zur Promotion eingereichte Arbeit mit dem Titel „Expanding the Toolbox for Positron Emission Tomography - Radiotracer Development from PARP to Reporter Genes" selbständig verfasst, nur die angegebenen Quellen und Hilfsmittel benutzt und wörtlich oder inhaltlich übernommene Stellen als solche gekennzeichnet habe. Ich erkläre, dass die Richtlinien zur Sicherung guter wissenschaftlicher Praxis der Universität Tübingen (Beschluss des Senats vom 25.05.2000) beachtet wurden. Ich versichere Eides statt, dass diese Angaben wahr sind und dass ich nichts verschwiegen habe. Mir ist bekannt, dass die falsche Abgabe einer Versicherung an Eides statt mit Freiheitsstrafe bis zu drei Jahren oder mit Geldstrafe bestraft wird.

Tübingen, 2023

SUMMARY

Cancer is a life-threatening disease. Its treatment is challenging due to the disease's heterogenous nature, and there is no universal therapy. In the last decades, different features of cancer have been explored for individualized treatment. One of those attributes is elevated levels of cellular stress, in particular replicative stress, within the tumors. Although treatments targeting replicative stress are available, to date, there is no specific biomarker available for the use with standard-of-care non-invasive imaging methods like position emission tomography utilizing radiolabeled molecules. Thus, therapy approaches are based on *ex vivo* information like histopathology or are applied without functional guidance.

In this work, we evaluated PARP enzymes for their potential as biomarker for replicative stress. PARPs are heavily involved in the repair of single-strand DNA breaks, and their inhibition leads to synthetic lethality in tumor entities that lack alternative repair mechanisms. First, we synthesized five different PARP radiotracers, small molecules radiolabeled with the β^+-emitting isotope ^{18}F, for comparison of their biodistribution in the same mouse model and to determine the best application. We synthesized [^{18}F]FPyPARP, a logD-optimized variant of [^{18}F]PARPi, to shift the clearance route towards renal excretion, as high liver uptake hampers [^{18}F]PARPi application for liver imaging. Compared to the gold-standards [^{18}F]PARPi and [^{18}F]FTT, [^{18}F]FPyPARP presented with improved liver clearance, and might be an alternative to [^{18}F]PARPi for liver imaging. [^{18}F]Olaparib, an isotopologue of the first approved PARP inhibitor olaparib, was synthesized for direct comparison with the 100-fold more effective second-generation isotopologue [^{18}F]talazoparib. The difference in efficacy here is attributed to the improved trapping capacity of PARP on the damaged DNA that prevents replication restart. In a xenograft model, [^{18}F]olaparib and [^{18}F]talazoparib showed similar biodistribution and PARP targeting, suggesting that the PARP trapping capacity does not influence radiotracer performance. In the overall comparison, target engagement was comparable but the radiotracers differed in non-target tissues; Thus, the choice of radiotracer is solely dependent on the envisioned application.

To evaluate PARP as a biomarker for replicative stress, four *in vitro* models were probed for correlation of PARP radiotracer uptake with levels of stress. In myc overexpression models, the results were heterogeneous, and another attempt for a mIDH expression-based cell model did not indicate increased uptake. We then set out to induce replicative stress chemically, and did not observe significant differences in PARP radiotracer uptake compared to controls. We concluded that PARP is not a suitable biomarker as the expression is not upregulated but more likely the protein is activated on an enzymatic level upon replicative stress. Several other potential biomarkers were tested for changes in expression levels with Western blot, but did not result in a clear specific biomarker.

SUMMARY

As a surrogate, we developed novel reporter gene systems to compensate the lack of a specific replicative stress biomarker for preclinical therapy development and research on biomarkers and animal models. A reporter gene could be used to quantify promotor activity or other biological processes that can not be visualized directly. We designed, characterized and evaluated HaloTag, SNAPTag and CLIPTag and novel radiotracers designed to target the respective proteins *in vitro* and *in vivo* in a pilot xenograft study. All three presented with excellent target engagement and favorable pharmacokinetics.

Interestingly, the HaloTag and CLIPTag radiotracers showed unspecific uptake in the naïve rodent brain, indicating that they are able to cross the intact blood-brain barrier. The blood-brain barrier is a recurrent obstacle in brain radiotracer development and thereby hampers global visualization of biological processes. Further evaluation in a murine model of viral gene transfer to the brain confirmed specific brain uptake and paves the way for future applications in the whole body.

Thereby, our novel reporter gene systems are suitable to be used for future development of replicative stress specific radiotracers. The potential to stratify patients according to levels of replicative stress would ultimately aid selecting appropriate therapy regimen, and pave the way for new treatments targeting replicative stress.

ZUSAMMENFASSUNG

Krebs ist eine lebensbedrohliche Erkrankung. Die Behandlung gestaltet sich in den meisten Fällen schwierig, da diese Erkrankung viele unterschiedliche Ausprägungen hat. In den letzten Jahrzehnten wurden verschiedene Eigenschaften von Krebserkrankungen auf ihre Eignung als individualisierbare Therapiemarker untersucht. Eine dieser Eigenschaften ist erhöhter zellulärer Stress, genauer replikativer Stress, in den Krebszellen. Obwohl Therapien zur Verfügung stehen, die spezifisch auf replikativen Stress abzielen, gibt es bis heute jedoch keinen spezifischen Biomarker, der auch für die Anwendung mit standardmäßigen nicht-invasiven Bildgebungsverfahren wie beispielsweise die Positronen-Emissions-Tomographie, welche radioaktive Moleküle benutzt, anwendbar ist. Demnach werden diese Therapiemöglichkeiten aufgrund von *ex vivo* Methoden wie histopathologischen Gutachten oder ganz ohne funktionale Informationen über den Tumor angewendet.

Diese Arbeit dreht sich um die Evaluation von PARP-Enzymen als potenzielle Biomarker für replikativen Stress. PARPs sind stark an der Reparatur von DNA-Einzelstrangbrüchen beteiligt, und ihre Inhibition führt zu synthetischer Letalität in Krebsarten, denen alternative Reparaturmechanismen fehlen. Zunächst haben wir aus Vergleichbarkeitsgründen fünf verschiedene radioaktive Marker für PARP („Radiotracer") synthetisiert, welche mit dem positronenemittierenden Isotop ^{18}F markiert wurden. Ziel hierbei war es, die fünf Radiotracer im gleichen Mausmodell auf ihre Biodistribution hin zu vergleichen und die optimale Anwendung herauszufinden. Als Alternative zu [^{18}F]PARPi, welcher eine hohe Leberaufnahme hat und daher nur eingeschränkt für Leber-Bildgebung verwendet werden kann, haben wir die logD-optimierte Variante [^{18}F]FPyPARP synthetisiert. Im Vergleich mit den „Goldstandards" [^{18}F]PARPi und [^{18}F]FTT zeigte [^{18}F]FPyPARP eine schnellere Leberexkretion, was dafürspricht, dass dieser Radiotracer als Alternative für die Leber-Bildgebung eingesetzt werden könnte. Das Isotopolog [^{18}F]Olaparib, welches auf dem ersten zugelassenen PARP-Inhibitor Olaparib beruht, wurde synthetisiert, um es direkt mit [^{18}F]Talazoparib, welcher ein 100-fach effektiverer PARP-Inhibitor ist, zu vergleichen. Dieser Unterschied in der Wirksamkeit kann durch das deutlich höhere Potenzial von Talazoparib erklärt werden, PARP-Enzyme auf der geschädigten DNA festzuhalten. Dies verhindert, dass die Replikationsgabel neu gestartet werden kann. Im Tumormodell zeigten sich allerdings kaum Unterschiede in der Biodistribution und der Wirkung zwischen den beiden Radiotracern, was darauf schließen lässt, dass die Eigenschaft, PARP-Enzyme auf der DNA festzuhalten, keinen Einfluss auf die Funktion des Radiotracers hat. Im Gesamtvergleich was das Potenzial, PARP-Enzyme zu visualisieren, zwischen allen fünf Radiotracern ähnlich, es gab aber durchaus Unterschiede in der Aufnahme in nicht-relevante Organe. Daher ist die Wahl des geeigneten PARP Radiotracers abhängig von der geplanten Anwendung.

ZUSAMMENFASSUNG

Um die Eignung von PARP-Enzymen als Biomarker für replikativen Stress zu evaluieren wurden vier *in vitro* Modelle verwendet und die Korrelation zwischen der Aufnahme von PARP Radiotracern und replikativem Stress überprüft. In Modellen, die auf myc-Überexpression beruhen, wurden keine eindeutigen Daten erzielt. Auch ein weiteres Modell basierend auf Überexpression von mIDH zeigte keine erhöhte Aufnahme des Radiotracers. Danach wurde der replikative Stress chemisch induziert, allerdings wurde kein signifikanter Unterschied in der Aufnahme von PARP-Radiotracern zwischen den behandelten Zellen und Kontrollzellen beobachtet. Wir schlossen hieraus, dass PARP kein geeigneter Biomarker für replikativen Stress ist, da die Expression nicht ausreichend und zuverlässig hochreguliert ist. Unsere Vermutung ist, dass PARP-Enzyme bei replikativem Stress eher auf einem enzymatischen Level aktiviert anstatt hochreguliert werden. Mehrere andere potenzielle Biomarker wurden mittels Western Blot betrachtet, aber auch hier ergab sich kein eindeutiger Biomarker.

Um den Mangel an einem spezifischen Bildgebungsbiomarker für replikativen Stress für die Entwicklung neuer Therapien sowie präklinischer Forschung auszugleichen, haben wir alternativ neue Reportergen-Systeme entwickelt. Diese Reportergene könnten genutzt werden, um die Aktivität von bestimmten Promotoren, oder andere biologische Prozesse, die nicht direkt visualisiert werden können, zu quantifizieren. In dieser Arbeit haben wir HaloTag, SNAPTag und CLIPTag und die jeweiligen dafür entworfenen Radiotracer entworfen, charakterisiert sowie *in vitro* und in einem *in vivo* Tumormodell evaluiert. Alle drei haben hier exzellente Bindung zum Zielprotein und vielversprechende pharmakokinetische Eigenschaften gezeigt

Interessanterweise haben die Radiotracer für HaloTag und CLIPTag unspezifische Aufnahme in das Gehirn gezeigt, was bedeutet, dass die Radiotracer die Blut-Hirn-Schranke überqueren können. Die Blut-Hirn-Schranke ist ein immer wiederkehrendes Hindernis in der Entwicklung neuer Radiotracer, und verhindert dadurch teilweise die globale Betrachtung biologischer Prozesse. Die weitere Evaluation von HaloTag und CLIPTag in einem Modell des viralen Gentransfers zeigte auch spezifische Gehirnaufnahme der Radiotracer, was den Weg für zukünftige Anwendung unserer Reportergen-Systeme im gesamten Körper ebnet.

Damit sind unsere neuen Reportergen-Systeme mehr als geeignet um die zukünftige Entwicklung von Radiotracern für replikativen Stress zu unterstützen. Das Potenzial, Krebspatienten in Hinsicht auf die Menge an replikativem Stress zu stratifizieren würde die Wahl einer geeigneten Therapieform vereinfachen und schlussendlich den Weg für neue Behandlungsmethoden ebnen, die spezifisch für replikativen Stress sind.

TABLE OF CONTENTS

TABLE OF CONTENTS

LIST OF ABBREVIATIONS

2-HG	2-hydroxyglutarate
53BP1	53 binding protein 1
AAV	adeno-associated virus
AGT	O^6-alkylguanine-DNA alkyltransferase
ANOVA	analysis of variance
AP	anteroposterior
APOBEC	apolipoprotein B mRNA editing enzyme, catalytic polypeptide
ATF6	activating transcription factor 6
ATM	ataxia telangiectasia mutated
ATP	adenosine triphosphate
ATR	ataxia telangiectasia mutated and Rad3-related
BAK	Bcl-2 homologous antagonist/killer 1
BAX	Bcl-2 associated X protein
BBB	blood-brain barrier
BER	base excision repair
BC	benzylcytosine
BG	benzylguanine
BiP	binding-immunoglobulin protein
BP_{ND}	non-displaceable binding potential
BRCA	breast cancer
CAR	chimeric antigen receptor
CHK1	checkpoint kinase 1
CPT	camptothecin
CT	computed tomography
DAPI	4',6-diamidino-2-phenylindole
dCK	deoxycytidine kinase
DCM	dichloromethane
DDR	DNA damage response
DGC	DABCO-guaninyl chloride
DHFR	dihydrofolate reductase
DMEM	Dulbecco's modified Eagle medium
DMI	1,3-dimethyl-2-imidazolidinone
DMSO	dimethylsulfoxide
DNA	deoxyribonucleic acid
DNA-PK	DNA protein kinase
DoE	design of experiments

LIST OF ABBREVIATIONS

DSB	double-strand break
DV	dorsoventral
eIF2α	eukaryotic translation initiation factor 2 α
EMT	epithelial-mesenchymal transition
ER	endoplasmatic reticulum
EGFR	epidermal growth factor receptor
ESI-MS	electrospray ionization mass spectrometry
EtOH	ethanol
FAC	1-(2′-deoxy-2′-fluoroarabinofuranosyl) cytosine
FAP	fibroblast activated protein
FBBG	*N*-(4-(((2-amino-9*H*-purine-6-yl)oxy)methyl)benzyl)-4-fluorobenzamide
FB-HTL	fluorobenzoyl-HaloTag ligand
FCS	fetal calf serum
FDA	food and drug administration
FDG	2-deoxy-2-fluoro-D-glucose
FHBG	9-(4-fluoro-3-hydroxymethylbutyl)guanine
FIAU	2'-deoxy-2'-fluoro-1-beta-D-arabinofuranosyl-5-iodouracil
FPyTFP	2,3,5,6-tetrafluorophenyl 6-fluoronicotinate
FTT	fluorthanatrace
GLS	glutaminase
GLUT1	glucose transporter 1
GLS	glutamine synthase
GPx	glutathione peroxidase
GTP	guanosine triphosphate
HEK	human embryonic kidney
HLB	hydrophilic lipophilic balance
HPLC	high performance liquid chromatography
HR	homologous recombination
HSV1-tk	*herpes simplex viru*s type 1 thymidine kinase
HTL	HaloTag ligand
HU	hydroxyurea
i.c.	intracranial
IDH	isocitrate dehydrogenase
IF	immunofluorescence
i.p.	intraperitoneal
IRE1α	inositol-requiring enzyme 1α
i.v.	intravenous

LIST OF ABBREVIATIONS

MeCN	acetonitrile
MeOH	methanol
*m*FBG	6-((3-fluorobenzyl)oxy)-9*H*-purine-2-amine
mIDH	mutant isocitrate dehydrogenase
MARylation	mono(ADP-ribosyl)ation
ML	mediolateral
MR	mismatch repair
MRI	magnetic resonance imaging
MRN	MRE11/RAD50/NBS1
NER	nucleotide excision repair
NAD$^+$	nicotinamide adenine dinucleotide
NHEJ	non-homologous end joining
NIS	sodium iodide symporter
NMR	nuclear magnetic resonance
OATP	organic anion transporting polypeptide 1B3
OE	overexpression
OSEM3D	ordered subset expectation maximization 3D
PAR	poly(ADP-ribose)
PARG	poly(ADP-ribose) glycohydrolase
PARP	poly(ADP-ribose) polymerase
PARylation	poly(ADP-ribosyl)ation
PBS	phosphate-buffered saline
PDAC	pancreatic ductal adenocarcinoma
PDGFR	platelet-derived growth factor receptor
PD-L1	programmed cell death-ligand 1
PERK	protein kinase R-like ER kinase
PET	positron emission tomography
*p*FBC	6-((4-fluorobenzyl)oxy)-9*H*-pyrimidine-2-amine
*p*FBG	6-((4-fluorobenzyl)oxy)-9*H*-purine-2-amine
PgP	P-glycoprotein
p.i.	post injection
PKM2	pyruvate kinase M2
PSMA	prostate-specific membrane antigen
RAS	rat sarcoma viral oncogene homolog
RGS	reporter gene system
RPA	replication protein A
RPMI	Roswell Park Memorial Institute

LIST OF ABBREVIATIONS

ROI	region of interest
ROS	reactive oxygen species
SASP	senescence-associated secretory phenotype
s.c.	subcutaneous
SD	standard deviation
SDS-PAGE	sodium dodecyl sulfate polyacrylamide gel electrophoresis
SFB	*N*-succinimidyl 4-fluorobenzoate
SOD	superoxide dismutase
SSB	single-strand break
SUV	standardized uptake value
TAC	time-activity curve
TCA	tricarboxylic acid
TCEP	tris-(2-carboxyethyl)-phosphine
TFA	trifluoroacetic acid
TGF-β	transforming growth factor β
TLC	thin layer chromatography
TME	tumor microenvironment
TNBC	triple negative breast cancer
TNF	tumor necrosis factor
TNKS	tankyrase
UPR	unfolded protein response
UV	ultraviolet
VEGF	vascular endothelial growth factor
VOI	volume of interest
XBP1	X-box binding protein 1

ACKNOWLEDGEMENTS

ACKNOWLEDGEMENTS

and advice. This was the first lab I worked in, and this is part of the reason I am where I am now. Also, I would like to thank Prof. Dr. Robert Feil for his support, who is part of my scientific career since my Master internship in his lab, as my second supervisor for my Master Thesis and now my PhD Thesis.

This work is dedicated to my family.

My family by blood, my parents, grandparents and brother. I would not have been able to achieve this without them, and they all were part of who I am now. Thank you for your understanding, your support, and for always being there for me.

My family by mind, my partner in crime, my best friends. I want to thank my partner Andreas in particular, for enduring 'stressed me', and supporting me in every aspect. Thank you for being you, for always seeing the positive, and for encouraging me to follow my dreams.

A successful woman once said, doing science is better when you work with your besties. I am very grateful that I worked together with Vera Jörke, who was always there for me and with whom I share many fond memories inside and outside the lab. Greg Bowden and Gina Dunkel were a big part of my life also outside of the lab, and I am thankful that . You were always there for me, scientifically and personally, and without you, the lab/Obergurgl/conferences/private life/.. wouldn't have been so much fun.

There are many more people who were part of this journey, and I am only able to name the most impactful ones. I would like to end the acknowledgements with a quote from my favorite book series, which was a way to wind down after a stressful week. The quote is a motivation for my future career, for which I hope I will have as amazing colleagues and friends as I had for my PhD Thesis.

Dream big, idiot.

\- Hoid, Stormlight Archives, Brandon Sanderson

1. INTRODUCTION

Personalized medicine utilizing non-invasive imaging methods is a game-changer for both patients and clinicians. In particular, this is crucial for cancer therapy as cancer is a highly heterogenous disease requiring different treatments for different cancer types. The introduction to this work aims to outline the current advances in cancer therapy, the need for specific imaging biomarkers in regard to replicative stress, a promising therapeutic target, and potential workaround strategies, with methodological focus on radiotracer development and positron emission tomography (PET).

1.1 Cancer and Cancer Treatment

Cancer is a life-threatening disease with many faces and affects millions of people world-wide. Many types of cancer have a good prognosis if detected early but a substantial amount require long-term treatment affecting overall health and still have poor outcomes. In the last decade, there were huge efforts towards personalized medicine, with the cancerous lesion being characterized extensively before choosing the appropriate treatment regimen. Although cancer was thought of as a simple mass of fast and unregulated growing cells, it is a complex system of different aberrant pathways and, more specifically, dysregulated metabolism.[1,2] Still, cancers generally share some common features, also referred to as the hallmarks of cancer. In early 2000, Hanahan and Weinberg defined six hallmarks to categorize the processes needed for healthy cells to transform to malignant cells: Self-sufficiency in growth signals and insensitivity to anti-growth signals, evading apoptosis, sustained angiogenesis, unlimited replicative potential, and tissue invasion and metastasis.[3]
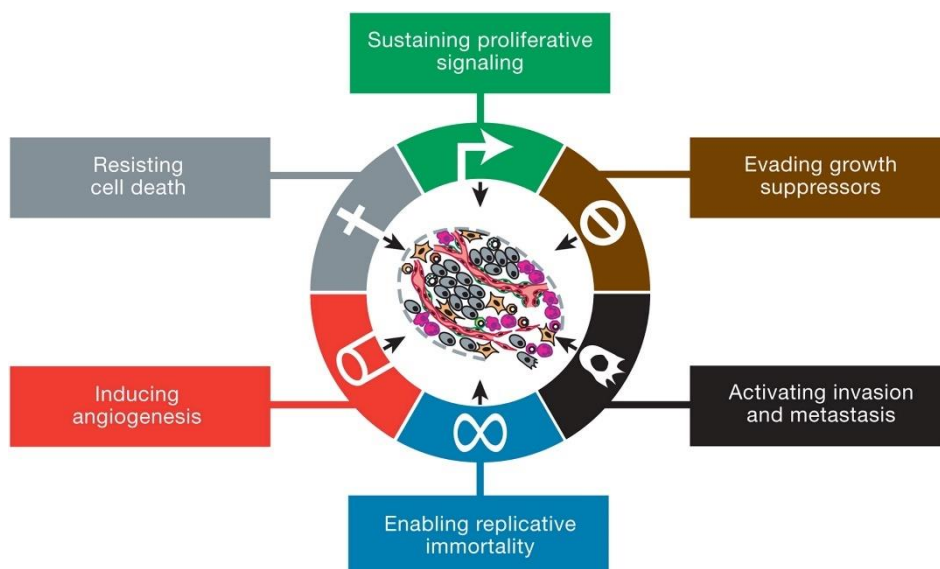
Figure 1: Overview of the hallmarks of cancer. Figure from Hanahan and Weinberg, 2011.[1]

Both Hanahan and Weinberg themselves as well as Fouad and Aanei revisited and updated the first six hallmarks later on, refining the definitions and adding metabolic reprogramming, immune modulation and the tumor microenvironment (Figure 1).[1,4] The following sections will provide a brief overview of the state-of-the art opinions on the hallmarks of cancer and their potential to enable cancer-specific treatment.

1.1.1 Sustained Proliferation and Evasion from Growth Suppressors

In healthy cells, proliferation is a tightly regulated process. Growth signals are required for normal cells to transition from a resting state to active proliferation. Simplified, cancer cells produce high levels of those growth signals in autocrine (self-stimulating) or paracrine (stimulation of nearby cells) manner to sustain continuous proliferation. Simultaneously, the receptors for growth factors are overexpressed or constitutively active. Binding of the polypeptide growth factors to their respective receptors triggers their activity and intracellular signaling pathways.[5] Further downstream, changes in the signaling cascade promote cell proliferation, but have also implications in other hallmarks like immune evasion or metabolic aberrations.

Prominent examples of growth factors and receptors heavily involved in cancer progression are the insulin-like growth factor family, vascular endothelial growth factor (VEGF) family, the transforming growth factor β (TGF-β) and the epidermal growth factor receptor family (EGFR family).[5] TGF-β is a very challenging drug target, as its activation is only tumorigenic in late stages of the disease and it actually acts as tumor suppressor in early stages.[6,7] The EGFR family consists of four members, the most popular being ErbB2/Her2, which is often overexpressed in breast, ovarian as well as non-small cell lung cancer and associated with cancer progression.[8,9] In consequence, it is a well-established target for Her2 positive tumors, utilizing anti-Her2 antibodies often in combination with other treatment like radiotherapy.[10,11] Growth factor receptors offer a promising but challenging platform for cancer therapy, as upregulation of a specific receptor is cancer type-dependent and some cancers rapidly develop resistances. Typically, tyrosine kinase inhibitors or specific antibodies are used for cancer therapy, and, as the monotherapeutic effects are rather moderate, mainly in combination with conventional chemotherapy or radiotherapy.[5]

Further downstream, mutations in the signaling pathways promoting cell proliferation contribute to cancer progression. A well-studied example is the rat sarcoma viral oncogene homolog (RAS) protein family, consisting of the three members Kras, Nras and Hras.[12] Activated by receptor tyrosine kinases like EGFR, RAS binds guanosine triphosphate (GTP) and triggers several signaling pathways important for cell proliferation. In cancer, RAS is either overexpressed or protein mutations lead to a stabilization of the GTP-bound, thus constitutively active, state.[13] RAS is very often mutated in human cancers, with over 80 % in

pancreatic and over 30 % in colorectal and lung cancer.[12] Despite this high incidence, therapeutic targeting of RAS remains challenging, as the involvement in complex signaling pathways leads to severe side effects and feedback loops.[14,15]

In healthy cells, cell division and the cell cycle is regulated and controlled by several checkpoints to prevent accumulation of damaged cells.[16] Cells that don't pass these checkpoints undergo repair mechanisms or, if the damage is irreparable, apoptosis, the cell's programmed cell death. Cancer cells developed mechanisms to suppress checkpoint proteins and thereby evade growth suppression. TGF-β has already been named as important tumor suppressor, and its loss is associated with tumor progression.[17] In over 50% of cancers, the function of the nuclear transcription factor p53 is impaired, implicating heavy involvement in cell cycle regulation.[2,18] Indeed, p53 acts as tumor suppressor by induction of cell cycle arrest and apoptosis and is involved in metabolic pathways.[19] As therapeutic reactivation of p53 is far more challenging than inhibition of oncogenic drivers like kinases, only two compounds targeting mutant p53 are in clinical trials.

1.1.2 Resistance to Apoptosis and Replicative Immortality

Tightly related to the sustained proliferation, cancer cells exhibit changes on an intracellular level that result in replicative immortality and resistance to apoptosis for unlimited replication required for macroscopic tumors. The replication potential is limited by the length of the telomers, short DNA tandem repeats at the end of the chromosomes that are shortened during replication. Once the telomers reach a critically short length, cells either undergo senescence or apoptosis.[20] The enzyme telomerase counteracts this effect and elongates the telomers again; unsurprisingly, it is upregulated in cancer and an interesting, though very challenging, therapy target.[21,22]

Apoptosis, also referred to as programmed cell death, is a signaling cascade ultimately leading to break-down of the cell. Extrinsically, death signals released from natural killer cells or macrophages are recognized by death receptors from the tumor necrosis factor (TNF) superfamily of proteins. Upon binding, a death-inducing signal complex is formed resulting in caspase 8 and 9 activation.[23] Intrinsic, or mitochondrial, apoptosis is triggered by various signals, for example p53, and is governed by the Bcl-2 protein family that can be further subdivided into the proapoptotic BH3-only proteins and anti-apoptotic Bcl-2 proteins.[24] Upon binding of BH3-only proteins, proapoptotic Bcl-2 homologous antagonist/killer 1 (BAK) and Bcl-2 associated X protein (BAX) are released which in turn stimulate mitochondrial cytochrome C release.[25] Again, this process culminates in activation of caspase 8 and 9, initiating proteolysis by further effector caspases. Thereby, loss of pro-apoptotic or upregulation of anti-apoptotic proteins contributes to cancer's resistance against apoptosis. In consequence, anti-cancer drugs directly targeting the apoptotic pathway block anti-

apoptotic Bcl-2 family members via BH3-only mimetics.[26] Although successful in various cancers, BH3 mimetics suffer from dose-limiting on-target toxicity and high relapse rate. Novel approaches combine both surface tumor antigen specific antibodies with BH3 mimetics or improvement of tumor delivery to reduce toxicity.[27]

Senescence is a cell state believed to be complementary to apoptosis and is described as irreversible exit from the cell cycle. Upon reaching a certain number of replicative cycles or caused by cellular stressors, cells change their morphology to a flatter, bigger shape (in cell culture) and enter the cell cycle arrest. Most important, they develop the senescence-associated secretory phenotype (SASP).[28] While senescence itself is tumor-suppressive, the SASP response is very diverse and contributes to tumor progression.[29] Therapy-induced senescence achieved by radiation or chemotherapy is used to render cells susceptible to senolytic therapy specifically targeting senescent cells, an approach that is currently explored in more detail.[30,31]

1.1.3 Angiogenesis

Blood vessels secure the energy and nutrient supply throughout the whole body; as such, cancer cells promote angiogenesis, the formation of novel blood vessels within the tumor. Without angiogenesis, tumors would not be able to grow further after they reach a critical size of 1-2 mm.[32] During the so-called angiogenic switch, tumors shift the homeostasis between pro- and anti-angiogenic factors towards pro-angiogenesis, leading to tumor progression and malignancy.[33] The VEGF signaling pathway is the key mediator of angiogenesis and is upregulated in cancer and under hypoxic, or oxygen-deprived, conditions.[32] Thus, as cancer cells further away from vasculature lack oxygen and become hypoxic, they express more VEGF and promote angiogenesis.[34] Anti-VEGF antibodies and VEGF inhibitors have become promising anti-cancer drugs, and other anti-angiogenic therapies like upregulation of thrombospondins, endogenous inhibitors of angiogenesis often downregulated in cancer, are currently explored.[35,36]

1.1.4 Invasion and Metastasis Formation

While cancer typically first forms at only one place, e.g. prostate or breast cancer, many types are prone to invade other body parts in form of metastasis. This process can be split in two main parts: first, physical detachment of cancer cells from the main lesion and migration to the metastatic site, and second, colonization and clinical manifestation of the metastasis.[37] Epithelial-mesenchymal transition (EMT), the conversion of epithelial primary cancer cells to motile mesenchymal cells, is crucial for cancer cell migration.[38] Again, the TGF-β pathway is a potent inducer of EMT, rendering it an even more attractive target for cancer therapy.[39] After the mesenchymal cancer cells enter the lymphatic vessels or the blood stream, they

can travel through the whole body until they extravasate again. As the microenvironment in the target tissue differs from the one at the primary site, metastases develop individual adaptations and in consequence show altered gene expression and metabolism compared to the primary site.[40,41] This is a particular challenge in cancer treatment, as metastatic sites might be non-responders to the therapy regimen of the primary tumor and require different treatment. In addition, metastatic cancer cells can remain dormant in the body for decades and only progress to macroscopic tumors years after dissemination from the primary site. Dormant micro-metastases are often the cause for a late relapse of the cancer, as metastatic dissemination occurs early in the disease.[42,43]

1.1.5 Metabolic Reprogramming

To sustain the increasing energy demand caused by fast proliferation, cancer cells alter their metabolism. This does not only include enhanced uptake of essential extracellular nutrients like glucose and glutamine for carbon intermediate supply but also aberrations in metabolic pathways and gene regulation driven by metabolites.[4]

In healthy, differentiated tissue, glucose is first metabolized to pyruvate through glycolysis. In the presence of oxygen, pyruvate then enters the mitochondrial tricarboxylic acid (TCA) cycle after conversion to acetyl-CoA (oxidative phosphorylation). This process yields energy in form of up to 36 mol adenosine triphosphate (ATP) by complete conversion of glucose to carbon dioxide. In absence of oxygen, pyruvate is converted to lactate (anaerobic glycolysis), allowing for ongoing glycolysis but is less effective (2 mol ATP).

In proliferative tissue and cancer cells, glucose is mainly metabolized to lactate regardless of the presence or absence of oxygen, the so-called aerobic glycolysis or Warburg effect.[44,45] By this, glucose consumption is ensured as well as accumulation of upstream metabolites for biosynthesis of higher macromolecules and preservation of carbon-carbon bonds. To enhance glucose uptake, the transporter GLUT1 is upregulated in many cancer types and associated with poor prognosis.[46-48] GLUT1 subsequently emerged as target for cancer therapy, as inhibition was shown to suppress tumor growth, or as diagnosic agent with fluorescently labeled probes.[49,50]

The non-essential amino acid glutamine serves as carbon donor and as source for nitrogen.[51] As such, cancer cells have a high glutamine demand. Exemplarily, expression of the glutamine transporter SLC1A5 is highly upregulated in triple-negative breast cancer (TNBC) and plays a role in the progression of head and neck cancer.[52,53] In cancer cells, glutamine is converted to glutamate by glutaminase (GLS), which can be reversed in an ATP-dependent manner by glutamine synthase (GS). It is either utilized directly or metabolized to α-ketoglutarate to enter the TCA cycle. The oncogenic transcription factor c-myc is a key player in dysregulated glutamine metabolism as it upregulates glutamine

transporters and enhances GLS expression to deplete the glutamine pool, thus encouraging more glutamine uptake.[54,55]

Myc proteins are one of the most-studied protein families due to their large involvement in cancer-related gene transcription and translation, thereby contributing to progression, growth and maintenance of malignancies.[56] As 'Jack of all trades but master of none', myc is heavily involved in cancer energy metabolism, in particular glutamine, glucose and nucleotide metabolism, but also in DNA replication, cell proliferation, and alteration of the tumor microenvironment.[57] Unsurprisingly, myc expression is dysregulated in about 70 % of all cancers.[58]

In addition to dysregulation of metabolic gene expression, mutations in metabolic genes can drastically contribute to cancer progression. One of the most studied examples is the mutation of isocitrate dehydrogenase (IDH), a crucial enzyme of the TCA cycle.[59] Wildtype IDH converts isocitrate to α-ketoglutarate, while mIDH drastically loses efficiency and gains the capability to reduce α-ketoglutarate to the oncometabolite 2-hydroxyglutarate (2-HG). 2-HG acts as a competitive inhibitor of α-ketoglutarate-dependent enzymes, which epigenetically regulate gene expression by DNA and histone demethylation.[60] In consequence, 2-HG induces DNA and histone hypermethylation which leads to dysregulated gene expression.[61] IDH is mutated in approximately 80% of glioma grade II/III cases and current research focuses on the development of small molecule mIDH-specific inhibitors, however, their efficacy is under discussion.[62-64]

1.1.6 The Tumor Microenvironment

While decades ago, cancer was perceived as a mass of uncontrollably growing cells, it is now evident that not only cancer metabolism is tightly regulated but also that cancer is not only one type of cells. Cancer stem cells, cancer-associated fibroblasts and endothelial cells, amongst others, and alterations in the tumor cell surrounding stroma contribute to a highly complex interplay which is generally described as the tumor microenvironment (TME).[65] As cancer progresses, the TME adapts and changes due to nutrient availability, metabolic alterations and tissue remodeling. Typical microenvironmental features are dysregulated pH or hypoxia, both promoting tumor growth, survival and therapy resistance.[66,67]

1.1.7 Immune Modulation in the Context of the Tumor Microenvironment

Another aspect of cancer complexity is their ability to evade and suppress the immune system. Importantly, the TME can co-opt innate and adaptive immune cells like macrophages or T cells to evade antitumoral immune response.[68] Immune cell infiltration in tumors can be a prognostic marker, and a strong initial immune response may prevent tumor invasion and metastasis.[69] However, tumor cells can actively disenable the immune response by

interfering with cytotoxic T cells (expression of specific surface proteins provides an inhibitory signal) and antigen presenting cells (natural selection of low-antigen expressing tumor cells). Chronic inflammation, an innate immune response mainly mediated by macrophages, also promotes tumor growth by secretion of cytokines, chemokines and growth factors.[70]

Immune therapy aims to extrinsically modulate the immune system through mainly activation, or blockade of the inhibitory surface proteins like programmed death-ligand 1 (PD-L1), thus reactivating cytotoxic T cells (immune checkpoint inhibition).[71] Additionally, genetically engineered T cells that specifically target tumor surface markers (chimeric antigen receptor or CAR T cells) emerged as very promising therapeutic option for non-solid tumors.[72]

In essence, cancers' heterogeneity and complex cellular genetic and metabolic changes contribute to the severeness of this disease but also features a great number of potential targets for personalized cancer therapy. Many anti-cancer drugs have effects on several different hallmarks as molecular changes in cancer cells are heavily intertwined. Still, novel hallmarks are defined and discovered, as demonstrated by a recent review from Hanahan, elaborating on "emerging hallmarks and enabling characteristics" like phenotypic plasticity, senescent cells, non-mutational epigenetic reprogramming, and polymorphic microbiomes.[73]

In this work, the focus lies on cellular stress in cancer, in particular replicative stress, and its potential for cancer diagnostic, therapy and patient stratification.

1.2 Cellular Stress in Cancer

As cancer cells proliferate at high rate, they are under constant cellular stress. Environmental stressors like ultraviolet (UV) light or temperature, chemicals, and fast accumulation of metabolism byproducts like reactive oxygen species (ROS) or unfolded proteins lead to a plethora of molecular responses. Cellular stress is highly complex and, although a promising anti-cancer target, identification of stress-specific biomarkers is challenging. This section will give definitions of different types on cellular stress, and provide the state-of-the art research about the main topic of replicative stress and its implication in cancer therapy.

1.2.1 Metabolic Stress

ROS, byproducts of metabolism, are free radicals that are on one hand important as signaling molecules for cell growth and differentiation, but, on the other hand, must be kept under tight control to prevent toxicity. ROS can damage DNA, lipids and proteins, leading to mutations, genetic instability and impaired cellular function. Counterplayers of ROS are detoxifying proteins like catalase, glutathione peroxidase (GPx) or superoxide dismutase (SOD).[74] Thus, the balance between ROS levels and antioxidants is crucial for normal cell function.

In cancer, ROS levels are increased due to increased metabolism. Thus, cancer cells accumulate ROS and exhibit more oxidative stress. While this oxidative stress is mostly known as oncogenic, excessive ROS can induce apoptosis and cell death. Drugs that increase ROS production are used to drive cancer cells with high oxidative stress into apoptosis, however, this negatively affects healthy cells by inducing redox imbalance.[75]

Therefore, antioxidant protein levels also play an important role in controlling metabolic stress. Serum SOD was found to be increasingly expressed during the development of breast cancer, pointing towards a compensatory mechanism.[76] Overexpression of GPx is associated with poor prognosis in thyroid cancer, and its inhibition has been shown to be antitumorigenic.[77]

Other metabolic stress includes low glucose levels, hypoxia or deprivation of other nutrients, which in turn leads to altered glucose metabolism, fatty acid synthesis and thus adaptation of the tumor to the changed metabolic environment.[78]

1.2.2 ER Stress

Ribosomal protein translation takes place at the rough endoplasmatic reticulum (ER). The ER is responsible for correct protein folding with the help of its chaperone proteins, post-translational protein modifications and translocation of proteins to the target region. ER stress and hypoxia are highly intertwined, as some post-translational modifications are oxygen-dependent. Nutrient shortage and hypoxia cause ER stress, but while acute stress

mainly contributes to cell death via apoptosis, chronic stress leads to adaption of the cancer cells to the changed environment.[79,80] Thus, ER stress plays an important role in tumor growth and the development of the tumor microenvironment. Other factors that contribute to ER stress are ROS accumulation and a low pH interfering with calcium homeostasis.[81]

Disturbance of the ER homeostasis leads to accumulation of un- or misfolded proteins, and triggers the unfolded protein response (UPR). The UPR consists of three stress sensing branches: inositol-requiring enzyme 1α (IRE1α), protein kinase R-like ER kinase (PERK), and activating transcription factor 6 (ATF6).[82] Under normal conditions, the sensors are bound by binding-immunoglobulin protein (BiP), but dissociate upon accumulation of unfolded proteins as BiP has a higher affinity towards them in comparison to the sensors.[83] When activated, IRE1α unconventionally splices the mRNA coding for X-box binding protein 1 (XBP1) which in turn promotes protein folding capacity. ATF6 is converted to its fragment ATF6f which acts as transcription factor for ER chaperones, and PERK phosphorylates the eukaryotic translation initiation factor 2 α (eIF2α).[82] The phosphorylation of eIF2α has two roles: it blocks translation to gain time for the cell to restore ER homeostasis, and in case of sustained ER stress, it induces cell death.[84] In addition, the ER-located chaperone calreticulin is translocated to the cell surface and promotes immunogenic cell death.[85]

As the UPR is well-studied, several small molecule inhibitors targeting PERK, IRE1α and ATF6 have been developed and are under investigation for their anti-tumorigenic effects.[86,87] Interestingly, IRE1α inhibition did not reduce hypoxia tolerance while PERK inhibition does, pointing towards involvement of the PERK UPR branch in tumorigenesis.[88] Current studies also explore the targeting of 'undruggable' Kras-driven lung cancer with inhibitors that activate the UPR, driving the cells into apoptosis.[89]

1.2.3 Replicative Stress

Both metabolic and ER stress are interlinked with a central theme in cellular stress: replicative stress. DNA replication is at the core of cellular division. When cells proliferate, they need to produce two identical DNA double helices per original DNA double helix in order to duplicate. The process in general is highly governed by control and repair enzymes and features high fidelity, however, it still bears a lot of error potential, in particular in cancer cells. The DNA structure was discovered by Nobel laureates Watson and Crick in 1953, and since then, the double helix with their two compliment strands is very well studied.[90] In the eukaryotic nucleus, replication starts at the replication origins. Multiple origins across all DNA space are activated at the same time (origin firing), and the amount of replication origins is dependent on DNA base availability (Figure 2 upper part). Not all available origins fire at the same time but some are only activated upon replication fork stallation.[91]

The core of DNA replication is the 'Y'-shaped replication fork, or replisome, where different DNA polymerases and associated proteins dynamically synthesize the replicate DNA. In the replication bubbles, initiator proteins assemble at the replication origins of the DNA and recruit helicases to unwind the double strand.[92] The thereby created tension is released by topoisomerases, enzymes that temporarily break one DNA strand to allow rotation around the intact strand.[93] Replication protein A (RPA) subsequently stabilizes the single-strand DNA to prevent rewinding and allow for association of the replication machinery. The large family of proteins responsible for DNA synthesis, the DNA polymerases, can only work in 5' to 3' direction, so, one of the two antiparallel DNA strands (the leading strand) is polymerized continuously while the lagging strand is synthesized in short fragments (Okazaki fragments) which are connected afterwards by DNA ligase (see Figure 2 lower part for an overview).[94]
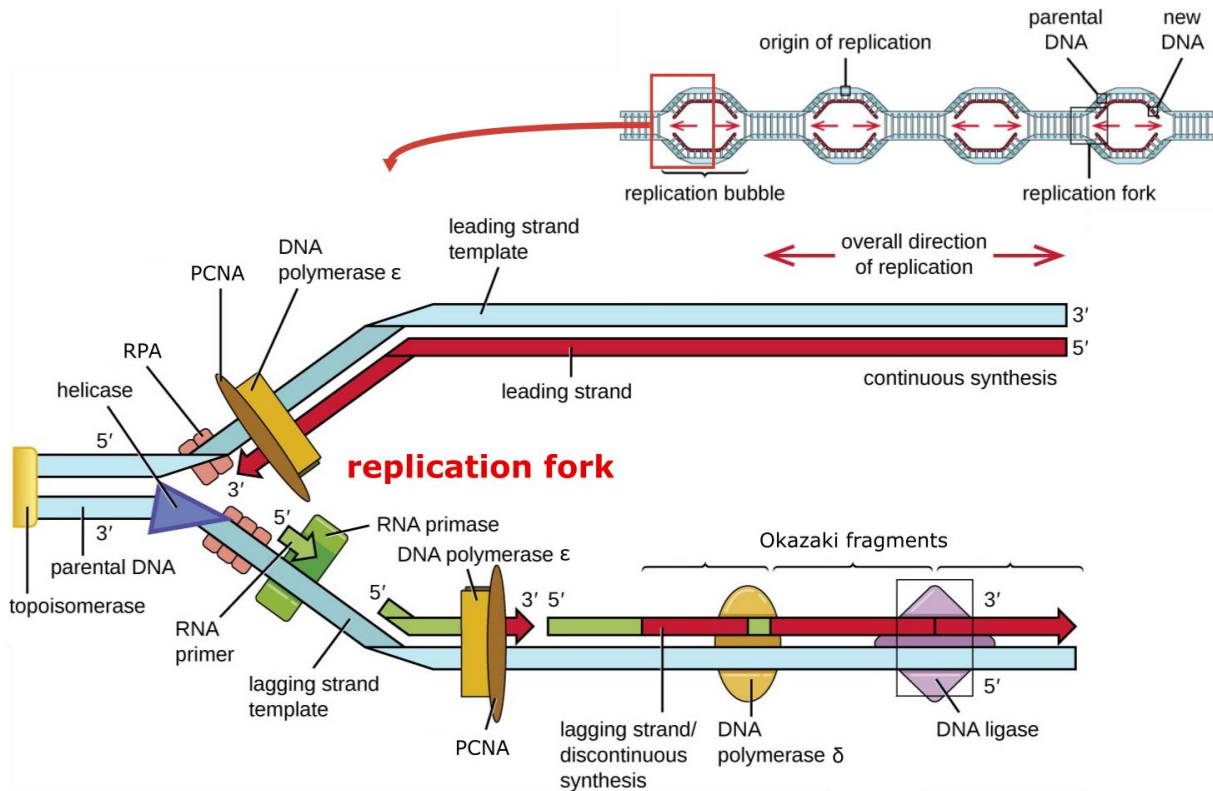
Figure 2:Schematic depiction of eukaryotic replication and the replication fork. In the upper part of the image, multiple replication origins are displayed, and in the lower part of the image, the 'Y'-shaped replication fork is displayed with the main proteins responsible for replication. Figure adapted from Parker et al, 2016.[95]

The replication fork often stalls due to replication barriers in the DNA like fragile or termination sites, or DNA lesions.[96] If the replication fork is slowed or stalled, it can either be stabilized and recovered through checkpoints, or it will collapse.

Replicative stress is highly complex and present in all proliferating cells; however, cancer cells exhibit more due to their sustained fast proliferation. Although an exact definition does not exist, it is commonly agreed to that slowed or stalled replication fork progression is a key

feature. Due to its close relationship to DNA damage and repair, the following sections will focus on pathways and biological interactions of replicative stress.

1.2.2.1 DNA Damage and Repair

As not only a hallmark for both cancer and ageing, but also a key player in replicative stress, DNA damage is a threat to normal cell function.[97] Endogenous, for example replicative stress or accumulation of ROS, and exogenous factors, like UV light or chemicals, cause changes in the molecular structure of the DNA bases (deamination, methylation, oxidization, or dimerization) or DNA breaks.[98] In addition, mismatched DNA bases can be occasionally introduced as the replication machinery performs with high fidelity but is not perfect (Figure 3 upper part). Persisting DNA damage can lead to integration of the mismatch in the genome and thus promote mutagenesis and disease.[99] Fortunately, repair mechanisms like the DNA damage response (DDR) and DNA repair pathways are able to resolve those damages efficiently in healthy cells (Figure 3 lower part).[100]
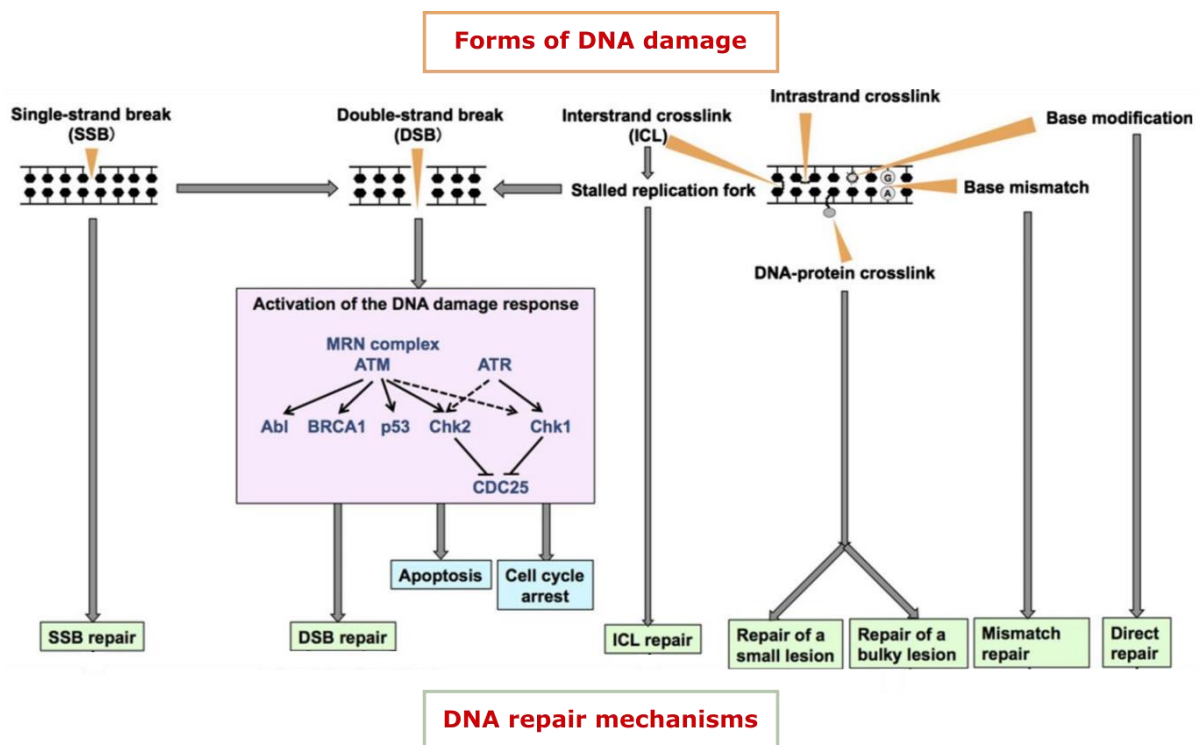
Figure 3: Overview of the complex interplay between DNA damage, the DDR, and DNA repair pathways. Figure adapted from Hosoya and Miyagawa, 2014.[100]

The DDR is orchestrated by three key proteins: ataxia telangiectasia mutated and Rad3-related (ATR), ataxia telangiectasia mutated (ATM) and DNA protein kinase (DNA-PK). All are activated upon DNA double-strand breaks (DSBs) (ATM and DNA-PK) or, additionally, various other DNA damages (ATR) as well as DNA repair mechanisms (ATM).[101,102] They initiate downstream signaling cascades and DNA repair (Figure 3 middle). When the extent

of DNA damage overwhelms the repair machinery, checkpoint activation leads to cell cycle arrest or apoptosis, which is a mechanism exploited in DNA-damaging cancer therapy.[103]

There are five main DNA repair mechanisms besides direct repair: base and nucleotide excision repair (BER/NER), mismatch repair (MR), homologous recombination (HR) and non-homologous end joining (NHEJ).[98] DNA base damage is usually repaired by specific repair enzymes that reverse alkylations, or by BER where the damaged base is removed by a glycosylase, the abasic site cleaved by abasic site endonucleases and the gap filled with newly synthesized DNA.[104] Likewise, more bulky DNA damage is repaired by NER. As indicated by the name, MR recognizes transient single strands introduced by mismatched DNA bases and, as BER and NER, excises a portion of the DNA including the mismatch to subsequently replace this part with the correct bases.

DNA break repair is mechanistically divided in two groups, the repair of single-strand breaks (SSBs) and of DSBs. SSBs occur from oxidative damage, flawed topoisomerase activity, or during BER at the abasic sites. During poly(ADP-ribose) polymerase (PARP) 1-mediated SSB repair, the SSB is recognized by PARP1 which recruits subsequent enzymes (see 1.3.1 PARP and PARP Inhibitors). Due to rapid modification of the DNA termini, the SSBs are excised and the gap is filled by DNA polymerase.[105]

HR and NHEJ are the two pathways mainly mediating the repair of the highly toxic DSBs that, when unresolved, contribute to various diseases including cancer. After end resection, HR essentially uses the correct sequence from the sister chromatin as template for replacement; in contrast, NHEJ directly religates the broken DNA. Thus, HR is limited to the late S and G2 phase of the cell cycle as it requires a homologous template DNA. NHEJ can take place throughout the whole cell cycle but is substantially more error-prone. As Ku70/80, the initiators of NHEJ, have a high affinity and fast binding kinetics to free DNA, end resection is an important factor to favor the high-fidelity HR.[106] 53 binding protein 1 (53BP1) plays a key role in mediating NHEJ repair and has an antagonistic relationship with breast cancer gene 1 (BRCA1), which is a critical catalytic enzyme for HR.[107] Aberrations in the DNA repair machinery, for example loss of BRCA1 function, is known to hamper HR and contributes to mutagenesis and tumor formation.

1.2.2.2 Causes of Replicative Stress

The causes of replicative stress are all related to slowing or stallation of the replication fork or interference with the replication machinery. Interestingly, it has been shown that also increased speed of the replication fork induced by PARP inhibitors contributes to replicative stress and genomic instability.[108]

Direct DNA damage like SSBs/DSBs, hindrance of their repair, as well as other DNA lesions are the main causes that lead to replication fork stallation. Exemplarily, inhibition of

topoisomerase function by camptothecin stabilizes the topoisomerase-DNA complex and thus slows repair of SSBs, and in addition depletes topoisomerase levels.[109] Other physical barriers that lead to replicative stress are unusual DNA secondary structures like formation of hairpins or triplexes, or G-quadruplexes in GC-rich DNA. Naturally occurring chromatin structures are also considered to hamper replication machinery function.[110]

Limited availability of replication factors like nucleotides, or proteins of the replication machinery is another cause of replicative stress.[110] For example, aberrant replication initiation causes simultaneous firing of too many origins which in turn depletes the nucleotide pool. Drugs like hydroxyurea (HU) exogenously alter the nucleotide pool and thereby slow initiation and progression of replication.[109]

As transcription and replication both require access to the DNA template, those two processes can collide, especially at highly-transcribed sites where DSBs are common.[111] RNA-DNA hybrids, where newly transcribed mRNA hybridizes with the parental DNA, can cause a halt of the replication fork. As ribonucleotide pools exceed deoxyribonucleotide pools in cells, and the polymerases can not strictly distinguish between the nucleotide types, ribonucleotides are commonly incorporated in the DNA, causing the replication machinery to stop until the mis-incorporated nucleotide is removed.[112]

In addition, oncogenes like myc and Kras can cause replicative stress. The exact mechanisms are still unclear and dependent on the respective oncogene. Most oncogenes cause both elevated levels of transcription that interferes with replication, and promote replication initiation and origin firing, leading to depletion of nucleotide pools.[113,114]

1.2.2.3 Consequences of Replicative Stress

There are two possible outcomes in case of a slowed or stalled replication fork: fork rescue and restart, or collapse and breakage. Upon checkpoint activation, the ATR primary substrate kinase checkpoint kinase 1 (CHK1) inhibits late and promotes dormant origin firing. Most importantly, CHK1 triggers cell cycle arrest. This is particularly vital to give the cell extra time to repair the DNA damage before potentially entering mitosis with incompletely replicated DNA.[114]

For fork rescue, reversed replication forks are an important intermediate.[115] Mechanistically, the nascent DNA is unwound and anneals in a reverse manner to parts of the parental DNA forming a 'chicken foot structure' instead of the typical 'Y' shape.[116] The reversed fork is subsequently stabilized by RPA and BRCA1/2-mediated DNA binding of RAD51 (Figure 4).[101] Firing of downstream dormant origins initiates another replication fork that can rescue the stalled one. In case of DNA lesions, the barrier which is on double-stranded DNA again is either removed by DNA repair pathways, and lesions on single-stranded DNA can be overcome utilizing specialized DNA polymerases.[115] During template switching, the nascent

DNA is used as a template to synthesize past the lesion. Lastly, cleavage of the nascent DNA strand initiates HR-mediated repair. Once the cause of stallation is removed, the fork is reversed again or degraded, or restarted via HR or branch migration, and replication can continue in a normal manner.[117]
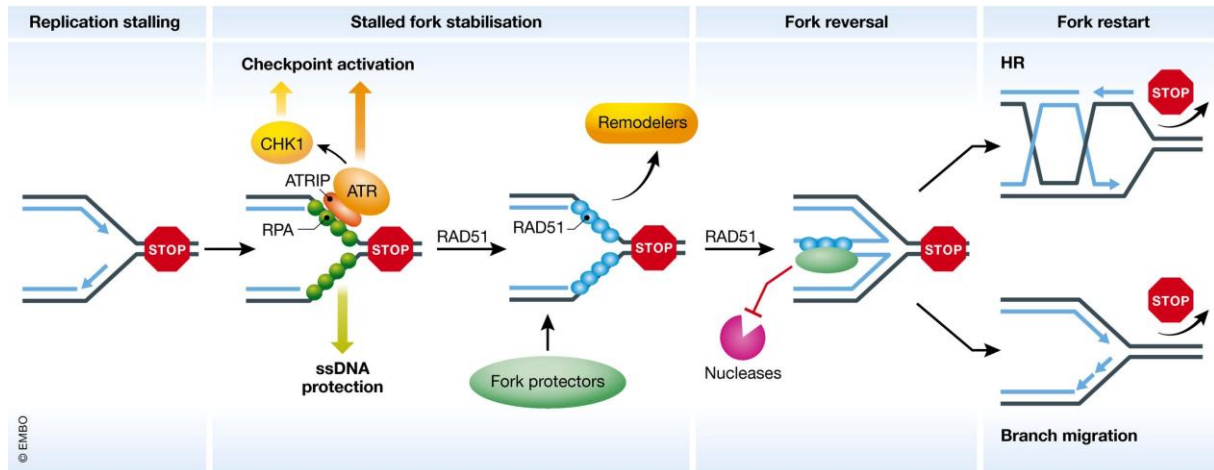
Figure 4: Schematic of essential proteins involved in the replicative stress response. Figure from Liao et al, 2018.[118]

In case of replication fork collapse, the replisome dissociates from the DNA and exonucleases, mainly EXO1, degrade the DNA. This can potentially form toxic DSBs. Alternatively, the single-strand end is resected and recombined using the sister chromatid as a template, after which the replisome reassembles.[119] In consequence, a high amount of fork breakage either leads to progression of an error-prone replisome, or accumulation of DSBs, and thus contributes to genomic instability, induction of cellular senescence or apoptosis.

Genomic instability is promoted by replicative stress as some of the misincorporated nucleotides or incompletely resolved DNA lesions lead to integration of the mutation in the genome. Globally, the most abundant consequence of replicative stress is cancer. Although not an immediate consequence, the genomic instability and accumulation of DNA damage promotes oncogenic mutations. In contrast, direct mutations in the repair machinery or the replicative stress response, if progressing to a post-embryotic stage, feature severe symptoms and lower life expectancy in mice.[120] Fortunately, those severe genetic birth defects are very rare and symptoms can range from very mild to very severe; unfortunately, there is only symptomatic therapy avaliable.[121]

1.2.2.4 Therapeutic Implications

Although described as "Achilles' heel" of cancer, therapeutic targeting of tumor stress, and in particular replicative stress, is not trivial. There are many factors involved, and although a range of therapeutics affect replicative stress, it is more a side effect than specific targeting.

Nevertheless, specific targeting of replicative stress by inhibition of proteins within the DDR or stress response has been shown to have an anti-cancer effect. Especially in cancers already treated with DNA-damaging agents or oncogene-driven high replicative stress, additional inhibition of the DDR can result in synthetic lethality by overloading the cancer cell with DNA damage and driving it into apoptosis.[122] In healthy cells, DDR inhibitors only have minimal effects as those cells can rely on several alternative repair pathways; however, they still affect highly proliferative tissue like bone marrow which has to be taken into consideration.

Small molecule inhibitors are described for several crucial DDR enzymes like ATM, ATR, CHK1 and DNA-PKs together with several downstream targets.[123] Those inhibitors are particularly potent in combination therapy with DNA damaging treatment like cisplatin, irradiation or temozolomide, but also monotherapy is investigated.[124-126] A great advantage is the already high probability of a defective DNA repair machinery due to frequent mutations in essential DDR enzymes, which potentiate the anti-cancer effects from this drug classes.[100] However, development of resistance by secondary mutations restoring the enzymes' normal function or upregulation of efflux proteins, is a limiting factor that still needs to be tackled.[100] Another challenge is the accurate monitoring of therapy response due to the lack of a biomarker suitable for imaging of replicative stress.[123]

1.3 Potential Candidates for Replicative Stress Biomarkers

The lack of a suitable biomarker for replicative stress hampers research on its therapeutic exploitation. Some biomarkers are available for antibody staining of resected tissue, but are often also correlated to other cellular processes like for example senescence. In the following chapter, potential biomarkers with focus on PARP enzymes and challenges in biomarker identification will be discussed.

1.3.1 PARP and PARP Inhibitors

In healthy tissue, PARP enzymes are essential mediators of fast DNA damage repair of SSBs. Generally, they add the posttranslational modification ADP-ribose to effector proteins utilizing nicotinamide adenine dinucleotide (NAD$^+$) as substrate. The PARP enzyme family consists of 17 members, but despite their name, only four (PARP1/2 and PARP5a/b) are able to perform poly(ADP-ribosyl)ation (PARylation) while all other members can only perform mono(ADP-ribosyl)ation (MARylation).[127] Poly(ADP-ribose) (PAR) chains can be branched and do not only change the biophysical properties of the proteins but are also recognized by the PAR-binding sites of several DNA repair enzymes which are subsequently recruited. Upon auto-PARylation, PARP1 is more and more negatively charged and dissociates from the DNA, supposedly to make space for the DNA repair machinery.[128] Poly(ADP-ribose) glycohydrolase (PARG) then reconstitutes PARP by removing the PAR chains.[129]

PARP1 senses a wide range of SSBs, and overhang and blunt end DSBs, via two of its zinc finger domains in a sequence-independent manner and thereby activates its catalytic domain.[130] PARP binding to DSBs is relatively fast, in consequence it is thought to fulfill the role of a 'first responder' to DNA damage.[131] In line with this hypothesis, it has been shown that the accumulation of the ATM-recruiting MRE11/RAD50/NBS1 (MRN) complex is mediated by PARP1.[132]

An increase in DSBs in PARP1-deficient cells suggests that PARP1 prevents the SSBs from escalation to DSBs which would need to be repaired by HR or NHEJ.[133] Upon PARylation of effector proteins including PARP1 itself, PARP1 may also recruit BER enzymes, however, the SSB preservation function seems to be most important.[134]

PARP1 also plays an important role in replication fork reversal and stabilization. The replication fork is slowed down in a PARP1-dependent manner in the case of DSBs.[135] Additionally, cleavage of PARP1 by caspase 3 is a marker for apoptosis and believed to be a mechanism to prevent NAD$^+$ and ATP depletion that would lead to induction of necrosis instead of apoptosis.[136]

Besides PARP1 and 2, PARP5a and b, also called tankyrase1 and 2 (TNKS1 and 2), are capable of PARylation and play an important role in telomere maintenance, mitosis and

regulation of the cancer-relevant Wnt-pathway. Although not involved in DNA repair, PARylation of enzymes by TNKS marks them for ubiquitinylation and degradation by the proteasome, thus regulating enzyme levels.[137]
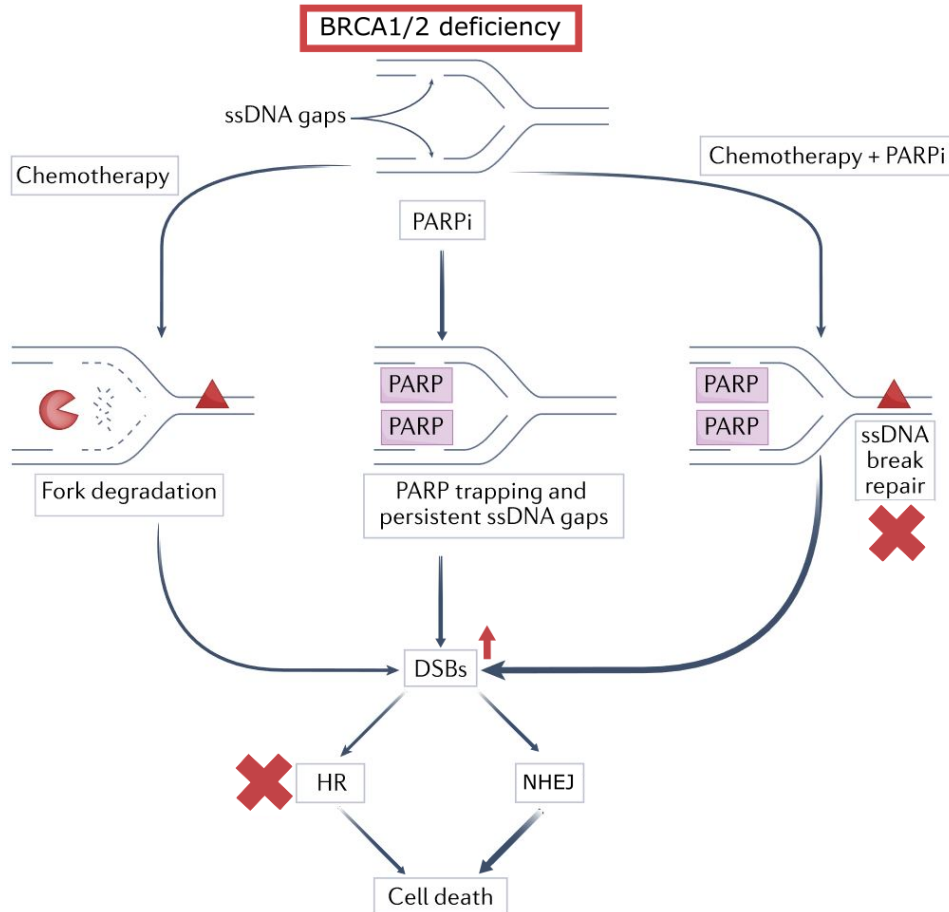
Figure 5: Synthetic lethality of PARP inhibitors in BRCA-deficient cells. Although chemotherapy alone also increases DSBs, additional PARP inhibition exacerbates the levels of DSBs further, leading to elevated cell death. Figure adapted from Cybulla and Vinidigni, 2023.[138]
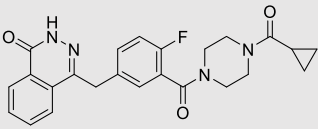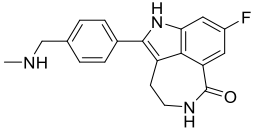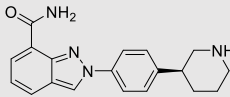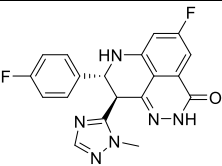
Especially in HR-deficient tumors that exhibit mutations in either BRCA1 or BRCA2, inhibition of PARP1 is often lethal for the cancer cells, as they are unable to repair sustained DNA damage caused by accumulation of DSBs, or only by the error-prone repair pathways NHEJ (Figure 5). Exemplarily, breast cancer often exhibits mutated BRCA1 and additional PARP inhibition induces synthetic lethality. Mechanistically, PARP inhibition follows two main molecular mode of actions: first, catalytic inhibition of the PARylation domain, and second, trapping of the PARP enzyme on the DNA.[139,140]

Several PARP1 inhibitors have been approved for cancer treatment in the USA by the food and drug administration (FDA), starting with the first, olaparib, in 2014.[141] Since then, olaparib has been extensively used for treatment of ovarian cancer in monotherapy and as maintenance therapy after cisplatin treatment.[142-144] The approval of other inhibitors followed with rucaparib and niraparib.[145,146] The most recently approved PARP inhibitor, talazoparib

(BMN673), showed exceptionally high efficacy that outperformed all of the previous by far.[147,148] This is believed to be an effect of the improved trapping mechanism of PARP1 to the DNA, leading to replication fork collapse.[149]

Table 1: Structures of FDA-approved PARP inhibitors. Approval data were accessed from https://www.drug.com (Nov. 2022).

INHIBITOR	FIRST FDA APPROVAL	STRUCTURE
Olaparib	2014 (Ovarian, fallopian tube, peritoneal, breast, pancreatic, and prostate cancer)	
Rucaparib	2016 (Ovarian and prostate cancer)	
Niraparib	2017 (Ovarian, fallopian tube, and peritoneal cancer)	
Talazoparib	2018 (Breast cancer)	

Although the PARP inhibitors are only approved for therapy in BRCA-mutated tumors, recent studies unlink the efficacy of the drugs from BRCA status.[150,151] Inhibitors of HR are known to increase PARP susceptibility. Radiation therapy, which induces DNA damage, seems to profit from maintenance PARP inhibition. PARP might not only be a potential biomarker for replicative stress but is also considered a good general tumor and prognostic marker. High PARP1 expression is associated with poor prognosis and survival in acute myeloid leukemia and high-risk neuroblastoma.[152,153] Additionally, PARP inhibitors are investigated for their repurposing in other diseases besides cancer, for example as neuroprotective agents, since PARP1 has been proven to be involved in neurodegenerative diseases like Parkinson's and Alzheimer's disease.[154]

It has been shown that PARP inhibitors increase replicative stress, and that suppression of HR increases PARP inhibitor susceptibility.[62,155] This indicates an essential role of PARP in DNA damage repair and replicative stress. In this work, PARP expression will be evaluated for its correlation with replicative stress, to answer the question whether PARP is a suitable biomarker.

1.3.2 Others

In vitro, the gold standard for quantification of replicative stress is the DNA fiber assay, where replication fork progression is measured by incorporation of fluorescently detectable nucleotides.[156] However, this method is not suitable for *in vivo* detection and quantification of replicative stress, so there is an urgent need for a measurable, specific biomarker. As the DDR and the replicative stress response are highly complex, there are other enzymes besides PARP1 that have the potential to serve as a biomarker. Many of them are associated with replicative stress and are in part also already exploited therapeutically.

Inhibition of the PAR-catabolizing PARG has been shown to have an anti-tumor effect as the lack of PAR cleavage from PARP renders it negatively charged, thus unable to bind to DNA again and initiate SSB repair.[157] As the mechanism of action is distinct from classical PARP inhibitors, PARG inhibition is considered an alternative therapy once a cancer developed PARP inhibitor resistance.[158]

The ATR/CHK1 and ATM/CHK2 axis features various targetable proteins, including ATR and ATM itself (see Figure 6 for an overview). ATR inhibitors have been shown to have a synergistic effect with both myc-overexpression induced replicative stress and in combination with olaparib as PARP inhibitor.[159] The main disadvantage of ATR/CHK1 inhibition is the essential role of this pathway in all cells.[160] While PARP inhibition is quite specific in combination with HR-deficient tumors, ATR/CHK1 inhibition suffers from severe on- and off-target toxicity and no inhibitor has been approved for clinical use so far.[161] Therefore, it seems sensible to target downstream proteins for both therapy and as biomarker for replicative stress for enhanced specificity.

Replicative stress also induces ATM activity not only in the context of DNA damage but also during hypoxic conditions, facilitating DNA replication and replication restart in a stress-specific manner.[162] However, ATM protein levels might not be increased during replicative stress as its activation occurs via dissociation of the inactive dimer into active monomers.[163] Still, ATM activity seems to be a marker for replicative stress and inhibitors have shown to sensitize tumors to radiation therapy and DNA damaging agents.[164] Several ATM inhibitors currently undergo clinical trials.[165] In addition, downstream phosphorylation targets like deoxycytidine kinase (dCK), a key enzyme of the deoxyribonucleoside salvage pathway, could be used to indirectly assess ATM activity.[166] There is evidence that dCK inactivation induces replicative stress, providing a link between nucleotide metabolism and replicative stress.[167] In addition, it has been proposed that ATR plays a role in dCK activation and regulation as well, doubling the interest in this protein.[168] Thus, dCK might also serve as an indirect biomarker for replicative stress, although it is currently used as a marker for imaging of immune cell infiltrates.[166,169]

A very interesting target is phosphorylated CHK1 as marker of ATR activity, which is of particular interest as changes in absolute protein levels might be negligible and thus not a good biomarker. It has been shown that upon chemical induction of replicative stress with HU, pCHK1 levels are increased.[170]

Wee1 is an effector kinase downstream of ATR/CHK1 that downregulates CDK1 and 2, two proteins responsible for S phase entry, by phosphorylation. When Wee1 is inhibited, CDK1 and 2 are more active, causing the cells to prematurely enter mitosis. In addition, CDK1 and 2 regulate dormant origin firing, and their activation will result in replication initiation.[171,172]
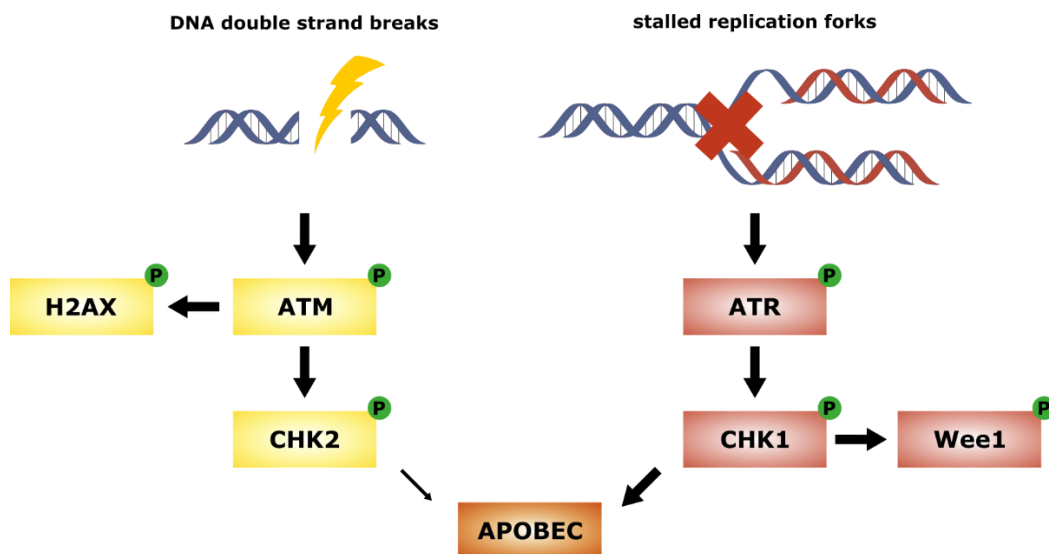
Figure 6: Schematic depiction of the ATM/CHK2 and the ATR/CHK1 axis in the context of replicative stress. DNA DSBs lead to activation of the ATM signaling cascade while stalled or slowed replication forks cause ATR activation. Figure derived from Weber and Ryan, 2015.[173]

The histone H2AX is phosphorylated at serine 139 (γH2AX) by ATM and is considered a DSB biomarker. However, it is not exclusively increased during DNA damage but also during apoptotic DNA cleavage and heat shock.[174,175] Furthermore, γH2AX emerged as a prominent biomarker of cellular senescence.[176] DBSs have been shown to induce an ageing-related phenotype, amongst others cellular senescence, in mice.[177] Thus, γH2AX is induced upon DSBs, but increased DSBs are not a specific marker for high replicative stress.

There is also a relationship between replicative stress and apolipoprotein B mRNA editing enzyme, catalytic polypeptide-like 3 (APOBEC3), a cytosine deaminase overexpressed in lung and breast cancer.[178] APOBEC promotes point mutations by converting cytosine to uracil, which subsequently contributes to mutagenesis.[179] It has been shown that replicative stress activates APOBEC mainly via the ATR/CHK1 and, in parts, the ATM/CHK2 axis, and its activity is strongly inhibited by CHK1 inhibitors.[180]

Two proteins that are well-studied for their role in replicative stress are the DNA-binding proteins RPA and RAD51. RPA foci are an *in vitro* marker for replicative stress, as it is

recruited to the damaged DNA single strand to prevent degradation.[181-183] Inhibition of RPA leads to destabilization of DNA single strands by digestion through nucleases, and has been shown to be an effective anti-cancer treatment.[184] After coating of the single strand DNA by RPA, the filaments of RAD51 recombinase are the main mediator of homologous DNA strand search and invasion during HR.[185] Thus, inhibition of RAD51 assembly leads to impaired HR and in consequence to sensitization of the cells for radiation or chemotherapy as well as PARP inhibitors.[186]

Since Myc is involved in a lot of oncogenic processes, it also plays a role in replicative stress. Global increase in transcription has been shown to increase replicative stress and promote genetic instability.[187] However, Myc might not be an ideal target as its upregulation is not exclusively tied to replicative stress but to other hallmarks like sustained proliferation, ER stress and altered metabolism as well.[188-190]

The recent increase in publications about therapeutic targeting of replicative stress emphasizes the importance of this molecular mechanisms. But despite all the efforts, no biomarker suitable for *in vivo* quantification has been defined up to date.

1.3.3 Challenges

As indicated in the previous chapters, replicative stress is a complex topic and highly intertwined with other pathways like DDR. DNA damage is considered both a cause and a consequence of replicative stress and partially utilizes the same signaling cascades. Also, some markers, for example γH2AX foci, are not only potential biomarkers for replicative stress but also for stress-related pathways like cellular senescence.

So far, no specific biomarker for replicative stress has been identified. In this work, PARP is investigated for its potential to fulfill this role, but other proteins are promising candidates as well. Considering the ultimate goal of translation to a clinical setting, the main challenge here is to assess whether candidate proteins exhibit increased expression, which is a measurable outcome with non-invasive imaging methods, or are merely activated or translocated. Activation of proteins through phosphorylation is frequent, but visualizing or detecting phosphorylation *in vivo* is highly challenging. The current preclinical and clinical standard-of-care diagnostic method for cancer is non-invasive imaging, since it features many advantages for patients as discussed in the next section.

1.4 Non-Invasive Imaging Methods

Identification of abnormal growth or tissue structure is often accomplished by anatomical magnetic resonance imaging (MRI) or computed tomography (CT) scans of the whole body or the body part in question. However, these methods mainly yield anatomical information about size and texture of the lesion. Personalized medicine relies on functional and molecular information about certain mutations in oncogenes, changes in expression levels of surface markers or presence of potential therapeutic targets. When characterizing abnormal masses, the first thought usually goes to biopsies, where a portion of the lesion is surgically removed for histological examination. Due to the potentially bad health condition of the patient, the difficult position of the lesion (e.g. brain tumors), and the possibility of longitudinal observation, non-invasive molecular imaging methods are preferentially used. They allow for identification of malignancy, patient stratification and aid the decision on the appropriate therapy regimen. In particular, nuclear imaging methods using radioactivity are very well suited for these purposes as they are highly sensitive and not limited by tissue penetration. The most prominent non-invasive nuclear molecular imaging methods are positron emission tomography (PET) and single photon emission computed tomography (SPECT), which employ a diverse set of radiotracers for cancer characterization.

1.4.1 SPECT and PET

The term "tracer principle" was shaped by Nobel price recipient George de Hevesy in the early 20th century, as a method to track molecules by incorporation of a radioactive isotope.[191] In short, radioactive isotopes have the same properties as their non-radioactive counterparts, thus they behave the same way in biological processes. As such, even trace amounts of radioactively labeled molecules are traceable and can shed light on metabolic processes with minimal risk to the body.

The discovery of the tracer principle set the basis for today's radiochemical and radiopharmaceutical research and has helped researches gain functional insights in the body preclinically and clinically. Detection of radioactive decay is possible by γ-photons that are either directly emitted from the radioisotope (SPECT) or created by positron/electron annihilation for β$^+$-emitting isotopes (PET).

The choice of radioisotope is dependent on the application. Typical SPECT isotopes are ^{99m}Tc, ^{123}I, ^{131}I or ^{111}In. They decay by emission of a single γ-photon that is detected by a gamma camera moving helically around the subject during a SPECT scan.[192]

In contrast, PET isotopes emit positrons (β$^+$) that are only detectable when they annihilate with nearby electrons. After decay, the positron travels a variable distance in the surrounding tissue (positron range). This distance is dependent on the isotope-dependent kinetic energy which decreases by interactions with the tissue until the kinetic energy is low enough to allow

for interaction with an electron and ultimately annihilation. In this process, two opposed γ-photons are emitted that are detected by circularly arranged detectors around the subject.[193,194] Using the position of the excited detector pairs and in some cases the differences in detection time, the exact position of the radioactive decay can be back-calculated using a line of response. Besides the positron range, scattering of the photons in tissue or detection of false coincidences can further decrease the spatial resolution besides technical limits.[195]

There is a wide range of PET isotopes that are used in research and patient care. Due to their convenient half-lives, ^{18}F (109.7 min), ^{11}C (20.3 min), and ^{68}Ga (68 min) are often preferred for the labeling of small molecules over longer-living isotopes like ^{64}Cu (12.7 h), ^{124}I (100.8 h), or ^{89}Zr (78.4 h).[196,197] The short-lived isotopes ^{15}O (2 min) and ^{11}C require an on-site cyclotron for isotope production while ^{18}F-labeled radiopharmaceuticals can be transported to other facilities or, in the case of ^{64}Cu, ^{124}I or ^{89}Zr-labeling, can be shipped even larger distances. Long-living isotopes allow for clearing of radiotracer from non-target tissue, and shorter-lived isotopes have lower organ doses and shorter measurement times.

The optimal choice of isotope for PET is dependent on many factors. The biological half-life of the radiotracer plays an important role. Biologicals like antibodies with long biological half-life require longer-living isotopes. Small molecules that only stay in the body for a short time before excretion can be labeled with short-lived isotopes.[198] The already mentioned isotope-dependent positron range is crucial to the resolution, as a smaller potential traveling distance of the positron leads to less blurring.[199] These factors need to be considered when choosing the labeling method for a novel radiotracer.

Besides diagnostic applications, therapeutic use of radionuclides or the combination (theranostic) allows for targeted radiotherapy. Especially targeted radiotherapy has advanced in the last years, dual-purpose molecules that can be labeled first with a SPECT or PET isotope for target quantification and then with an α- or β$^-$-emitting isotope for therapy are a promising tool for cancer therapy. Examples of such pairings are the exchangeable isotopes $^{123/124}$I/^{131}I or the matched pairing ^{68}Ga/^{177}Lu utilizing the same chelator for radiometal coordination.[200] Recently, α-emitters are utilized more frequently for theranostic approaches, as their highly focused and large deposited radiation dose is well-suited for specific tumor targeting.

1.4.2 MRI and CT

As SPECT and PET imaging mainly yields functional and molecular information on biological processes, these techniques are often combined with MRI or CT for the anatomical co-registration.

INTRODUCTION

MRI exploits the water protons that are available in bodies. Briefly, MRI utilizes a strong magnetic field to align their spin within that field. When a radiofrequency pulse is applied, the protons swing out of this equilibrium, and after the pulse is turned off, they release energy when realigning in the magnetic field. This energy can be detected and gives quantitative information about the water content and properties in the different regions of the subject.[201] Thus, MRI can be used to detect abnormal structures within soft tissue without exposing the subject to ionizing radiation.

CT is based on Roentgen technology, using an X-ray source with opposed detector rotating around the subject to create 3D images.[202] As with 2D Roentgen, dense tissues like bones attenuate the X-rays to a higher extent compared to soft tissue or air-filled structures. Although the contrast in soft tissue can be enhanced with highly attenuating contrast agents like iodine or barium, the main advantage of CT lies in the excellent bone contrast and spatial resolution.

In the clinic, CT is often preferred for trauma patients due to its superior bone contrast for the detection of bone fractures and the cheap and easy operation of the system. MRI is mainly used to diagnose diseases of soft tissue, like strokes, cancer and hemorrhages.

With the combination of functional imaging by PET or SPECT and anatomical information from CT scans or MRI, we have a powerful tool for cancer detection and characterization in hand. There are many different radiopharmaceuticals, or radiotracers, available that yield different functional information. In the next section, a selection of cancer radiotracers will be introduced to give an overview of the diagnostic possibilities.

1.5 Radiotracers for Cancer Detection and Characterization

Some radiopharmaceuticals are based on relatively small molecules that are labeled by exchange of an atom with a radioactive isotope (isotopologue) or with the help of a prosthetic group. However, a large number of cancer radiopharmaceuticals is based on antibodies or other biologicals. The huge advantage of utilizing radiolabeled antibodies, in particular for cancer imaging, is the variety of targets and clinically validated antibodies available and the straight-forward labeling method with a combination of chelators and suitable radiometals. In contrast to small molecules, antibodies are not able to cross the plasma membrane for intracellular targets, so they are limited to the tumor cell surface. Their inherently huge size of approximately 150 kDa is the main cause of the suboptimal pharmacokinetics with high blood pool background leading to late imaging time points. Additionally, they might have an inadequate tumor penetration. The use of mini- or nanobodies, or fragments of antibodies, partially solves this issue but their use is still limited to surface structures and proteins and does not reflect on metabolic processes but offers a mere quantification of the target. Thus, radiolabeled small molecules are in many cases favored due to their superior biodistribution.

PET utilizing the glucose analogue 2-deoxy-2-[^{18}F]fluoro-D-glucose (FDG) is the gold-standard for cancer diagnosis. Here, the high glucose consumption of cancerous cells (Warburg effect) is exploited as [^{18}F]FDG is taken up by cancer at a much higher rate compared to healthy cells. [^{18}F]FDG is a glucose analogue where the hydroxyl group at C2 is replaced by ^{18}F. Inside the cells, [^{18}F]FDG is phosphorylated but further metabolization is prevented by the lack of the C2 hydroxyl group, thus trapping the radioactive molecule. This in turn leads to a higher accumulation and stronger radioactive signal in cancer cells.

Although [^{18}F]FDG is the most-used radiopharmaceutical in standard clinical care, it only yields information about glucose uptake and thus energy consumption and metabolism rate. Besides, the brain generally has a high glucose demand, so visualization of brain tumors is challenging. To determine susceptibility for certain treatments or characterize the TME, other radiopharmaceuticals are being developed or already in clinical use. Well-known examples of other radiopharmaceuticals are prostate-specific membrane antigen (PSMA)-targeting radiotracers that are used in prostate cancer diagnosis or fibroblast activation protein (FAP)-targeting radiotracers, a protein that is highly upregulated in the stroma content by tumor-associated fibroblasts in various cancers.[203,204] These have the advantage that the PET scans following the initial diagnosis yield additional information about expression of specific targetable antigens for combination with radiotherapy, or about other metabolic processes besides glucose metabolism.

By 2016, ten small molecule radiotracers were approved by the FDA and available for clinical use, and way more are in clinical trials on their way to the patient's bedside. The development of novel radiotracers often utilizes specific inhibitors or pharmacophores as

basis. One prerequisite for a successful radiotracer are suitable pharmacokinetic properties, the processing of the radiotracer within the body. The pharmacokinetics need to be investigated to gain information about absorption, distribution, metabolism, and excretion kinetics and pathways (also known as ADME). Equally important is the pharmacodynamic, how the radiotracer engages with the target. The effects of the body on the radiotracer is negligible for PET imaging due to only trace amounts of radioactive compound in the body.

A particular challenge in radiotracer development is the blood-brain barrier (BBB), the body's protection mechanism of the brain from toxic compounds and pathogens. Many radiotracers show excellent pharmacokinetic distribution but are unsuitable for most brain application as they are unable to cross the BBB. Generally, radiotracers that readily cross the BBB without transporters are small and lipophilic compounds, as those properties mediate passive diffusion over the BBB.[205,206] However, even if the compounds are able to reach the brain, they might still be effluxed too fast to bind to the target structure. Notably, one of the most challenging brain efflux transporters is the ATP-dependent P-glycoprotein (PgP), due to its high diversity of substrates.[207]

Brain penetration is of particular interest for brain metastasis and brain tumors, since while the BBB can be disrupted during late stages of the disease, early detection in stages where the BBB is still fully intact would greatly benefit the patients. Thus, brain delivery of radiopharmaceuticals should be kept in mind during radiotracer development, especially when targeting a pathway that is of general importance in all types of tumors like replicative stress.
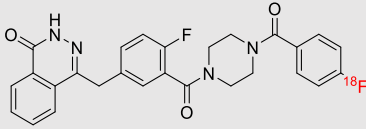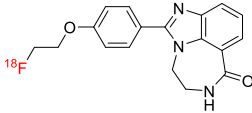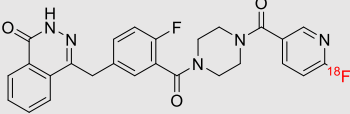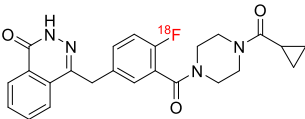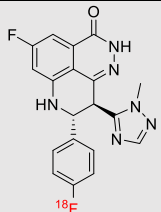
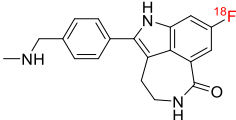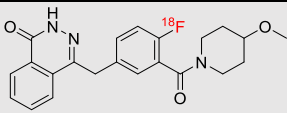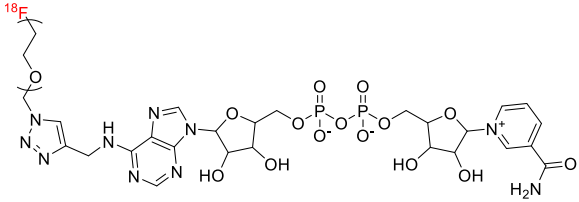## 1.5.1 PARP Radiotracers for Replicative Stress

So far, no radiotracer for replicative stress has been developed. However, there are several radiotracers that might be repurposed for imaging of replicative stress. In this work, PARP will be evaluated as potential biomarker for replicative stress. The aforementioned PARP inhibitors have proven their clinical merit as radiotracers in detection and delineation of tumors. Thus far, several radiolabeled PARP inhibitors are in preclinical or clinical use (Table 2). The olaparib-derived [^{18}F]PARPi, together with rucaparib-based [^{18}F]fluorthanatrace (FTT), are considered the current gold-standard of clinical PARP imaging and even outperformed [^{18}F]FDG in patients with head-and-neck cancer.[208-212] An alternative to [^{18}F]PARPi featuring a reduced logP, [^{18}F]FPyPARP was developed in our lab and evaluated preclinically within the scope of this work.[213] Since both the structures of olaparib and talazoparib already include fluorine, the synthesis and evaluation of [^{18}F]olaparib and [^{18}F]talazoparib were published during and within this work, respectively.[214-217]

A PARP imaging agent which is not based on one of the clinically relevant PARP inhibitors is [^{18}F]SuPAR, a NAD$^+$ analogue which serves as a substrate for PARylation by PARP1.[218]

INTRODUCTION

PARP activity imaging in combination with assessing the absolute protein expression could provide the added benefit of understanding the modulation of PARP expression and activation in response to DNA damage, replicative stress and tumor therapy. However, the molecule is quite bulky and it is metabolized relatively quickly already in mouse serum. As NAD+ is a common metabolism substrate, it might as well be quickly metabolized by liver metabolism and tumor uptake might be an effect of increased metabolism.

Table 2: Structures of PARP radiotracers.

NAME	STRUCTURE	DERIVED FROM	FIRST REPORT
[18F]PARPi		Olaparib	2016[209]
[18F]FluorThana-trace		Rucaparib	2016[219]
[18F]FPyPARP		Olaparib	2022[213]
[18F]Olaparib		Olaparib	2019[217]
[18F]Talazoparib		Talazoparib	2021[220]
[18F]Rucaparib		Rucaparib	2021[221]
[18F]AZD2461		Olaparib	2020[222]
[18F]SuPAR		NAD+	2019[218]

Here, we aimed to correlate PARP radiotracer uptake with replicative stress. As it was unclear whether we will find a correlation between PARP and replicative stress, we extended the search to include fallback options. An alternative way to quantitatively and longitudinally assess replicative stress could be the use of so-called reporter gene systems (RGS). These versatile biological tools could also be used for the construction of *in vitro* and *in vivo* models for drug development and evaluation while no specific imaging biomarker is available.

1.6 Reporter Genes

RGS have been utilized extensively in biochemical research. They played a vital role in shedding light on important biological processes like the UPR and are still of immense importance. Since decades, new, improved generations of diverse RGS have been developed and optimized for various purposes, from genetically engineered cells to transgenic mouse models.[223,224] An impressive example of reporter gene application is the development of the 'brainbow' transgenes, inducing combinatorial expression of three distinct fluorescent proteins allowing for visualization of individual neurons in 90 different colors.[225]

RGS translate biological processes in detectable and quantifiable physical properties like emission of light, fluorescence or bioluminescence. As such, either the encoded reporter itself is detectable as it is the case for fluorescent protein like green fluorescent protein (GFP) or it can be tracked by specific ligands that for example emit light upon metabolization (luciferin) or radioactive radiation.[226,227] Through the specific detection of a particular protein and thus assessment of its expression levels, RGS can also assess promotor or enzyme activity, protein stability or mRNA splicing.[228,229]

While the traditional application of RGS, in particular fluorescent and bioluminescent RGS, is *in vitro*, the use of RGS *in vivo* has opened up opportunities to study biological processes in living animals. Optical reporters are physically limited by the penetration depth and scattering in tissue, which is only partially improved by the use of near-infrared dyes; thus, this technique is only suitable for superficial applications.[230-232] Due to their non-invasive application and excellent physical properties for detection, reporters used for or with MRI, SPECT/PET and ultrasound have gained significant attention.

MRI reporters can manipulate water content or properties and thus improve the diffusion weighted contrast in tissue, like overexpression of aquaporin1 or the urea transporter. Alternatively, they enhance MRI contrast by accumulation of iron particles (ferritin or transferrin receptor) or contrast agents.[233-236] Human Organic Anion Transporting Polypeptide 1B3 (OATP) is presumably one of the most frequently used MRI reporters. Originally expressed in the liver, OATP mediates uptake of the gadolinium-based contrast agent Primovist.[237] But, in contrast to aquaporin-1 or the urea transporter, it still requires additional injection of a contrast agent.

More recently, gas vesicle-based acoustic reporters have emerged as a powerful tool for ultrasound or MRI detection. Gas vesicles are produced in aquatic bacteria for floating purposes to ensure optimal photosynthesis. Cells genetically encoded to produce gas vesicles can be tracked *in vivo* using ultrasound.[238] They can also be modified for MRI by introducing hyperpolarized ^{129}Xe.[239] This field only recently started to gain traction, and more developments and applications are anticipated in the next years.

PET reporter gene imaging has the great advantage of superior sensitivity as it can detect changes in radiotracer uptake in the nanomolar range compared to MRI reporters that require rather large probe quantities (millimolar range).[240] The combination of excellent spatial and temporal resolution, the chemical versatility in radiotracer design and the high sensitivity and specificity render nuclear RGS most suitable as a platform for the development of a RGS for replicative stress.

1.6.1 State-of-the-Art Reporter Genes for PET Imaging

One of the most prominent examples for a nuclear RGS in preclinical use is *herpes simplex virus* type 1 thymidine kinase (HSV1-tk), the mutant form HSV1-sr39tk optimized for therapy and imaging, and the respective radiotracers 2'-deoxy-2'-[^{18}F]fluoro-1-beta-D-arabinofuranosyl-5-iodouracil ([^{18}F]FIAU) and 9-(4-[^{18}F]fluoro-3-hydroxymethylbutyl)guanine [^{18}F]FHBG.[241-244] This RGS has already successfully been utilized in many studies, for example to track the fate of different cell types in a reporter mouse or of cytotoxic T cells during immunotherapy in a case study.[241,245] Another prominent application is monitoring of therapeutic gene delivery, as HSV-tk has been used as a suicide gene for ganciclovir treatment.[246,247] Although [^{18}F]FHBG has a favorable biodistribution and performance, it does not readily cross an intact BBB and is thus only suitable for the use in the periphery.[248]

Other examples for PET RGS include pyruvate kinase M2 (PKM2) and the radiotracer [^{18}F]DASA-23.[249] It has proven very promising as a brain reporter due to low endogenous background, however, PKM2 is highly upregulated during inflammatory processes and brain cancers, rendering it unsuitable for the diseased brain.[250] Indeed, [^{18}F]DASA-23 has been successfully utilized to delineate high grade glioma from healthy brain tissue in mice and humans.[251,252]

The highly specific bacterial dihydrofolate reductase (DHFR) inhibitor trimethoprim (TMP) has not only been exploited as antimicrobial treatment but also labeled with the PET isotopes ^{11}C and ^{18}F for PET imaging of DHFR for imaging of bacterial infection and as a reporter.[253-255] Although both radiotracers are reported to cross the intact BBB, uptake of [^{18}F]TMP in transduced DHFR-expressing brain regions is rather low.[256]

An example for a combined PET and SPECT RGS is the sodium iodide symporter (NIS) using ^{99m}Tc pertechnetate or ^{131}I as ligand.[257] It also can serve a dual purpose and accumulate the radioisotopes in therapeutic doses, causing NIS-expressing tumors to shrink in a xenograft model.[258] Complementarily, the PET isotope ^{124}I can be used instead, and the NIS-specific radiotracer [^{18}F]tetrafluoroborate has been utilized for NIS PET imaging in clinical trials.[259,260]

More recently, PSMA and the commercially available ^{18}F-labeled PSMA radiotracer [^{18}F]DCFPyl have emerged as PET RGS.[261,262] Besides being an excellent tumor marker for

prostate cancer, PSMA features very low endogenous expression outside of the prostate and prostate cancer-derived metastasis. Most conveniently, [^{18}F]DCFPyl has already been approved by the FDA for human use, and other PSMA radiotracers like [^{68}Ga]PSMA-11 and [^{18}F]PSMA-11 are in clinical studies, thus, repurposing should facilitate the approval for applications like CAR T cell therapy surveillance.[263-265] Additionally, PSMA-targeted radiotherapeutics could be used as a safety switch to specifically kill PSMA-CAR T cells in case of cytotoxic effects from the therapy.[266] Despite outperforming the HSV-tk and NIS RGS in direct comparison, PSMA is a large protein of 100 kDa, limiting the application to the available vector size.

The concept of multimodal reporters promises even further advantages. Multimodal reporters combine two or more modalities in either one dual-purpose reporter or in one genetic construct that combines two distinct reporters. With this, disadvantages of single reporters can be evened out, and reporter detection can be adjusted to the circumstances.

OATPs, which have been presented previously in the context of MRI RGS, can actually serve a multimodal purpose as they also mediate uptake of the near-infrared dye indocyanine green.[267] Furthermore, the gadolinium atom in the contrast agent complex has been successfully exchanged to the SPECT isotope ^{111}In, combining the advantages of both MRI and SPECT.[268] In theory, it could also be exchanged with ^{68}Ga enabling PET imaging, but ^{18}F-labeled small molecule radiotracers are avaliable.[269,270]

As example for trimodal RGS imaging, CAR T cells expressing the PET reporter DHFR, yellow fluorescent protein and *Renilla* luciferase as a bioluminescence reporter were tracked *in vivo* using all three modalities.[271] This approach features all the advantages of the different modalities, however, genome capacity must be kept in mind and the modalities can differ drastically in their sensitivity, requiring careful design of the multimodal construct.

There are more PET RGS available that can not be covered in this brief overview, and all of the PET reporters have their distinct drawbacks and benefits. All of the mentioned RGS find their use in assessment of successful gene transfer and in particular in *in vivo* cell tracking of engineered immune cells. However, they have their disadvantages in different aspects, like insufficient radiotracer BBB penetration, limiting applications; endogenous expression of the reporter in healthy or diseased tissue; or low sensitivity. This warrants the development of novel RGS with the goal to minimize the drawbacks and maximize the applicability.

1.6.2 Challenges

A particular challenge in RGS research is the limited applicability in the brain. Although a wide range of nuclear RGS is available for oncological research, RGS dedicated to neurological applications are limited. For some RGS, like HSV1-sr39tk and [^{18}F]FHBG, the radiotracer is not able to cross the intact BBB and the reporter expression leads to

immunogenicity.[248,272] Others suffer from low uptake in the target region, or have high background in the whole body except the brain, limiting their use to the brain only. The reporter protein can also be upregulated during inflammatory processes or in brain cancer, like PKM2 and [^{18}F]DASA-23, and is thus limited to healthy brain tissue.

While the BBB is often compromised in later stages of brain cancer or neurodegenerative diseases like Alzheimer's or Parkinson's disease, early metastases do not yet or only partially disrupt the BBB.[273-275] Especially for brain metastases that are usually associated with poor prognosis, early detection is crucial for successful treatment.[276] There are studies linking inhibition of replicative stress-involved proteins in brain metastases with sensitization to radiation therapy.[277,278] In addition, levels of replicative stress in brain metastases could be altered or be similar in comparison to the primary tumor, an information that could affect the therapy regimen drastically.[279]

Thus, as replicative stress is not yet fully characterized, intertwined with many other pathways, and the implications for brain metastases are unknown, it is important to investigate all aspects within the whole body. As stated in the previous chapters, there are candidates for a specific biomarker; nevertheless, a versatile RGS as stress reporter would aid the development and validation of potential biomarkers.

In consequence, BBB permeability must be considered when designing a novel reporter radiotracer for stress applications, in order to yield a universal RGS that is not limited to certain tissues and can assess also early changes in stress levels in brain metastasis. Additionally, the general properties of the reporter gene itself and its ligand need to be chosen carefully to not limit the applicability of the RGS.

1.6.3 Covalent Reporter Genes

Besides general considerations about the reporter's size and origin, the binding of the ligand can be either reversible or irreversible. The advantage of using a covalent RGS is the potential for signal retention at the target. Ideally, the covalent bond between ligand and reporter for non-invasive PET imaging should be also irreversible, in order to avoid dissociation of the ligand. The off-target binding of the RGS can be further reduced by choosing reporter proteins that are not endogenous to the body or have low endogenous expression. Generally, the reporter sequence should be relatively small to not interfere with the protein folding or pathway it is reporting on and to retain flexibility in vector design in regard to genome capacity. Another important factor is immunogenicity, which is depending on the envisioned application. If the RGS is planned to be applied in humans and is immunogenic, it can have adverse effects within the patient and lead to fast elimination of the transduced cells.

Ligand design is equally important for PET imaging. The most versatile ligand is a small molecule that can cross the plasma membrane, enabling both intra- and extracellular applications, penetrates the BBB and has favorable excretion pharmacokinetics. In addition, the ligand should bind the reporter covalently and with high specificity and selectivity.

We thus envisioned the future ligand for a novel RGS to be small and slightly lipophilic for potential BBB penetration, and to have a site suitable for labeling with ^{18}F, our isotope of choice due to its convenient physical properties. In this work, we focused on the three covalent protein reporters HaloTag, SNAPTag and CLIPTag.

1.6.3.1 Development and Applications of HaloTag

HaloTag is a self-labeling protein originally derived from DhaA, a dehalogenase from the gram-positive soil bacterium *Rhodococcus rhodochrous*. As indicated by the name, dehalogenases catalyze the conversion of a haloalkane to its respective hydrogen halide and alcohol.[280] It has been shown for a different dehalogenase from *Xanthobacter* (DhA) that a histidine moiety in the enzyme's active center catalyzes cleavage of the formed ester bond with the ligand, but is not necessary for the initial nucleophilic attack.[281] Thus, the HaloTag is engineered to carry a Phe272 in the active center instead of His272, preventing cleavage of the ligand.[282] This leads to formation of a covalent bond between HaloTag and the respective HaloTag ligands (HTLs) which has been exploited to attach all kinds of detectable labels to the HaloTag.

The HaloTag is widely used in biological research for protein purification, studying protein interactions and function, cellular status, live cell and even *in vivo* imaging.[283,284] Often, the HaloTag is fused to and co-expressed with a protein of interest to study specific pathways. The chemical versatility of HTLs is directly linked to the applications. Straightforward labeling of the HaloTag with fluorescent or radiolabeled probes is mainly used to study protein expression while protein-protein interactions are investigated using Foerster or bioluminescence resonance energy transfer.[285] Importantly, the HTL structure is very versatile as it only requires a chloroalkane moiety to react with the HaloTag. Due to the robustness of the enzyme, it can be employed for both extra- and intracellular applications.[286,287]

In vivo, fluorescent HTLs have been used for tumor detection to overcome limitations of fluorescent proteins since HaloTag can be targeted flexibly with various different fluorophores.[288] PET imaging of HaloTag has been attempted before as well, but the ^{64}Cu-labeled HTL used in this study is bulky and the biodistribution was not suited for brain imaging.[289]

Despite being of bacterial origin, therefore more likely to be immunogenic, the HaloTag and HTLs feature a very promising platform for the development of a nuclear brain RGS. HaloTag

itself is relatively small, and the enzymatic reaction is fast, specific and covalent.[282] HTLs are chemically versatile and can be modified heavily without losing the affinity to the HaloTag. For this work, we designed a minimalist HTL that consists of only the haloalkane moiety and a site for ^{18}F-labeling ([^{18}F]fluorobenzoyl-HaloTag ligand, [^{18}F]FB-HTL, Figure 7).
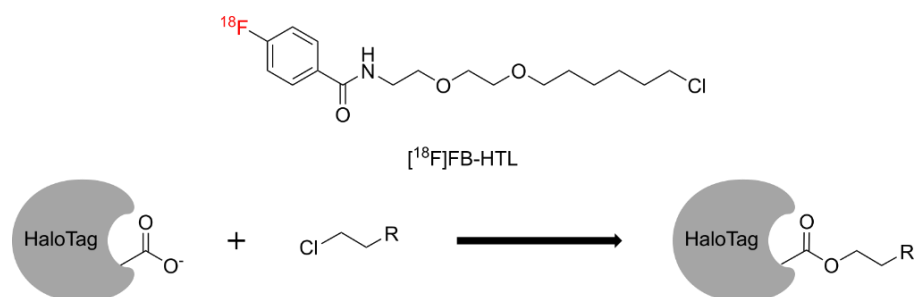

Figure 7: Structure and principle of the HaloTag radiotracer.

1.6.3.2 Development and Applications of SNAP- and CLIPTag

As HaloTag is a bacterial enzyme, alternative protein tags suitable for brain RGS development we decided to investigate alternatives that are based on human enzymes for potential translatability.

SNAPTag is an optimized version of human O^6-alkylguanine-DNA alkyltransferase (AGT), a suicide DNA repair enzyme that recognizes and repairs methylated guanines as part of the direct DDR. AGT restores the guanine by transferring the methyl group onto itself, in consequence the enzyme is ubiquitinylated and degraded.[290] The substrate specificity of original AGT is relatively low, thereby also accepting benzylguanines (BGs) and other derivatives in addition to alkylguanines.[291] AGT can be predictive of chemotherapy efficacy as higher expression leads to better repair of DNA lesions from alkylating agents.[292] In order to visualize AGT expression and activity with PET, O^6-BG derivatives have been radiolabeled but no follow-up studies in mice or humans have been published.[293-295]

Initially, AGT fusion proteins themselves were selectively labeled with BG derivatives.[296,297] SNAPTag was obtained by directed evolution to optimize specificity and kinetics.[298] It features increased reactivity with O^6-BG derivatives and low DNA interaction.[299-301] Similarly to HaloTag, SNAPTag is used in biochemical assays to determine protein-protein interactions, label proteins of interest site-specifically or for live cell imaging.[302,303]

During this work, SNAPTag radiotracers for PET imaging have been disclosed within the scope of this work and independently by two other groups (Figure 8 B).[304-306] The published radiotracers show high specificity and good *in vivo* tumor uptake in SNAPTag-expressing tumors. However, the pharmacokinetic properties need to be further improved, as they all suffer from high abdominal radiotracer uptake or defluorination.

CLIPTag was developed as an 'add-on' to SNAPTag, allowing for simultaneous labeling of two different proteins. CLIPTag is an AGT derivative as well, orthogonal to SNAPTag, that

was designed to accept *O*[6]-benzylcytosines (BCs) as ligands (Figure 8 C).[307] As SNAPTag, it has demonstrated exceptionally high specificity and enzyme kinetics which allows the complimentary use of both SNAP- and CLIPTag without undesired cross-reactivity to study for example protein-protein interactions in more detail.[308]
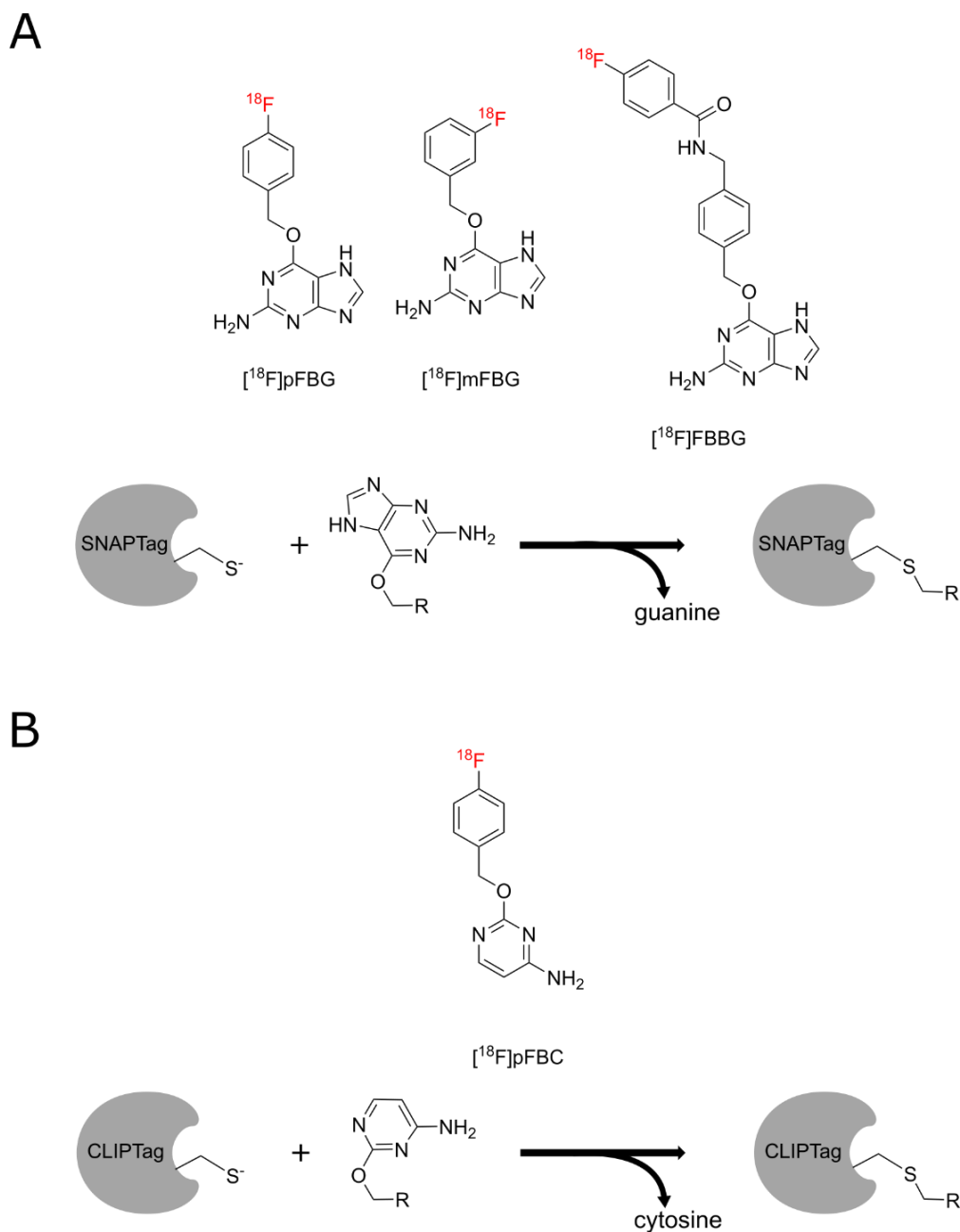
Figure 8: Structures of the SNAP and CLIP radiotracers developed in this work and schematic of the biochemical principle. A Structures of the three SNAPTag radiotracers [18F]*p*FBG, [18F]*m*FBG, and [18F]FBBG and principle of SNAPTag irreversibly binding benzyl guanine derivatives and releasing guanine in the process. **B** Structure of [18F]*p*FBC and the principle of CLIPTag which is similar to SNAPTag but using benzyl cytosine derivatives.

Here, we again decided to keep the SNAP- and CLIPTag ligands as simple and small as possible, only including the BG or BC binding site and a site for 18F-labeling (see Figure 8 for

structures, 6-((4-[^{18}F]fluorobenzyl)oxy)-9H-purine-2-amine: [^{18}F]pFBG, 6-((3-[^{18}F]fluorobenzyl)oxy)-9H-purine-2-amine: [^{18}F]mFBG, N-(4-(((2-amino-9H-purine-6-yl)oxy)methyl)benzyl)-4-[^{18}F]fluorobenzamide: [^{18}F]FBBG, 6-((3-[^{18}F]fluorobenzyl)oxy)-9H-pyrimidine-2-amine: [^{18}F]pFBC).

Like HaloTag (33 kDa), SNAP- and CLIPTag are relatively small protein tags (20 kDa) and bind their respective ligands covalently. Thus, the reporter protein coding sequences can easily be cloned into vectors that have limited genome capacity and are very unlikely to interact with biological pathways. The ligands can be designed to be small and lipophilic to potentially penetrate the BBB and might be also suitable for intracellular targets. Additionally, all three reporter proteins can be labeled with established fluorescent ligands, allowing for multiscale imaging. Interestingly, in a head-to-head comparison of HaloTag, SNAPTag and CLIPTag and their respective improved variants, there are some differences in reaction kinetics.[309] These differences are dependent on the charge and size of the ligands and the engineering method for the optimized ligands. While HaloTag reacts faster with rhodamine-based ligands, SNAPTag binds most non-fluorescent ligands faster. However, this comparative study was based on *in vitro* assays, thus, the reaction kinetics and affinity might change drastically *in vivo*. In this work, we aimed to develop a novel PET RGS that is suitable for whole-body PET imaging. This RGS could serve as a platform to develop an RGS specific for replicative stress in addition to our attempts to directly visualize replicative stress.

2. AIM OF THE WORK

This work investigates several different ways to visualize replicative stress. First, by direct PET imaging with PARP radiotracers in various cell models, since PARP is a highly promising candidate to be a replicative stress biomarker. Alternatively, several potential biomarkers that could be targetable with small molecules were evaluated for their correlation with levels of replicative stress with Western blot analysis. Second, we aimed to develop and characterize three different RGS that can be used in biological models of replicative stress to circumvent a potential lack of a specific biomarker. In addition, the RGS were tested for their ability to serve as brain RGS, as the BBB is one of the most challenging obstacles in the body. This would also open up their applicability beyond replicative stress.

We decided on ^{18}F as the PET isotope of choice for both the PARP radiotracer development and the RGS ligand design and synthesis. This is due to several reasons: ^{18}F features a convenient half-life of 109 minutes, and has a favorable positron range of 0.6 mm only.[195] Additionally, this isotope is readily available in our laboratories. Generally, small molecules have tunable biodistribution, excellent tissue penetration and short biological half-life suitable for short-lived isotopes. ^{18}F-labeling is fast, efficient and many small molecule pharmaceuticals already have a replaceable fluorine or a site suitable to attach the label.

2.1 Novel Radiotracers for PARP Imaging

As the clinical interest in PARP imaging is on the rise, optimization and development of novel PARP-targeting radiotracers is warranted. [^{18}F]PARPi, the gold-standard for PARP imaging, suffers from high liver uptake, limiting its use for hepatocellular carcinoma and liver metastasis.[209] In order to lower the lipophilicity and expand the clinical scope we thus exchanged the labeling site from a fluorobenzoic acid to a fluoronicotinic acid and evaluated the resulting novel radiotracer [^{18}F]FPyPARP.[213] We expected this change to shift the clearance route towards more renal clearance. For comparison reasons, we also established the synthesis of [^{18}F]FTT, another gold-standard PARP radiotracer based on a different PARP inhibitor, in our laboratories.

The direct comparison between radiolabeled olaparib and talazoparib isotopologues was of particular interest, since olaparib was the first approved PARP inhibitor and is still heavily used in cancer treatment. Talazoparib, the latest approved PARP inhibitor, is considered a "next-generation" PARP inhibitor with 100-fold improved PARP trapping capacity. We aimed to compare the two of them to investigate whether the improved PARP trapping capacity also impacts PARP PET imaging. During this work, the synthesis of isotopically labeled [^{18}F]olaparib was disclosed by Wilson et al.[217] which we significantly optimized and adapted. Shortly after, we established the synthesis of [^{18}F]talazoparib.[214]

To perform a reliable head-to-head comparison between the five PARP radiotracers in our laboratories, the same tumor model and imaging time points were used. We chose the BRCA1-mutated breast cancer cell line HCC1937 since they were already successfully used for the preclinical evaluation of [^{18}F]FTT and present with high PARP expression in Western blot analyses.[219] First, the radiotracers were evaluated for their *in vitro* uptake in HCC1937 cells and subsequently in a xenograft model utilizing immunodeficient mice. In the *ex vivo* analysis, the residual activity in selected organs and the dynamic distribution was assessed with particular focus on tumor retention of the radiotracers and the different excretion routes to identify the best applications for the five different radiotracers.

2.2 Identification of Biomarkers for Replicative Stress

We hypothesized that PARP is a key player in replicative stress and that PARP levels reflect replicative stress levels present in tumor cells. Thus, we tested several cell lines with high and low replicative stress for their PARP levels by Western blot and uptake of PARP radiotracers. Here, several different cell models were used. The first cell models were based on myc overexpression and provided by our collaboration partners. Initially, two pancreatic ductal adenocarcinoma (PDAC) cell lines with high and low myc expression were generated for first evaluations. Then, liver progenitor cells were transfected with either Kras and myc or only Kras (high and low replicative stress) for further experiments. The next step were two patient-derived cell lines from the NCI60 panel that have been previously tested for their levels of replicative stress.[310]

In parallel, we aimed to generate a more universal cell model for replicative stress, since myc overexpression might not be specific and influences other metabolic or stress-related pathways. Therefore, we generated mIDH overexpression cell models with two different cancer cell lines as we hypothesized that mIDH and subsequently produced oncometabolite 2-HG plays a role in replicative stress and induces susceptibility to PARP inhibition.[62] Furthermore, cells in which replicative stress was induced chemically following published procedures with the topoisomerase I inhibitor camptothecin (CPT) or with hydroxyurea (HU) were used according to literature as fast, simple and peer-reviewed control model.[109,311,312]

PARP enzymes are heavily involved in the DDR. Thus, we could not exclude that PARP might not be a specific marker for RS, so we tried to identify novel, potentially more specific, biomarkers. We used Western blot analysis of cell lysates with chemically induced replicative stress to quantify protein levels of biomarker candidates. We decided to test for ATR and ATM, APOBEC, CHK1, and Wee1 levels.

2.3 Development of Novel PET Imaging Reporter Gene Systems

As an alternative, we set out to investigate novel nuclear RGS to bypass potential challenges with the identification of specific biomarkers for replicative stress. As replicative stress plays a great role also in neuro-oncology and neurological diseases, an RGS that is universally applicable in the whole body is essential. The most challenging organ for drug and radiotracer delivery is the brain. Therefore, we chose three different RGS with small covalent ligands that were suitable for radiolabeling with ^{18}F to have a set of fallback options. First, the radiosynthesis of a total of five RGS radiotracers was established: [^{18}F]FB-HTL for HaloTag, [^{18}F]*p*FBC for CLIPTag, and [^{18}F]*p*FBG, [^{18}F]*m*FBG, as well as [^{18}F]FBBG for SNAPTag. We first assessed reporter-specific uptake extensively *in vitro* and *in vivo* in a pilot tumor study in immunodeficient mice. As BBB penetration for [^{18}F]FB-HTL and [^{18}F]pFBC was confirmed in the subcutaneous tumor study, specific brain uptake with these two RGS was investigated using adeno-associated virus (AAV)-mediated gene transfer to striatal neurons.

3. MATERIALS AND METHODS

3.1 Chemistry

All reagents and solvents used in this work were purchased from commercial suppliers and used without further purification if not stated otherwise. High performance liquid chromatography (HPLC) columns were obtained from Phenomenex (Torrance, CA, USA). Solid-phase extraction cartridges were purchased from Waters (Milford, MA, USA) if not stated otherwise. Electrospray ionization mass spectrometry (ESI-MS) analysis was performed on a 1200 series HPLC system (Agilent, Waldbronn, Germany) equipped with a 6120 quadrupole ESI mass spectrometer. Nuclear magnetic resonance (NMR) spectra were acquired using a 600 MHz Avance III spectrometer (Bruker Biospin, Ettlingen, Germany).

For this work, a total of ten radiotracers and their respective precursors and non-radioactive standard compound were synthesized (Table 3). Compound designs and synthesis strategies were developed by Dr. Andreas Maurer, Dr. Gregory D. Bowden and Dr. Jonathan M. Cotton. Organic syntheses were performed by Dr. Gregory D. Bowden, Dr. Jonathan M. Cotton, Johannes Kinzler and Dr. Andreas Maurer.

Table 3: Overview of the radiotracers, their precursors and non-radioactive standards used in this work.

RADIOTRACER	PRECURSOR	STANDARD	TARGET
[^{18}F]PARPi	1	PARPi	PARP1/2
[^{18}F]FTT	2	FTT	PARP1/2
[^{18}F]FPyPARP	1	FPyPARP	PARP1/2
[^{18}F]Olaparib	3	Olaparib	PARP1/2
[^{18}F]Talazoparib	4	Talazoparib	PARP1/2
[^{18}F]FB-HTL	5	FB-HTL	HaloTag
[^{18}F]*p*FBC	6	*p*FBC	CLIPTag
[^{18}F]*p*FBG	7, DGC	*p*FBG	SNAPTag
[^{18}F]*m*FBG	8, DGC	*m*FBG	SNAPTag
[^{18}F]FBBG	BG-NH$_2$	FBBG	SNAPTag

3.1.1 Precursor and Standard Syntheses for PARP Radiotracers

Precursors **1** and **2** and PARPi, FTT and FPyPARP were prepared according to published literature from Stotz et al.[213]

Precursor **3** was synthesized as described by Bowden et al.[313]

Precursor **4** was prepared according to literature by Bowden et al.[214]

Olaparib and talazoparib were purchased from Hoelzel Biotech (Cologne, Germany) and used without further purification.

3.1.9 Precursor and Standard Syntheses for Reporter Radiotracers

*Precursor **5** (FB-HTL precursor)*

Precursor **5** was synthesized and purified as previously described.[314] 2-[2-(Boc-amino)ethoxy]ethanol was deprotonated with NaH and reacted with 6-chloro-1-iodohexane. The product was purified using silica chromatography, deprotected with trifluoroacetic acid (TFA) and again purified by silica chromatography. Product identity was confirmed using ^{1}H NMR and mass spectrometry.

^{1}H NMR (600 MHz, Chloroform-*d*) δ 3.77 (t, *J* = 5.1 Hz, 2H), 3.69 – 3.65 (m, 2H), 3.59 – 3.56 (m, 2H), 3.53 (t, *J* = 6.7 Hz, 2H), 3.48 – 3.45 (m, 2H), 3.19 (t, *J* = 5.0 Hz, 2H), 1.77 (p, *J* = 7.0 Hz, 2H), 1.59 (p, *J* = 6.8 Hz, 2H), 1.44 (td, *J* = 10.0, 9.0, 5.7 Hz, 2H), 1.40 – 1.36 (m, 2H). ESI-MS (m/z) calc. [M+H]$^+$ 224.14, found 224.2.

FB-HTL

Fluorobenzoic acid (1 eq, 1 mmol, 140 mg) was added to a solution of 224 mg of precursor **5** (1 eq, 1 mmol) and diisopropyl ethylamine (DIPEA, 9.2 eq, 9.2 mmol, 800 µL) in 10 mL dichloromethane (DCM). Then, 1-ethyl-3-(3-dimethylaminopropyl)carbodiimide (EDC, 1.1 eq, 1.1 mmol, 211 mg) was added and reacted at room temperature for 4 h. The reaction mixture was diluted with water and extracted with DCM. The organic phase was sequentially washed with saturated bicarbonate and 2 M HCl. Solvents were evaporated under reduced pressure and 20 µL of the resulting oil were further purified by preparative HPLC on a Luna C18(2) column (250 mm × 10 mm, 100 Å, 10 µm) on a 1260 Infinity HPLC system (Agilent). Identity was confirmed by ^{1}H NMR and LC-MS analysis.

^{1}H NMR (600 MHz, Chloroform-*d*) δ 7.87 – 7.73 (m, 2H), 7.16 – 7.03 (m, 2H), 6.81 (s, 1H), 3.71 – 3.64 (m, 6H), 3.62 – 3.57 (m, 2H), 3.51 (t, *J* = 6.7 Hz, 2H), 3.46 (t, *J* = 6.7 Hz, 2H), 1.74 (dt, *J* = 14.5, 6.7 Hz, 2H), 1.56 (dt, *J* = 14.5, 6.8 Hz, 2H), 1.48 – 1.38 (m, 2H), 1.37 – 1.28 (m, 2H). ESI-MS (m/z) calc. [M+H]$^+$ 346.15, found 346.1, calc. [M+Na]$^+$ 368.15, found 368.1.

Precursor **6** and *p*FBC were prepared according to literature by Bowden et al.[315]

Precursor **7** and **8,** *p*FBG, *m*FBG and FBBG were synthesized according to literature by Stotz et al.[306] BG-NH$_2$ was purchased from AA Blocks (San Diego, CA, USA and used without further purification.

3.2 Radiochemistry

[^{18}F]Fluoride was produced on a medical cyclotron (PETtrace 800, GE Healthcare, Uppsala, Sweden) using the ^{18}O(p,n)^{18}F nuclear reaction and trapped in the respective synthesizer on an ion exchange cartridge (Sep-Pak Plus Light QMA Carb) preconditioned with 10 mL 1 M

NaHCO$_3$ and 10 mL H$_2$O unless stated otherwise. Radiotracer syntheses were performed on a modified TRACERlab (GE Healthcare) ([^{18}F]PARPi, [^{18}F]FTT, [^{18}F]FPyPARP, [^{18}F]FB-HTL, [^{18}F]FBBG), a TRACERlab FX N Pro ([^{18}F]olaparib, [^{18}F]talazoparib, [^{18}F]pFBC), or an Elixys FLEX/CHEM ([^{18}F]olaparib, [^{18}F]talazoparib, [^{18}F]pFBG, [^{18}F]mFBG) radiochemical synthesizer with PURE/FORM HPLC module. The synthons N-succinimidyl 4-[^{18}F]fluorobenzoate ([^{18}F]SFB) and 2,3,5,6-tetrafluorophenyl 6-[^{18}F]fluoronicotinate ([^{18}F]FPyTFP) was available as an established radiosynthesis on our modules.

Radiotracer identity and purity were confirmed using a 1260 Infinity II HPLC system (Agilent) with radioactivity detector. Radiochemical purity (RCP) was additionally assessed by radio-thin layer chromatography. Molar activity (MA) was calculated from the HPLC chromatograms using previously obtained calibration curves. The final products were eluted with 0.5 mL EtOH and formulated for in vivo application with 4.5 mL phosphate-buffered saline (PBS, ThermoFisher Scientific, Waltham, MA, USA) if not stated otherwise.

Radiosyntheses were performed by Gregory D. Bowden, Jonathan M. Cotton, Johannes Kinzler, Elena Kimmerle, and Ramona Stremme. Data on decay-corrected radiochemical yield (RCY), radiochemical purity (RCP) as determined by radiography thin layer chromatography (radio-TLC) and molar activity (MA) of the individual radiotracers are provided in Table 12 for the PARP radiotracers and Table 13 for the reporter radiotracers.

3.2.1 Radiosyntheses of PARP Radiotracers
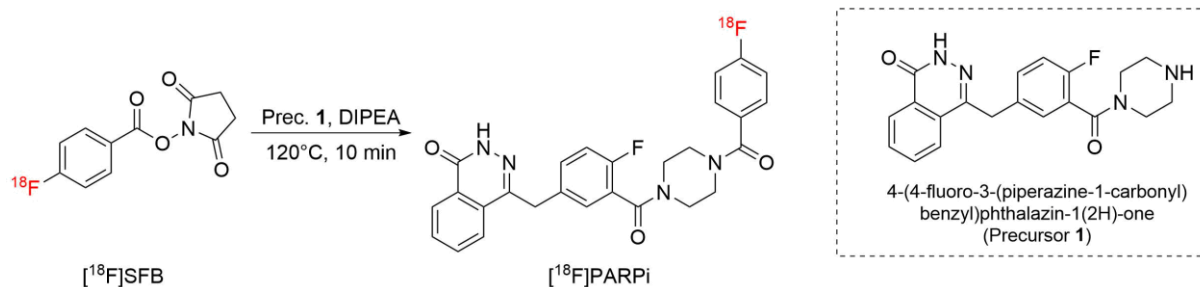
Figure 9: [^{18}F]PARPi radiosynthesis.

[^{18}F]PARPi was synthesized according to Stotz et al.[213] Briefly, [^{18}F]SFB was conjugated to precursor **1** (4-(4-fluoro-3-(piperazine-1-carbonyl)benzyl)phthalazin-1(2H)-one, AB478852, abcr) for 10 min at 120 °C. HPLC separation on a Luna C18(2) column (250 mm × 10 mm, 100 Å, 10 μm) and subsequent solid-phase extraction using a Sep-Pak Plus Light C18 cartridge yielded the product [^{18}F]PARPi.
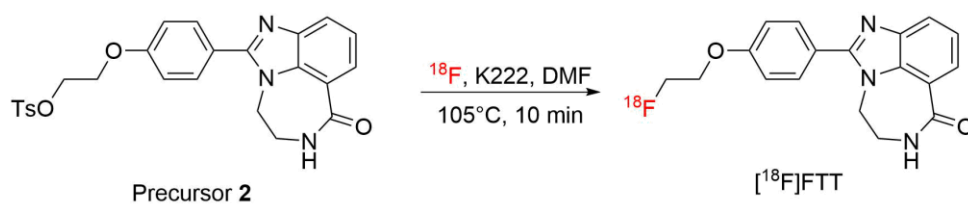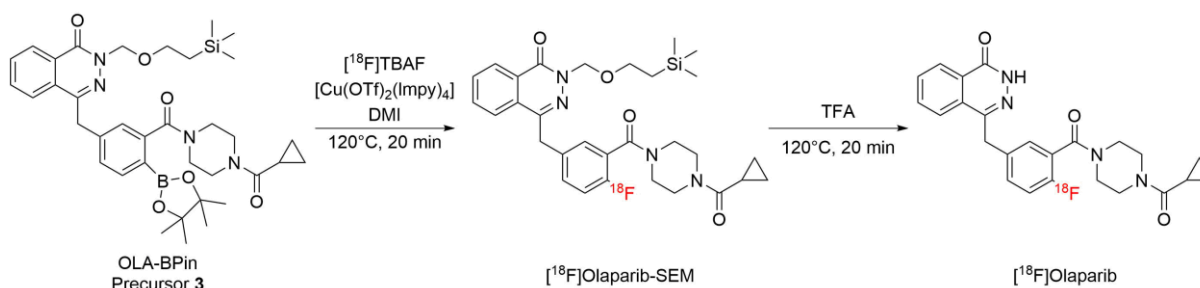
Figure 10: [18F]FTT radiosynthesis.

[18F]FTT was synthesized according to Stotz et al.[213] In short, [18F]fluoride was added to precursor **2** in 750 µL DMF and reacted for 10 min at 105 °C. After dilution with HPLC eluent, the reaction mixture was purified on a Luna C18(2) column (250 mm × 10 mm, 100 Å, 10 µm). The product peak was collected and [18F]FTT was reformulated using a Sep-Pak Plus Light C18 cartridge.
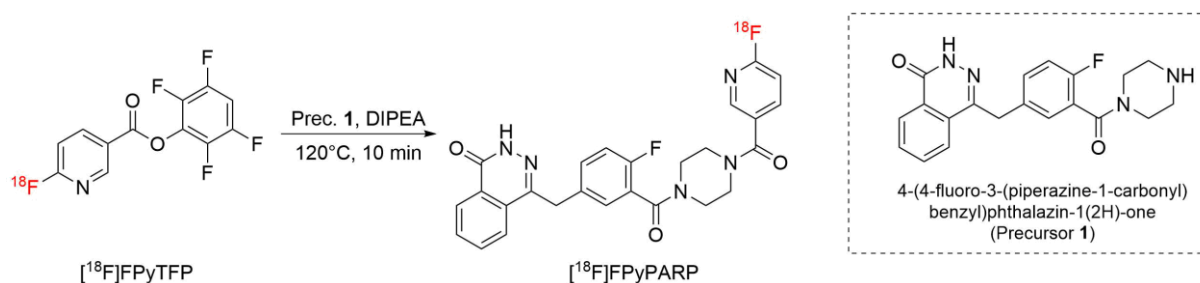

Figure 11: [18F]FPyPARP radiosynthesis.

[18F]FPyPARP was synthesized according to Stotz et al. in analogy to [18F]PARPi with the difference that the synthon [18F]FPyTFP was used instead of [18F]SFB.[213]

Figure 12: [18F]Olaparib radiosynthesis.

[18F]Olaparib was synthesized according to Bowden et al.[215] Briefly, precursor **3** was reacted with [18F]TBAF for 120°C for 20 min and subsequently deprotected with TFA at 120 °C for 15 minutes. The product was purified on a Luna C18(2) column (250 mm × 10 mm, 100 Å, 10 µm), collected, and reformulated using an HLB cartridge.
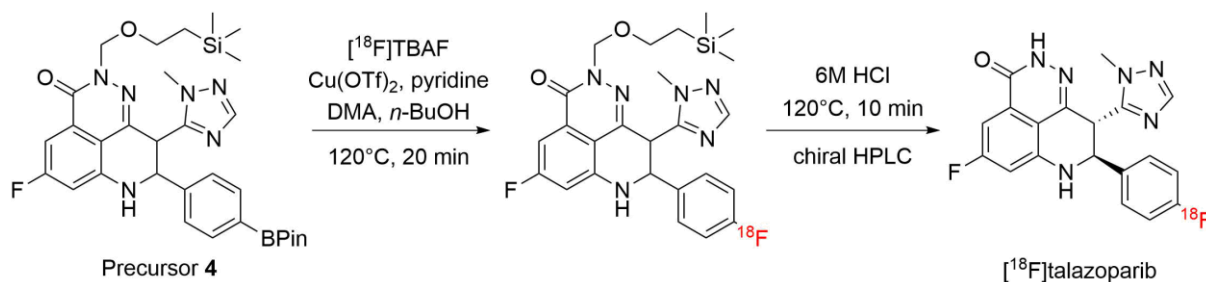
Figure 13: [¹⁸F]Talazoparib radiosynthesis.

[¹⁸F]Talazoparib was synthesized according to Bowden et al.[214] In short, [¹⁸F]TBAF was reacted with precursor **4** at 120 ℃ for 20 min and the intermediate was deprotected with 6 M HCl. The product was purified using a chiral 2D-HPLC strategy and reformulated using an HLB cartridge.

3.2.2 Radiosyntheses of Reporter Radiotracers
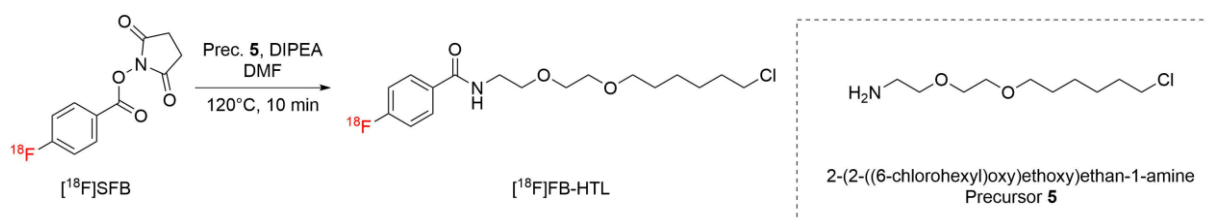

Figure 14: [¹⁸F]FB-HTL radiosynthesis.

[¹⁸F]FB-HTL was synthesized as follows: [¹⁸F]SFB was reacted with 10 mg precursor **5** in 500 μl DMF and 40 μL DIPEA for 10 min at 120°C. After cooling to 50°C, the reaction was diluted with 2 mL HPLC eluent (50 % MeCN in 0.1 % aqueous TFA) and purified on a Luna C18(2) column (250 mm × 10 mm, 100 Å, 10 μm). at a flow of 7 mL/min. The product peak (retention time 10 min, detected using an online radioactivity detector) was diluted in 50 mL H₂O and reformulated using a preconditioned Sep-Pak Plus Light C18 cartridge.
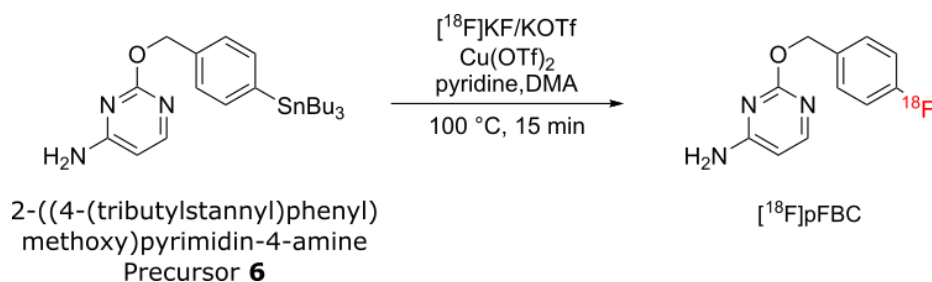
Figure 15: [¹⁸F]pFBC radiosynthesis.

[18F]*p*FBC was synthesized according to Bowden et al.[315] Precursor 6 was directly radiofluorinated using a copper-mediated radiofluorination (CMRF) reaction. The reaction mixture was purified on a Luna C18(2) column (250 mm × 10 mm, 100 Å, 10 µm) reformulated using a Sep-Pak Plus Light C18 cartridge.
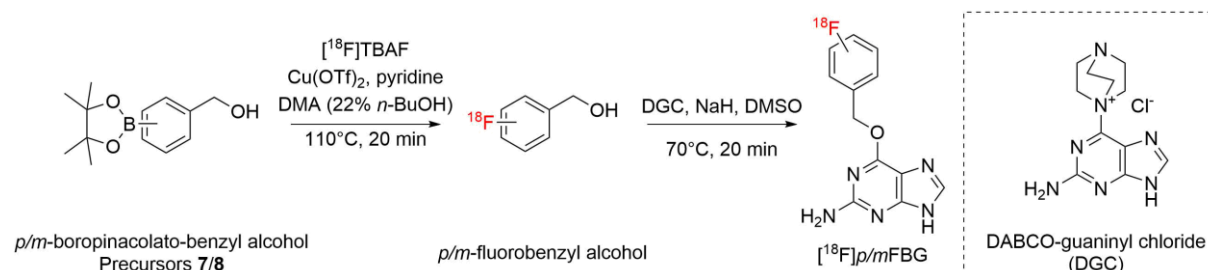
Figure 16: Radiosynthesis of [18F]*p*FBG and [18F]*m*FBG.

[18F]*p*FBG and [18F]*m*FBG were synthesized according to Stotz et al. via a fully automated two-step process.[316,306] In short, the respective *p/m*-boropinacolate precursors were radiofluorinated using [18F]TBAF and the resulting fluorobenzyl alcohols were conjugated to DABCO-guaninyl chloride (DGC). The reaction was diluted with HPLC eluent and subsequently purified with semipreparative HPLC (ABZ+; 5 µm; 250 × 10 mm). The product fraction was diluted with water and reformulated using an HLB cartridge.
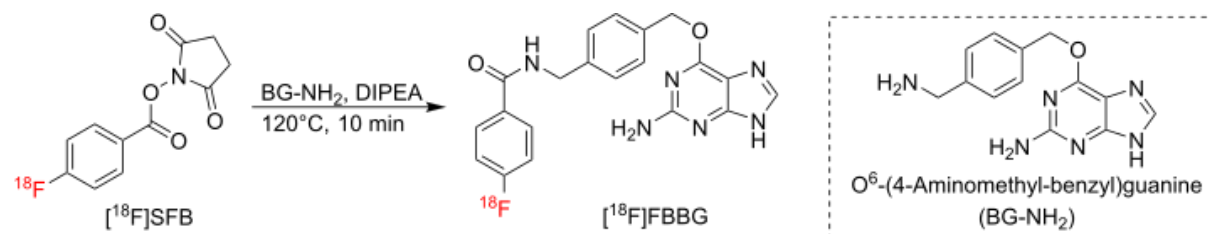
Figure 17: [18F]FBBG radiosynthesis.

[18F]FBBG was synthesized according to Stotz et al.[306] Briefly, the synthon [18F]SFB was added to the reactor containing BG-NH$_2$ (6-((4-(aminomethyl)benzyl)oxy)-7*H*-purin-2-amine, AA blocks) and heated to 120 °C for 10 min. HPLC eluent was added before semipreparative HPLC purification on a Luna C18(2) (5 µm, 100 Å, 250 × 10 mm). The final product was collected and reformulated using an Oasis HLB Plus Light cartridge.

3.3 In Vitro Methods

3.3.1 Cell lines, Plasmids and Viruses

Table 4: Cell lines used in this work

NAME	ORIGIN	SPECIES	SUPPLIER
HCC1937	breast ductal carcinoma	Human	DSMZ GmbH
Kras myc^{OE} p53$^{-/-}$	Pancreatic ductal adenocarcinoma	Murine	Zender Lab
Kras p53$^{-/-}$	Pancreatic ductal adenocarcinoma	Murine	Zender Lab
K1C1	Liver progenitor Kras	Murine	Zender Lab
K1C2	Liver progenitor Kras	Murine	Zender Lab
K5C1	Liver progenitor Kras	Murine	Zender Lab
K5C2	Liver progenitor Kras	Murine	Zender Lab
K3C2	Liver progenitor Kras myc^{OE}	Murine	Zender Lab
K3C4	Liver progenitor Kras myc^{OE}	Murine	Zender Lab
ACHN	Renal cell carcinoma	Human	Zender Lab
Hop62	Lung adenocarcinoma	Human	Zender Lab
CHP	Neuroblastoma	Human	DSMZ GmbH
CHP IDH	Neuroblastoma IDH^{OE}	Human	In-house
CHP mIDH	Neuroblastoma R132H mIDH^{OE}	Human	In-house
HCT116	Colon carcinoma	Human	DSMZ GmbH
HCT116 IDH	Colon carcinoma IDH^{OE}	Human	In-house
HCT116 mIDH	Colon carcinoma R132H mIDH^{OE}	Human	In-house
HEK293	Embryonic kidney	Human	Cell Line Service
HEK-Halo	Embryonic kidney HaloTag^{OE}	Human	In-house
HEK-SNAP	Embryonic kidney SNAPTag^{OE}	Human	In-house
HEK-CLIP	Embryonic kidney CLIPTag^{OE}	Human	In-house

3.3.2 Cell Line Generation Using Lipofection

The coding sequence for cell surface expression of HaloTag, SNAPTag and CLIPTag was constructed by in silico insertion of the sequences (Halo, SNAP26f or CLIP) downstream of the *Bgl*II site of the pDisplay (ThermoFisher Scientific) multiple cloning site sequence. The resulting open reading frame including the Kozak sequence was synthesized by BioCAT (Heidelberg, Germany) and inserted in between the *Xho*I and *Xba*I sites of pcDNA3.1(+) (Thermo Fisher Scientific). HEK293 cells were stably transfected with the pcDNA3.1 vector containing the respective reporter sequence using Lipofectamine 3000 transfection reagent

according to the manufacturer's protocol (ThermoFisher Scientific) and transgenic cells were selected with G418 (500 µg/mL, Biochrom, Berlin, Germany). Single clones were isolated using limiting dilution and tested for protein expression using Western blot.

3.3.3 Cell Line Generation Using Lentiviral Transfection

For the introduction of IDH and mIDH, we chose a lentiviral transfection strategy. Plasmids coding for IDH/mIDH under a tet-inducible promotor and third generation lentiviral packaging plasmids described by Lewis et al. were ordered from Addgene (Table 5).[317]

Table 5: Plasmids for lentiviral transfection

PLASMID	ADDGENE ORDER NO
pSLIK-IDH1- FLAG	#66802
pSLIK-IDH1-R132H-FLAG	#66803
pMDLg/pRRE	#12251
pRSV-Rev	#12253
pMD2.G	#12259

Once plasmid-bearing bacteria arrived, they were streaked on a LB agar plate with ampicillin, and single clones were picked for midi preparation according to the manufacturers protocol (QIAGEN Plasmid Plus Midi Ki, QIAGEN, Hilden, Germany). HEK293FT cells were seeded in 10 cm cell culture dishes for virus production and transfected the next day using Lipofectamine 3000 transfection reagent according to the manufacturer's protocol (ThermoFisher Scientific) and the lentiviral production workflow. Briefly, 1.5 mL Opti-MEM medium were mixed with either 42 µL Lipofectamine 3000 or with 2 µg of each packaging plasmid, 2 µg of the respective insert and 35 µL P3000 reagent. Subsequently, both formulations were mixed 1:1 and added to the HEK293FT cells. After overnight incubation, the medium was replaced with Opti-MEM supplemented with 10 % fetal calf serum (FCS), 100 U/mL penicillin, 100 µg/mL streptomycin, 1 % GlutaMAX and 1 % sodium pyruvate. The day after, the first batch of virus supernatant was collected, the medium replaced and the second day, a second batch of virus supernatant was collected. The supernatant was filtered through a 0.45 µm membrane and CHP and HCT116 cells were transfected with the supernatant in different concentrations in a 6-well plate (0 %, 2 %, 10 %, 20 %, 50 %, 100 % virus supernatant in complete medium). After a week in normal medium, single cell clones were selected with hygromycin (CHP: 100 µg/mL, HCT116: 200 µg/mL) and tested for IDH/mIDH expression.

3.3.4 Cell Culture

Cells were cultured in Roswell Park Memorial Institute (RPMI, PAN-Biotech, Aidenbach, Germany), McCoy's 5A medium (PAN-Biotech) or Dulbecco's Modified Eagle Medium (DMEM, PAN-Biotech) supplemented with 10 % FCS (Sigma-Aldrich, Steinheim, Germany), 100 U/mL penicillin and 100 μg/mL streptomycin (10,000 U/mL penicillin and 10 mg/mL streptomycin stock solution, PAN-Biotech) and additional supplements according to Table 6 which will be referred to as complete medium. For genetically modified cell lines, the same complete medium was used as for the parental cell line.

Table 6: Composition of complete medium for the cell lines used in this work

CELL LINE	MEDIUM	ADDITIONAL SUPPLEMENTS
HCC1937	RPMI	16 % v/v FCS
PDAC	DMEM	1 % v/v 100 mM sodium pyruvate (Sigma-Aldrich)
Liver Progenitor	DMEM	1 % v/v 100 mM sodium pyruvate 0.5 % v/v MEM non-essential amino acids (Sigma-Aldrich)
ACHN	DMEM	1 % v/v 100 mM sodium pyruvate 1 % v/v MEM non-essential amino acids
Hop62	DMEM	1 % v/v 100 mM sodium pyruvate 1 % v/v MEM non-essential amino acids
CHP	RPMI	-
HCT116	McCoy's 5A	-
HEK293	DMEM	-
HEK293FT	DMEM	1 % 1 M HEPES buffer (PAN-Biotech) 1 % 100x GlutaMAX (ThermoFisher Scientific)
HEK-reporter	DMEM	-

Cells were kept in T175 flasks (Greiner Bio-One, Frickenhausen, Germany) at 37°C under 5 % CO_2 atmosphere and passaged every 2-5 days when 90 % confluent. Absence of mycoplasma infection was confirmed by PCR analysis monthly.

For passaging, the medium was removed and the cells were washed with 5 mL PBS. After PBS removal, 3 mL 0.25% trypsin-EDTA solution (ThermoFisher Scientific) were added and the cells incubated for 5 min at 37°C until detachment. Trypsination was stopped by adding 7 mL complete medium, the cell solution was transferred to a 50 mL tube and centrifuged (500 × g, 5 min).

Cells were counted by resuspending the cell pellet in 10 mL PBS and preparing a 1:10 dilution of the cell suspension in 2 % aqueous trypan blue (ThermoFisher Scientific). 10 μL of

this dilution were then transferred to a Neubauer C-Chip counting chamber (NanoEnTek, Seoul, South Korea) and unstained cells were counted under a microscope.

3.3.5 Serum Stability and LogP/LogD Determination

Pooled serum from C57BL/6J mice or human serum (blood type AB+, Sigma-Aldrich) was used for determination of serum stability. Radiotracer solution was mixed 1:1 with serum and incubated at 37°C in a shaker. After 0, 30, 60, 120, and 240 min, samples were drawn and proteins were precipitated by addition of ice-cold MeCN to a final concentration of 50 %. After centrifugation (12,100 × g, 90 s), the supernatant was analyzed by HPLC with the same methods as described for the respective radiotracer's quality control.

For experimental logP and logD determination, water (logP) or PBS (logD) were mixed 1:1 with 1-octanol and saturated for 24 h. 1 µL of radiotracer solution was added to 1 mL of 1:1 water/PBS:1-octanol and the solution was mixed thoroughly. After short centrifugation for phase separation, triplicate samples were drawn from each phase and the radioactivity was measured in a gamma counter (WIZARD2, PerkinElmer, Waltham, MA, USA).

3.3.6 Fluorescence Microscopy

0.1×10^6 cells were seeded in a 4-chamber culture slide (BD Falcon, Franklin Lakes, NJ, USA) the day before the experiment to achieve 50% confluency. Cells were then incubated for 30 min at 37 °C with 250 µL of medium containing either 1 µM of a commercial fluorescent reporter-ligand (HaloTag AlexaFluor 488, Promega, Madison, WI, USA; SNAP-Surface AlexaFluor 488, or CLIP-Surface 488, NEB, Ipswich, MA, USA), or 1 µM of fluorescent ligand with 100 µM of the non-fluorescent compound as blocking control. DAPI solution (250 µL, 1:12,000 in PBS) was added for 5 min after removal of the staining solution. The cells were washed twice with 500 µL PBS, fixed with 500 µL 4% paraformaldehyde solution for 30 min and mounted with quick-hardening mounting medium (Eukitt, Sigma-Aldrich). Fluorescence microscopy was performed using a Zeiss LSM 710 ConfoCor3 microscope (Carl Zeiss, Jena, Germany) with a C-Apochromat × 40 N.A. 1.2 water immersion objective (Zeiss) and argon ion (488 nm) and DPSS (561 nm) excitation lasers.

3.3.7 Radiotracer Cell Uptake Experiments

Assay in Gamma Counter Tubes

A total of 1×10^6 cells in 0.9 mL medium were dispensed into gamma counter tubes (quadruplicates) and 0.6 mL tracer solution were added (2 MBq/mL in complete medium, either with 2.5 µL/mL DMSO as vehicle control or 2.5 µL/mL 10 mM non-radioactive standard (25 µM), blocking group). After incubation for 30 min at 37 °C, cells were washed twice with

0.5 mL and once with 1.5 mL complete medium. The supernatant was removed after a final centrifugation step and the samples were measured in a gamma counter (WIZARD2).

Assay in the Multi-Screen System

0.2×10^6 cells were incubated in 96-well filter plates (MADVN6550, Merck Millipore, Darmstadt, Germany) with 60 µL of a 0.4 MBq/mL radiotracer solution containing either 2.5 µL DMSO as vehicle or 2.5 µL/mL 10 mM non-radioactive standard to a final concentration of 25 µM as blocking control. After 30 min of incubation at 37°C, the cells were washed by vacuum filtration of medium through the plate (2×100 µL followed by 2×200 µL) and the filters were transferred into tubes using a commercial punch kit (MAMP09608, Merck) and measured in a gamma counter (WIZARD2).

3.3.8 SDS-PAGE Autoradiography

1×10^6 cells were incubated with 3 MBq of radiotracer in 250 µL complete medium for 15 min at 37°C (or medium only for control). After washing with 1 mL of complete medium, 200 µL RIPA buffer with protease inhibitor were added and the samples were incubated for 10 min at room temperature. 20 µL of sample were mixed with 4 µL 6x reducing loading buffer (tris-(2-carboxyethyl)-phosphine, TCEP), heated to 95°C for 5 min and subjected to discontinuous sodium dodecyl sulfate polyacrylamide gel electrophoresis (SDS-PAGE) on gels containing 12% polyacrylamide. After completion of the electrophoresis, a storage phosphor screen (Molecular Dynamics, Caesarea, Israel) was exposed to the gel in a light-shielded cassette for approximately 10 half-lives of ^{18}F (18 h), and the screen was scanned using a phosphor imager (Storm 840, Molecular Dynamics). The gel was stained with a commercial Coomassie solution (InstantBlue Protein Stain, Expedeon/Biozol, Eching, Germany) according to the manufacturer's instructions for loading control.

3.3.9 Commercial Assays (BCA and 2-HG)

A bicinchoninic acid assay (BCA assay) was performed to determine protein concentrations if applicable. For this, a BCA assay kit (Pierce BCA Protein Assay Kit, ThermoFisher Scientific) was used according to the manufacturer's instructions in a clear flat-bottom 96-well plate. Samples were analyzed in duplicates. Absorbance was measured at 550 nm with a SpectraFluor plate reader (Tecan, Maennedorf, Switzerland).

To determine 2-HG levels, a commercial D-2-HG kit was used according to the manufacturer's instructions with cell lysates of transfected cells (D2HG Assay Kit, Sigma-Aldrich). Duplicate samples were measured in a SpectraFluor plate reader with an excitation wavelength filter of 550 nm and an emission wavelength filter of 595 nm.

3.3.9 Western Blot

SDS-PAGE was performed as described above using samples containing 40 µg protein. After completion of the electrophoresis run, the proteins were transferred onto a poly-vinylidene fluoride membrane using the Mini-PROTEAN Tetra system (Bio-Rad, Hercules, CA, USA) and blocked for 1 h with Odyssey blocking buffer (Li-Cor, Lincoln, NE, USA). The blot was incubated at 4°C overnight in PBS with primary antibodies (Cell Signaling Technology, Danvers, MA, USA; Enzo Life Sciences, Farmingdale, NY, USA; ThermoFisher Scientific; Santa Cruz Biotechnology, Dallas, TX, USA; see Table 7). After washing twice with PBS-T for 10 min, the membrane was incubated for 1 h in PBS with secondary antibodies (see Table 8), washed again twice with PBS-T and subsequently imaged with an Odyssey Sa Infrared Imaging System (Li-Cor).

Table 7: Primary antibodies used for Western blot analysis in this work

TARGET	ORIGIN	SUPPLIER	CATALOGUE NO	RATIO
cmyc	mouse	ECACC(Mycl-9E10 hybridoma cells)	85102202	0.5 µg/mL
PARP	mouse	Enzo Life Sciences	BML-SA250-0050	1:1000
ATR	rabbit	Cell Signaling Technology	13934	1:1000
ATM	rabbit	Cell Signaling Technology	2873	1:1000/1:500
CHK1	mouse	Cell Signaling Technology	2360	1:1000
APOBEC3	rabbit	Cell Signaling Technology	41494	1:1000
Wee1	rabbit	Cell Signaling Technology	13084	1:1000
Phosphor-Wee1	rabbit	ThermoFisher Scientific	702120	1:1000
TNKS1/2	mouse	Santa Cruz Biotechnology	sc-365897	1:1000
β-actin	mouse	Merck	MAB1501	1:3333
β-actin	rabbit	Cell Signaling Technology	4970	1:3333

Table 8: Secondary antibodies used in this work

ANTIBODY TARGET	ORIGIN	SUPPLIER	CATALOGUE NO	RATIO
Mouse (IRDye 680RD)	donkey	LI-COR Biosciences	926-68072	1:12000
Rabbit (IRDye 800CW)	donkey	LI-COR Biosciences	926-32213	1:12000
Mouse (IRDye 800CW)	goat	LI-COR Biosciences	926-32210	1:12000
Rabbit (IRDye 680RD)	goat	LI-COR Biosciences	926-68071	1:12000
Mouse (IRDye 680RD)	goat	LI-COR Biosciences	926-68070	1:12000

3.4 In Vivo Methods

3.4.1 Animal Use and Care Licenses

All animal experiments were performed in accordance with to the European directives in the protection (Council Directive 2010/63/EU) and use of laboratory animals and the German Animal Welfare Act. The animal use and care protocols were approved by the responsible local authorities (Regierungspraesidium Tuebingen, R3/18 and R15/20 G).

3.4.2 Animal strains, Housing and Anesthesia

For the animal experiments, female NOD.CB17-*Prkdc^{scid}* mice were purchased from Charles River Laboratories (Sulzbach, Germany). Animals were housed at the Werner Siemens Imaging Center vivarium in individually ventilated cages (up to 5 mice per cage) with enrichment and water and a standard diet *ad libitum*. Animals were maintained on a 12 h:12 h light-dark cycle at a temperature of 22°C and 40-60 % humidity.

For the metabolite analysis, the subcutaneous (s.c.) tumor cell injections, PET scans and MRI, mice were anaesthetized with initial 5 % and maintained with 1.5 % isoflurane in pure medical oxygen with a flow rate of 1.5 L/min. For the intracranial virus injection, mice were anaesthetized with medetomidin/midazolam/fentanyl intraperitoneally (i.p., 0.5/5/0.05 mg/kg bodyweight) and antagonized with flumazenil/atipamezole s.c. (0.5/2.5 mg/kg bodyweight) after surgery. Mice received 5 mg/kg bodyweight carprofen during surgery and twice daily for 2 days after surgery.

3.4.3 Metabolite Analysis

Mice were injected with approximately 100 MBq of radiotracer intravenously (i.v.) via tail vein. After 5, 15 and 30 min, mice were sacrificed using CO_2 and blood was collected from the heart into EDTA-containing reaction tubes. The mice were immediately perfused with 20 mL cold PBS, the brain was explanted and homogenized with ice-cold PBS. Plasma (after centrifugation of the blood) and cleared brain homogenate were subjected to HPLC analysis.

3.4.4 Subcutaneous Xenograft Implantation

1×10^7 (HCC1937) or 5×10^6 (HEK293 and HEK-reporter) were injected subcutaneously (s.c.) in the right shoulder area (HCC1937) or the right flank (HEK293 and HEK-reporter) of mice (see 3.4.2 for strain information). After the xenografts reached a suitable size for imaging (100 – 500 mm^3), mice were subjected to further experiments.

3.4.5 Intracranial Virus Injections

Anaesthetized mice (see 3.4.2 for strain information) were placed on a stereotactic device with the head fixed and were warmed by a heating pad during surgery. The skin was incised and laterally displaced and the periost was removed with a scalpel until bregma and lambda were visible. From the bregma as reference point, a hole was drilled into the skull at coordinates anterior-posterior (AP) 0.6 mm and mediolateral (ML) -2 mm (right striatum) or + 2 mm (left striatum). Using a Hamilton syringe with a glass capillary (200 μm tip diameter, Hilgenberg GmbH, Malsfeld, Germany), 2 μL of either AAV-GFP or AAV-Halo were injected slowly into the right striatum (0.1 μL/30 s) at the coordinates AP 0.6 mm, dorsoventral (DV) - 3 mm and ML -2 mm. The capillary remained in place for 5 min to allow distribution of the injected solution and was then removed slowly (0.1 mm/ 10 s). On the left side (AP: 0.6 mm, DV: -3, ML: +2 mm) a sham injection with PBS was performed. After the injection, the skull was closed with bone wax and the skin was sewn.

3.4.6 *In Vivo* Imaging

PET imaging was perfomed on a dedicated small animal Inveon D-PET scanner (Siemens Preclinical Solutions, Knoxville, TN, USA) on self-regulating water-heated beds (Jomatik, Tuebingen, Germany or Medres, Cologne, Germany). PET data acquisition and scanner control was performed with Inveon Acquisition Workplace (Siemens Preclinical Solutions).
For 1 h dynamic scans (3600 s), the mice were placed on the scanner and 5 s after start of the emission scan protocol, the radioactive tracer was injected i.v. via a previously placed tail vein catheter. For 10 min static scans after 1 h resting uptake, the radiotracer was injected i.v. and the mice were kept under isoflurane for 1 h, after which they were placed on the scanners for the 10 min static emission scan protocol. After the respective emission scan

protocols, a transmission scan using a cobalt-57 source to account for attenuation and scattering artifacts was performed for 899 s.

Subsequently after the PET scans, animals were placed in a 7 Tesla BioSpec 70/30 USR or a ClinScan (Bruker Biospin MRI GmbH) MR tomograph equipped with a whole-body rat coil (diameter 72 mm, Bruker Biospin) for anatomical MRI scans. The choice of MR tomograph was dependent on equipment availability. MRI was performed using ParaVision 6.0.1 software (Bruker Biospin) and a modified T2-weighed 3-dimensional turbo spin-echo sequence (Biospec: TR = 800 ms, TE = 35; Clinscan: TR = 1800, TE = 90.5 ms).

3.5 Ex Vivo Methods

3.5.1 Ex Vivo Biodistribution Analysis

After the scans, mice were sacrificed by cervical dislocation (xenograft groups only) and organs of interest were collected. The organs were weighed in gamma-counter tubes and the radioactivity was measured by gamma-counting (WIZARD2) according to in-house protocols.

3.5.2 Brain Autoradiography

Immediately after the scans, mice were sacrificed using CO_2 and perfused with PBS. The brains were frozen in TissueTek OCT compound (Sakura Finetek, Torrance, CA, USA) and 20 µm slices of the striatal region were prepared on microscopy slides (R. Langenbrinck GmbH, Emmendingen, Germany). A storage phosphor screen (Molecular Dynamics) was exposed to the slides for 18 h and afterwards scanned at a resolution of 50 µm/pixel with a phosphor imager (STORM).

3.5.3 Immunofluorescence Microscopy

The immunofluorescence staining and microscopy was performed by the Department of Dermatology at the University of Tuebingen, Germany. Sections of paraffin-embedded xenografts were blocked with donkey serum for 30 min and incubated with primary antibody overnight (rabbit polyclonal anti-human PARP1 ab74290 (1:50, Abcam, Cambridge, UK), rat anti-CD31 (1:100, DIA-310, Dianova, Hamburg, Germany), mouse anti-c-myc (hybridoma supernatant 1:20, clone 9E10) and rabbit anti-Ki67 (1:100, ab15580, Abcam, Cambridge, UK)). After washing, the sections were incubated for 1 h at room temperature with secondary antibody (donkey anti-rat IgG Alexa488 (1:125, 712-546-153, Dianova), donkey anti-mouse IgG Cy3 (1:125, 715-166-151, Dianova), donkey anti-rabbit IgG (1:125, 711-606-152, Dianova), and Cy3 conjugated donkey anti-rabbit IgG (1:250, 711-166-152, Dianova)). Nuclei were stained with either DAPI solution (D9542, Sigma-Aldrich) or YO-PRO-1 iodide (ThermoFisher Scientific) for 25 or 5 min, respectively, according to the manufacturer's

instructions, the samples were subsequently mounted with Mowiol (Sigma-Aldrich) and imaged on an LSM 800 microscope (Carl Zeiss, Oberkochen, Germany).

3.5.4 Light Sheet Microscopy

If not indicated otherwise, the standard washing solution was PBS with 0.2 % Triton X-100 (PBS-TX100). Brains were stored in 15 mL tubes and transferred to either 15/30 mL screw cap vessels for alcohol de-/rehydration or 5 mL reaction tubes for antibody incubation and washing.

For light sheet microscopy, mice were injected with different vessel dyes (WGA 594 or WGA 680, 0.25 mg in 150 μL PBS i.v., Evans blue 2 % v/v 150 μL 12 h before perfusion i.p., see Table 9), and the animals were perfused first with 15 mL cold PBS with heparin (10 U/mL) and afterwards with 15 mL ice-cold 4 % PFA at 8 mL/min. Brains were removed, fixed with 4 % PFA overnight and stored in PBS with 0.05 % sodium azide until further use.

Table 9: Dyes used for preparation of the brains subjected to light sheet microscopy

DYE	TARGET	EMISSION WAVELENGTH	SUPPLIER
Evans blue	Large vessels	680 nm	Sigma-Aldrich
WGA594	Small vessels	618 nm	ThermoFisher
WGA680	Small vessels	704 nm	ThermoFisher

The brain tissue was permeabilized with penetration buffer (20 % DMSO, 0.3 M glycine in PBS-TX100) at 4°C overnight. Before antibody staining, an antigen retrieval and bleaching step was performed. Brains were incubated with an increasing methanol series at 4°C (30 %, 2 h; 50 %, 2 h; 70 %, 2 h; 95 %, 90 min; 100 %, 90 min) and bleached with bleaching solution (50 % MeOH, 33.3 % H_2O_2, 16.7 % DMSO) overnight. The brains were rehydrated the next day in reverse order (100 %, 30 min; 95 %, 30 min; 70 %, 2 h; 50 %, 2 h; 30 %, 2 h), washed with PBS-TX100 twice for 30 min at room temperature, and blocked with blocking buffer (10 % DMSO, 6 % FCS in PBS-TX100) overnight. Primary antibody was diluted in visicol antibody diluent (5 % DMSO, 3 % FCS, 0.05 % sodium azide in PBS-TX100), added to the brains and incubated for 12 days at 37°C (Table 10). After the incubation, brains were washed several times over a course of 1.5 days with PBS-TX100. Secondary antibody was again diluted in visicol antibody diluent, a nuclear stain was added (SYTOX Orange, ThermoFisher Scientific, 1:3000) and brains were incubated at 37°C for 12 days (Table 11). After the second washing step for 1.5 days with PBS-TX100, brains were dehydrated again with an increasing EtOH series (30 %, 50 %, 70 %, 100 %, 100 %, change of solutions every 24 h). Refractive indices were matched with ethyl cinnamate (ECI) and brains were images on an UltraMicroscope Blaze (Milteny Biotec, Bergisch Gladbach, Germany).

Table 10: Primary antibodies used for light sheet microscopy in this work

TARGET	ORIGIN	SUPPLIER	CATALOGUE NO	DILUTION
c-myc	mouse	ECACC (Mycl-9E10 hybridoma cells)	85102202	2 µg/mL
SNAP/CLIPTag	rat	Chromotek	6f9	1 µg/mL
HaloTag	rabbit	Promega	G9281	1 µg/mL

Table 11: Secondary antibodies used for light sheet microscopy in this work

TYPE/CONJUGATE	ORIGIN	SUPPLIER	CATALOGUE NO	DILUTION
Mouse (H+L) Cross-Adsorbed, AlexaFluor Plus 555	donkey	Invitrogen	A32773	1:300
Rat IgG (H+L) Cross-Adsorbed, DyLight 755	donkey	ThermoFisher Scientific	SA5-10031	1:200
Rabbit IgG (H+L) Cross-Adsorbed, AlexaFluor 750	goat	ThermoFisher Scientific	A-21039	1:200

3.6 Data Analysis

3.6.1 Statistical Analysis

Statistical analyses are represented as mean values ± standard deviation (SD). Analyses were performed using GraphPad Prism 9 and non-parametric t-tests (comparison of two groups) and one-way analysis of variance (ANOVA, comparison of more than two groups). Blood half-life was calculated using a two-phase decay fit in GraphPad Prism 8. P-values < 0.05 were considered statistically significant according to the software (*: $p < 0.05$, **: $p < 0.01$, ***: $p < 0.001$, ****: $p < 0.0001$).

3.6.2 PET Image Analysis

PET image reconstruction and co-registration with MR images for the xenograft models was performed with Inveon Acquisition Workplace and Inveon Research Workplace (Siemens Preclinical Solutions), respectively, using the acquired attenuation scan, user-defined dynamic framing (12 × 5 s, 6 × 10 s, 6 × 30 s, 5 × 60 s, 10 × 300 s) and an ordered-subset expectation maximization 3D (OSEM3D) algorithm. Regions of interest (ROIs) were drawn according to the acquired MR images and co-registered with the PET data to obtain time-activity curves (TACs). TACs are displayed as the standardized uptake value (SUV) as calculated in Microsoft Excel.

3.6.3 Pmod

For the brain studies, PET images were co-registered with the Mirrione mouse brain atlas[318] in pmod (version 4.2). For kinetic analyses, the Logan reference tissue model was used.[319] For volume of interest (VOI) analyses, either whole-striatum VOIs were used (according to the brain atlas) or a 70 % isocontour VOI.

4. RESULTS AND DISCUSSION

4.1 Side-by-Side Comparison of PARP Radiotracers

We successfully adapted the syntheses of [^{18}F]PARPi[209,320], [^{18}F]FTT[212] and [^{18}F]olaparib[215,216] from the literature in our laboratories and, in addition, designed and synthesized [^{18}F]FPyPARP[213] and [^{18}F]talazoparib[214] (contributions according to Chapter 8.1). First, we developed the less lipophilic [^{18}F]PARPi variant [^{18}F]FPyPARP (clogP: 2.49). For further comparison, we synthesized the benchmark PARP radiotracers [^{18}F]PARPi and [^{18}F]FTT (clogP: 3.36 vs 3.09, respectively). [^{18}F]PARPi syntheses was adapted from literature.[209] *N*-succinimidyl 4-[^{18}F]fluorobenzoate ([^{18}F]SFB) was used instead of the free fluorobenzoic acid as a reaction intermediate for automation of the radiosynthesis. [^{18}F]FPyPARP was synthesized using [^{18}F]FPyTFP as a synthon.[213] [^{18}F]FTT was afforded by a one-pot synthesis through direct radiofluorination of the tosylate precursor.[321] All radiotracer syntheses resulted in good RCY, RCP and MA and a reasonable synthesis time for further *in vitro* and *in vivo* application (Table 12).

To verify the decreased lipophilicity, logP and logD values were determined using the shake-flask method. As expected, [^{18}F]FPyPARP exhibited a lower logP and logD compared to [^{18}F]PARPi (1.16 vs. 2.09, respectively, identical for logP and logD). Interestingly, the logP of [^{18}F]FTT was closer to [^{18}F]FPyPARP (1.10) while the logD was in the same range as [^{18}F]PARPi (1.94). Thereby, we were able to confirm that the exchange of the prosthetic group from a fluorobenzoic to a fluoronicotinic acid decreased the logP and logD value of [^{18}F]FPyPARP in comparison to [^{18}F]PARPi.

In parallel, we set out to directly compare the radiolabeled first generation PARP inhibitor olaparib with the latest and most potent PARP inhibitor talazoparib. The synthesis of [^{18}F]olaparib was disclosed during the course of this work and promptly adapted to our laboratories.[217] Talazoparib is a chiral molecule, and only the (8S, 9R)-diastereomer is a PARP inhibitor while the enantiomer LT-674 (8R, 9S) is several magnitudes less active.[322] Instead of using an enantiomerically pure precursor, both [^{18}F]talazoparib and [^{18}F]LT-674 were synthesized simultaneously and subsequently separated by chiral HPLC, to avoid potential racemization of an enantiomerically pure precursor during the harsh reaction conditions.

A design of experiments (DoE) study was applied by Dr. Gregory D. Bowden to the syntheses of [^{18}F]olaparib and [^{18}F]talazoparib to optimize the yield for *in vitro* and *in vivo* studies. This drastically improved the yields of both radiotracers, which is of particular importance for [^{18}F]talazoparib. Due to radiolabeling of the racemate and the subsequent enantiomeric separation, the yield is cut in half from the beginning. Thus, the radiosynthesis

must be fully optimized to afford a sufficient amount of enantiomerically pure [^{18}F]talazoparib for further studies.

Table 12: Radiochemical characterization of the reporter radiotracers. n = 18 for [^{18}F]PARPi[1], n = 5 for [^{18}F]FTT, n = 10 for [^{18}F]FPyPARP, n = 2 for [^{18}F]olaparib, and n = 4 for [^{18}F]talazoparib.

	% RCY	RCP	MA (GBq/µmol)	SYNTHESIS TIME (min)
[^{18}F]PARPi	7 ± 3	> 95 %	31 – 265	94
[^{18}F]FTT	9 ± 4	> 95 %	71 – 329	50
[^{18}F]FPyPARP	12 ± 10	> 95 %	16 – 109	72
[^{18}F]olaparib	71 ± 9	> 95 %	25 – 58	108
[^{18}F]talazoparib	13 ± 3	> 95 %	52 – 176	120

In advance of the *in vitro* and *in vivo* evaluation, the two novel PARP radiotracers [^{18}F]FPyPARP and [^{18}F]talazoparib were tested for their stability in human and mouse serum (Figure 18). Over a time course of 240 minutes no radiometabolite was detected by HPLC analysis.

---

[1] One synthesis was excluded due to a defective radioactivity detector leading to incomplete data
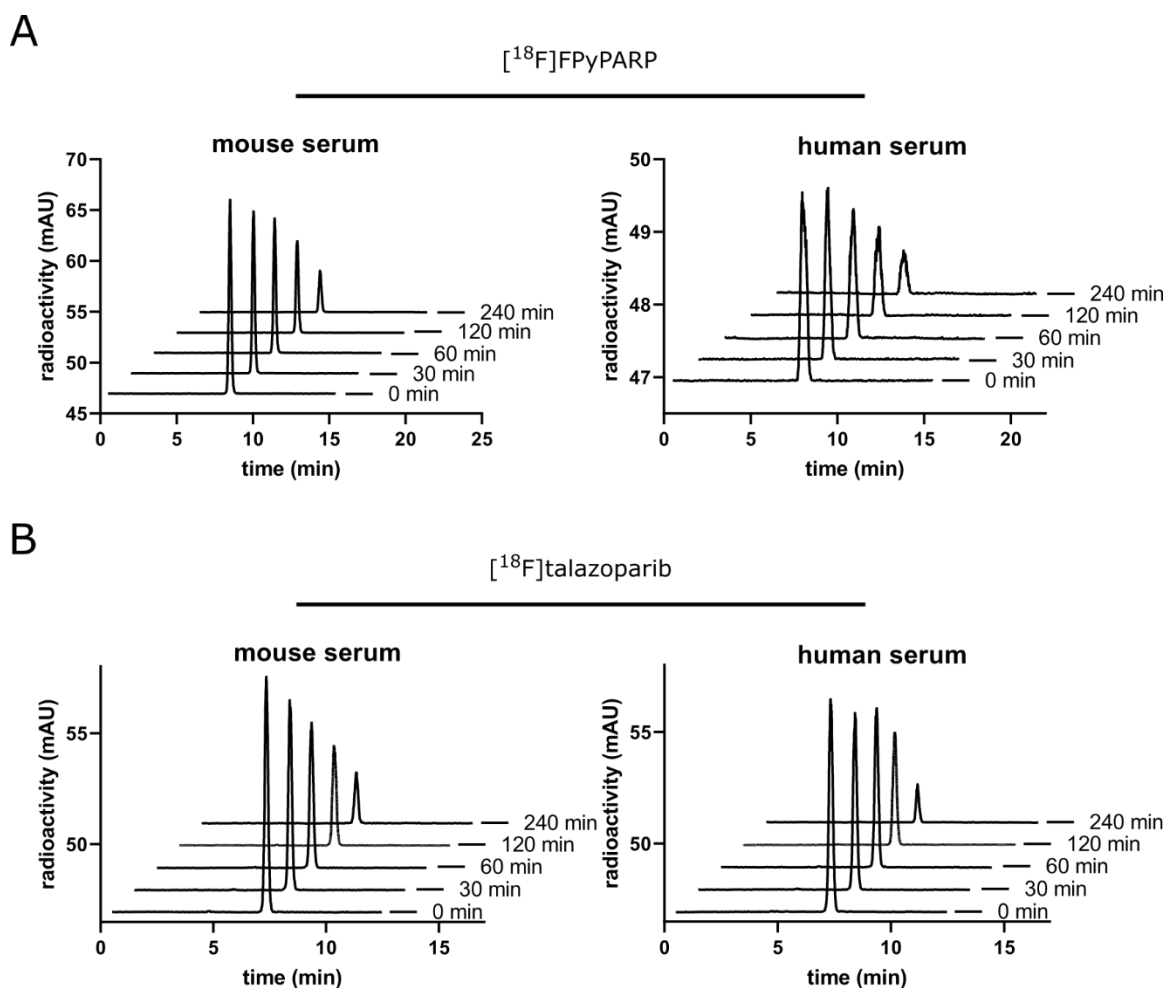
Figure 18: HPLC chromatograms from serum stability analyses in mouse and human serum. A Serum stability of [^{18}F]FPyPARP. **B** Serum stability of [^{18}F]talazoparib.

For *in vitro* evaluation of all five radiotracers, HCC1937, a BRCA-mutated primary ductal carcinoma cell line, was used. The same model was already utilized for evaluation on [^{18}F]FTT.[219] Strong expression of PARP1 in HCC1937 cells was confirmed by Western blot analysis (Figure 19 C), showing a band at the corresponding molecular weight of PARP1 (116 kDa).

To confirm PARP binding of the radiotracers, HCC1937 cells were incubated with each radiotracer separately, washed, and the residual radioactivity was measured by gamma-counting. To verify PARP-specific binding, cells were additionally co-incubated with excess of Olaparib (25 µM). Later on, sustained PARP1 expression in HCC1937 xenografts was also verified by immunofluorescence (IF) staining after the *in vivo* experiments (Figure 19 B).

All radiotracers showed high uptake in HCC1937 cells (Figure 19 A). Although absolute uptake was highest for [^{18}F]FPyPARP compared to control wells without cells, the fold-change revealed that [^{18}F]talazoparib bound most (61.9-fold), followed by [^{18}F]PARPi and [^{18}F]olaparib (28.7-fold), [^{18}F]FTT (13.9-fold) and [^{18}F]FPyPARP (7.2-fold). The PARP radiotracer uptake was significantly increased for all five in comparison to control wells

without cells. Also, uptake was blockable to baseline levels with olaparib, demonstrating PARP1 specific binding.
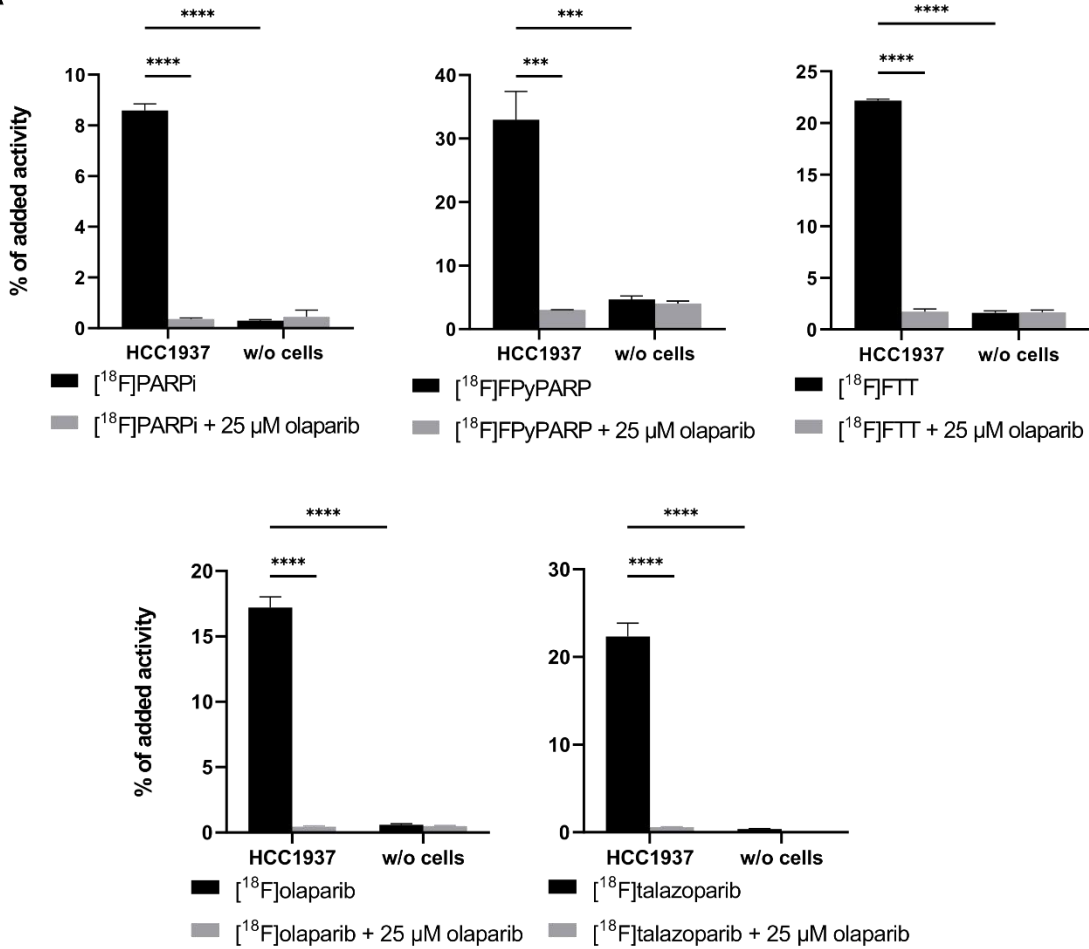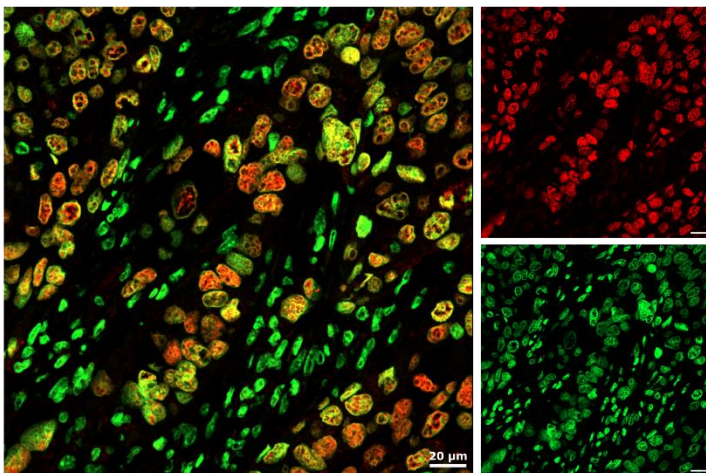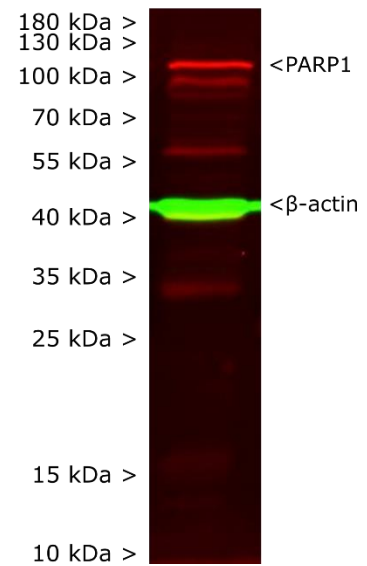
Figure 19: Evaluation of the cell model and the xenografts. A Uptake of the five radiotracers in HCC1937 cells *in vitro*, blocked with olaparib. Error bars represent the standard deviation of n = 3 biological replicates. **B** Immunofluorescence images from HCC1937 xenograft tissue (PARP in red, nuclei in green). **C** Western blot of HCC1937 cell lysate with anti-PARP1 antibody.

After confirming sufficient PARP-1 expression and *in vitro* PARP radiotracer uptake in the chosen cell model, HCC1937 cells were injected subcutaneously in the shoulder region of immunodeficient female NOD.CB17-*Prkdc^{scid}* mice (n = 5 per group) for an *in vivo* xenograft study. The shoulder was chosen here instead of the more common flank injection to avoid spill-over effects from the excreting organs. After sufficient tumor growth, mice underwent dynamic PET imaging for 1 hour directly after radiotracer injection, and a second PET scan 2 hours after injection to ensure progressed excretion. PET images were correlated with anatomical MRI scans for image analysis and ROI quantification.

Generally, the PET images revealed high abdominal uptake for all five radiotracers (Figure 20). This was expected due to clearance routes, which usually cause high initial uptake in excreting organs like kidney, liver and bladder. At the later time point, the abdominal radioactivity decreased and single organs became more visible, indicating that a stable *in vivo* radiotracer biodistribution was reached.

Like the bladder is a reliable measure for renal excretion, the hepatobiliary excretion can be quantified in the intestine. Since the intestine itself is very difficult to quantify, the liver was chosen as a surrogate for hepatobiliary excretion quantification in this work, although some signal might come from specific binding. When comparing our novel PARP tracer [^{18}F]FPyPARP with the gold standards [^{18}F]PARPi and [^{18}F]FTT, only [^{18}F]FPyPARP showed consistent bladder uptake, pointing towards increased renal clearance (Figure 21). Liver uptake was initially high for all three radiotracers, but decreased over time. Pronounced kidney uptake, in particular in the medullar region at the later timepoint, can also be seen in the PET images (Figure 20 A-C). Although the introduction of a nitrogen seems to increase renal clearance of [^{18}F]FPyPARP in comparison to [^{18}F]PARPi, both radiotracers are still excreted by both hepatobiliary and renal pathways.

The direct comparison of the PET images of [^{18}F]olaparib with [^{18}F]talazoparib revealed a clearly higher bladder uptake for [^{18}F]olaparib in contrast to [^{18}F]talazoparib. Liver uptake of both radiotracers was relatively high initially, and persisted over time. The same applies to the kidney uptake. This indicates that both [^{18}F]olaparib and [^{18}F]talazoparib are cleared by mixed hepatobiliary and renal excretion.

Taking a closer look at the HCC1937 tumors, PARP radiotracer distribution was heterogenous within the xenografts, in particular for [^{18}F]FTT and [^{18}F]talazoparib. This observation is in line with literature-known heterogenous PARP1 expression in tumors.[323] For [^{18}F]FTT, [^{18}F]olaparib and [^{18}F]talazoparib, the xenograft was more clearly distinguishable from surrounding tissue than for [^{18}F]PARPi and [^{18}F]FPyPARP for both time points. According to the PET images, [^{18}F]FTT seems to have the highest xenograft uptake, but it

also has higher background compared to for example [18F]FPyPARP. A more quantitative approach is the direct measurement of organ radioactivity.
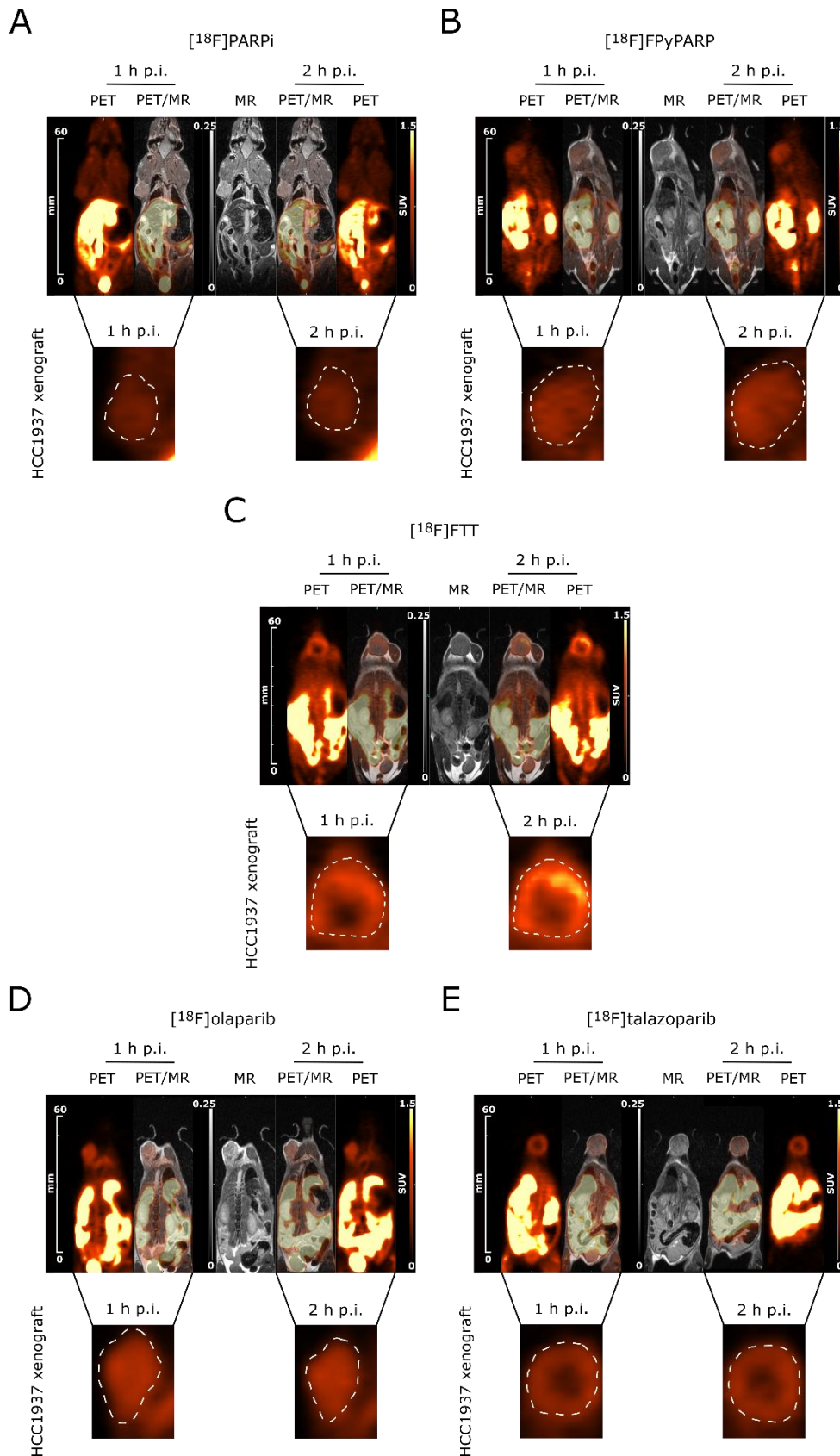
Figure 20: Representative PET and MR images of the 5 evaluated PARP radiotracers with focus on the xenografts, A [18F]PARPi, **B** [18F]FPyPARP, **C** [18F]FTT, **D** [18F]olaparib, and **E** [18F]talazoparib. 1 h images are

the last 10 min of a 1 h dynamic PET scan and after 2 h, a 10 min static PET scan was performed. HCC1937 xenograft images are displayed below the respective whole-body images.
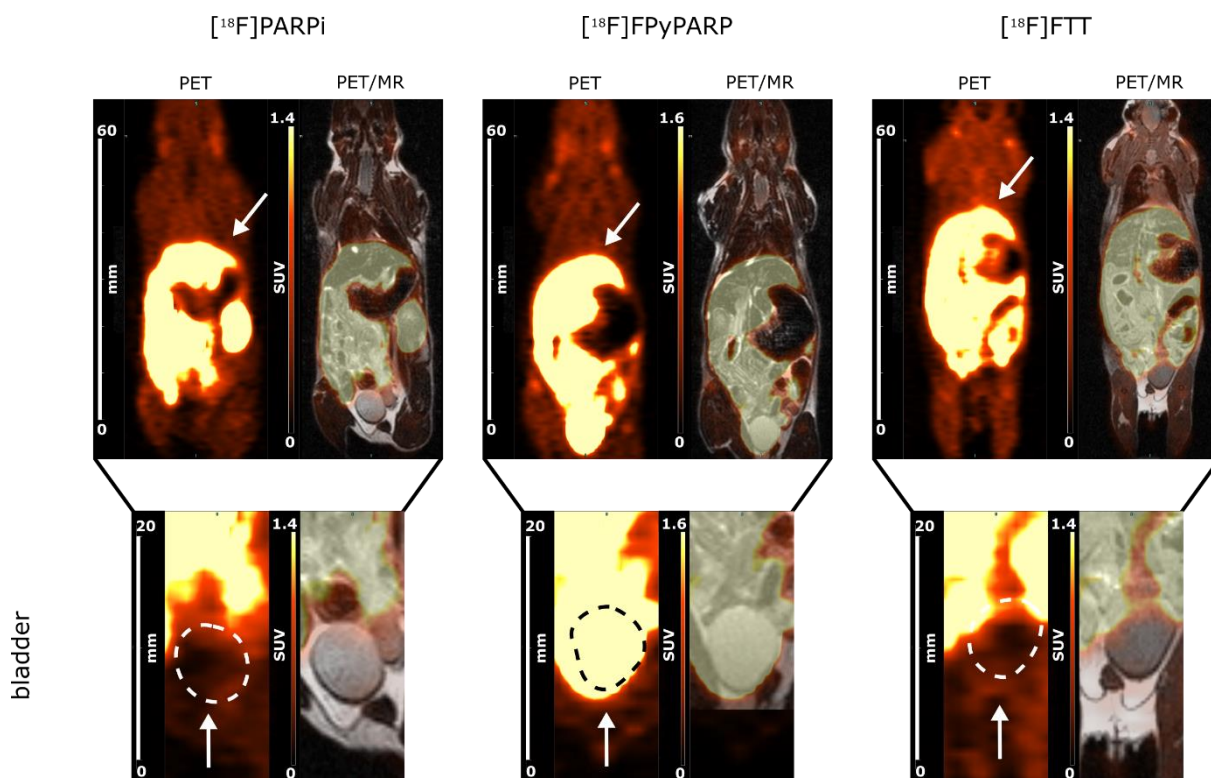
Figure 21: Representative PET and MR images of the last 10 min of a 1 h dynamic PET scan. Images show [^{18}F]PARPi, [^{18}F]FPyPARP and [^{18}F]FTT-injected animals, comparing the excreting organs liver and bladder (indicated with white arrows), with focus on the bladder displayed enlarged below.

Subsequently after the second static PET scan 2 hours p.i., the mice were sacrificed and organs were collected to measure the residual radioactivity by gamma-counting. Here, all five radiotracers had a similar pattern with the highest uptake in kidney, intestine, liver and spleen (Figure 22 A), in line with the PET images (Figure 22 A).

[^{18}F]FPyPARP featured liver and kidney uptake comparable to [^{18}F]FTT, and [^{18}F]PARPi showed liver uptake in the same range but lower kidney values. To further evaluate and quantify the excretion routes, the liver-to-kidney ratios (LKRs) were calculated and showed balanced renal and hepatobiliary clearance for [^{18}F]PARPi and [^{18}F]FTT (Figure 22 D). As expected, the excretion route of [^{18}F]FPyPARP was shifted towards renal clearance compared to [^{18}F]PARPi (0.6 vs 1.4, respectively). This confirms our hypothesis that [^{18}F]FPyPARP is an alternative to [^{18}F]PARPi and clearance route is shifted towards more renal clearance relative to hepatobiliary clearance, which was mainly hepatobiliary for [^{18}F]PARPi in murine glioblastoma models.[209] In clinical studies, [^{18}F]PARPi presented with already 30 % renal clearance, suggesting that with [^{18}F]FPyPARP, imaging of liver metastasis could be feasible.[208]

RESULTS AND DISCUSSION

[^{18}F]Olaparib and [^{18}F]talazoparib revealed similar liver uptake but [^{18}F]talazoparib had a higher kidney uptake in comparison. The LKRs of 1.8 ([^{18}F]olaparib) and 1.1 ([^{18}F]talazoparib) confirmed balanced renal and hepatobiliary clearance while [^{18}F]olaparib was cleared mainly hepatobiliarily.

As replicative stress can also occur in the brain, for example in brain tumors, brain penetration was assessed. Only for [^{18}F]FTT apparent brain uptake was observed, while [^{18}F]PARPi and [^{18}F]FPyPARP show more residual activity in the brain, and no brain uptake was detected for [^{18}F]talazoparib and [^{18}F]olaparib.

The most important question here, besides the differences in excretion routes, is the target engagement of the radiotracers in the case of a PARP-expressing tumor. To evaluate the performance of the radiotracers in the xenografts, the biodistribution data were analyzed and absolute tumor uptake was considered as well as the ratio of tumor uptake to the reference tissues muscle and blood.

Absolute tumor uptake was highest for [^{18}F]FTT (4.7 %ID/g), followed by [^{18}F]olaparib (3.7 %ID/g) (Figure 22 A). [^{18}F]FPyPARP and [^{18}F]olaparib were within the same range (2.0 and 2.5 %ID/g), and [^{18}F]PARPi showed lowest tumor uptake (1.1 %ID/g). However, absolute tumor uptake is not necessarily a good measure of tumor targeting performance, as the signal-to-noise ratio is most important to clearly distinguish a tumor from the surrounding tissue. Thus, tumor uptake needs to be considered in relation to a reference tissue with negligible background uptake of the radiotracer.

The tumor-to-muscle ratios (TMRs) were indeed comparable between the five radiotracers (Figure 22 B). Although [^{18}F]PARPi performed worst in terms of absolute uptake, the TMR is second-highest, with [^{18}F]FTT featuring the highest TMR (2.9 and 3.3, respectively). The TMRs of [^{18}F]FPyPARP and [^{18}F]olaparib are comparable (2.5 and 2.3), and [^{18}F]talazoparib was the lowest (1.8). Nevertheless, these values in a greater context are within the same approximate range, and demonstrate that all five radiotracers are able to reliably distinguish PARP-expressing tumors from surrounding muscle tissue.

As a second reference tissue the blood was chosen, since blood retention and thus longer circulation of the radiotracers in the blood pool can lead to higher tissue and tumor accumulation. The tumor-to-blood ratios (TBRs) reveal higher values for [^{18}F]talazoparib and [^{18}F]olaparib (Figure 22 C). This is expected, as the absolute blood uptake values were the lowest for those two radiotracers, while [^{18}F]FTT had the overall highest blood signal, which is reflected by a relatively low TBR. Still, the TBRs are in a good range and do not hamper the use of the radiotracers in heavily perfused organs.

A potential pitfall when looking at PARP radiotracer uptake is the lack of a 'true' reference tissue, since PARP is more or less expressed in all tissues. Thus, we evaluated two different

reference tissues to account for background PARP expression and to primarily focus on the signal-to-noise ratio.
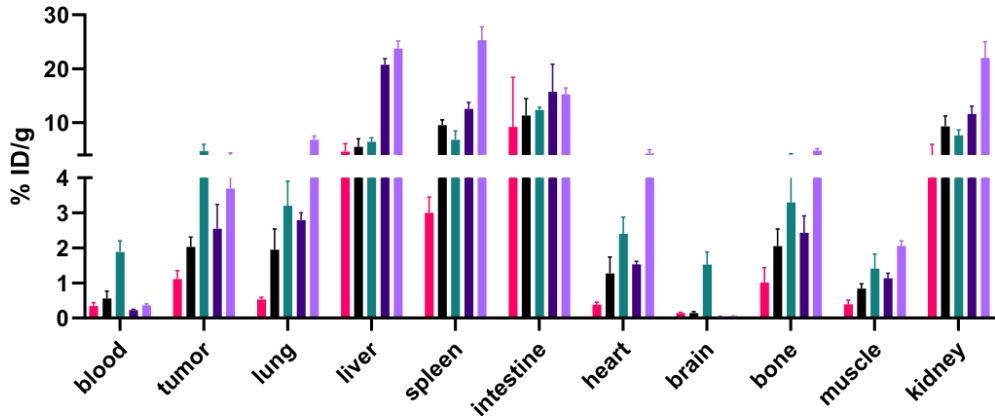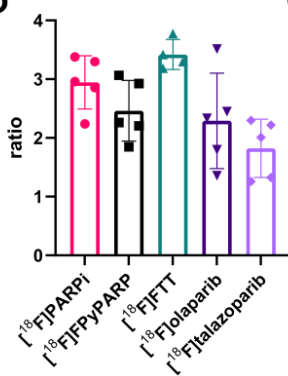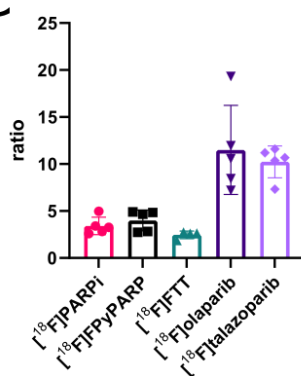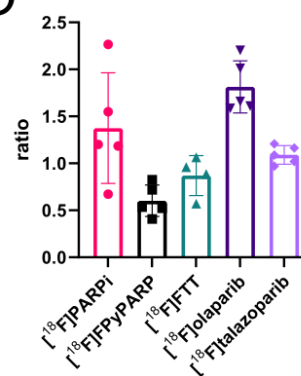
Figure 22: *Ex vivo* **biodistribution analysis of the five PARP radiotracers. A** Biodistribution in selected organs 3 h p.i. **B** Tumor-to-muscle, **C** tumor-to-blood, and **D** liver-to-kidney ratios for the radiotracers. Error bars represent standard deviations of n = 5 mice (n = 4 for [^{18}F]FTT).

To have dynamic insights into the radiotracer biodistribution within the first hour after radiotracer administration, the TACs from the dynamic PET scan were analyzed. As the TACs do only represent the first hour after tracer administration, these findings are not contradictory to the *ex vivo* biodistribution which was performed 3 h p.i..

For the xenografts, the TACs reflect the *ex vivo* biodistribution data very well, with [^{18}F]FTT and [^{18}F]talazoparib having the highest uptake 1 hour p.i. and [^{18}F]olaparib, [^{18}F]FPyPARP and [^{18}F]PARPi being in the same range. While the latter three seem to have reached an stable maximum already at the 1 hour time point, [^{18}F]talazoparib and [^{18}F]FTT were still in a positive slope. This could be explained by the longer blood circulation of [^{18}F]FTT.

The blood biodistribution data gives information on how long the radiotracer is circulating in the blood, and, if there is no target present in the blood, indirectly on excretion kinetics. Blood retention was highest for [^{18}F]FTT in the *ex vivo* biodistribution, while the other four radiotracers were comparably low. The heart TACs were used to calculate the blood half-life

which was comparably fast ([^{18}F]PARPi: 3.7 min; [^{18}F]FPyPARP: 1.2 min; [^{18}F]FTT: 2.2 min; [^{18}F]olaparib: 2.1 min; [^{18}F]talazoparib: 3.3 min).

The liver TACs showed highest liver uptake for [^{18}F]olaparib and [^{18}F]talazoparib while the other three were comparable. This is in line with the *ex vivo* biodistribution data. Notably, [^{18}F]FPyPARP featured a lower initial liver uptake in comparison to [^{18}F]PARPi, underlining the reduced hepatobiliary clearance.

In the kidneys, the uptake between the five radiotracers differed more in the kidney cortex compared to the medulla, where no actual difference was visible, but was generally in the same range. As the whole kidney was used for *ex vivo* biodistribution analysis, the absolute values reflect more on the difference in the kidney cortex, with [^{18}F]talazoparib as highest and [^{18}F]PARPi as lowest value.

Generally, the differences in the maximum values and the slopes of the TACs could be attributed to the actual excretion dynamics of the radiotracers, while the differences after reaching equilibrium probably corresponds to the PARP expression of the tissue.

We were able to successfully shift the excretion route from mainly hepatobiliary to more renal with the [^{18}F]PARPi alternative [^{18}F]FPyPARP. This demonstrates the potential of small chemical changes to improve pharmacokinetic properties. Other than that, [^{18}F]PARPi, [^{18}F]FPyPARP, and [^{18}F]FTT featured similar uptake patterns, however, [^{18}F]PARPi generally had lower background uptake in lung, heart, bone, and muscle.

In the direct comparison of the first generation PARP inhibitor [^{18}F]olaparib to the currently most potent [^{18}F]talazoparib, we found that they behaved relatively similar, except for a notably higher uptake of [^{18}F]talazoparib in lung, spleen, heart and bone. [^{18}F]Talazoparib exhibited highest heart and bone uptake among all five PARP radiotracers. The improved PARP trapping capacity of talazoparib does not seem to have much influence on [^{18}F]talazoparib pharmacokinetics and its ability to delineate xenografts from healthy tissue. However, a study performed in a different xenograft model at later time points (4 and 8 hours) reported that the tumor retention is improved in comparison to olaparib-derived radiotracers.[220]

Concluding, radiotracer distribution can vary significantly between the different PARP radiotracers, especially in organs not related to excretion. In consequence, the choice of the most suitable PARP radiotracer is dependent on the organs of interest. If the organ of interest is the lung, for example in cases of lung cancer or metastases, [^{18}F]PARPi would be a better choice than [^{18}F]talazoparib due to lower background in the lung. With these five PARP radiotracers in hand, we were optimally equipped to tackle the question whether quantification of PARP can be correlated with levels of replicative stress.
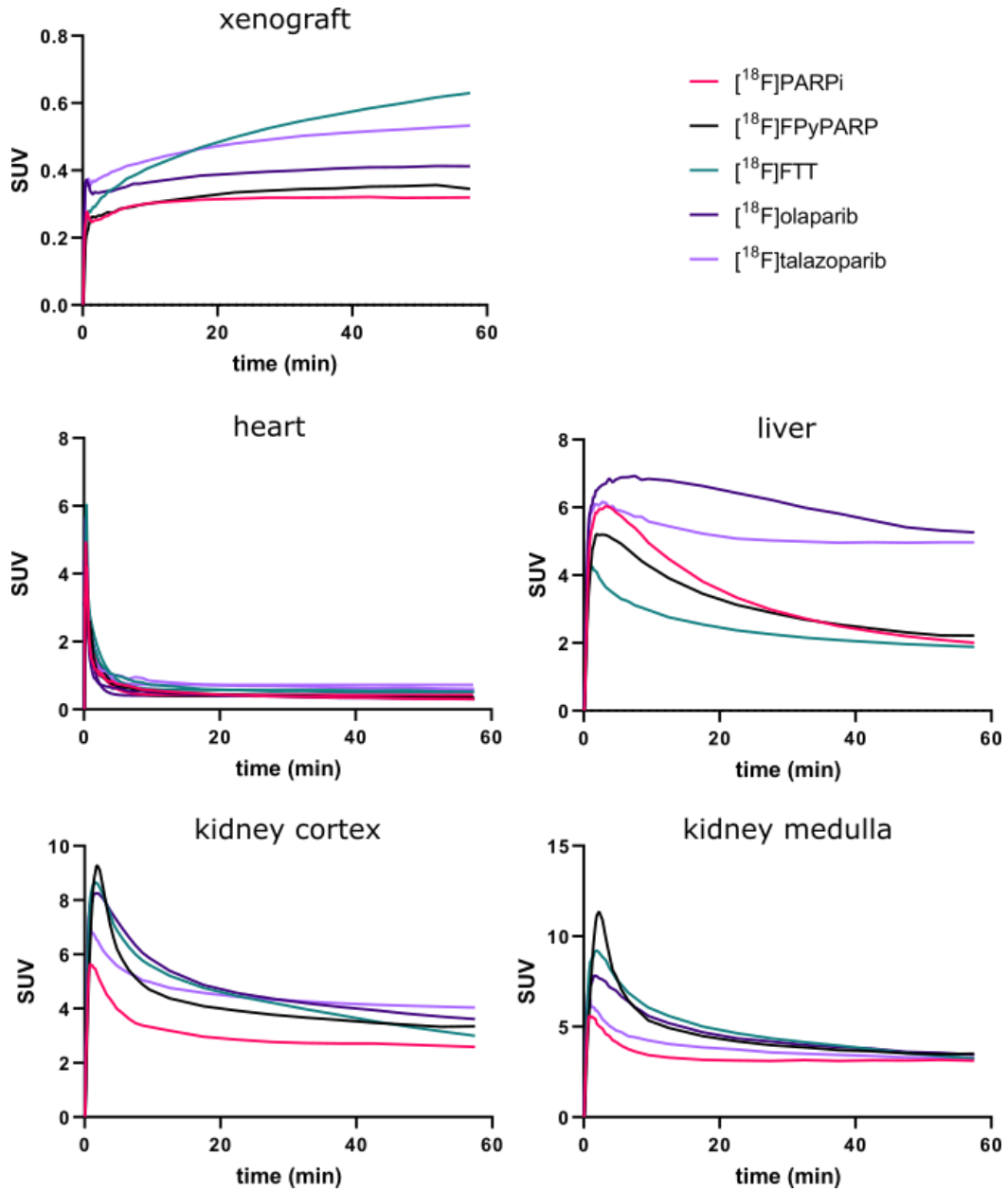
Figure 23: TACs of the five radiotracers in selected organs. TACs for the xenografts (n = 6 for [18F]PARPi and [18F]FTT, n = 7 for [18F]FPyPARP, n = 4 for [18F]olaparib, n = 5 for [18F]talazoparib), heart, liver, and kidney divided in cortex and medulla (n = 7 for [18F]PARPi and [18F]FPyPARP, n = 6 for [18F]FTT, n = 5 for [18F]olaparib and [18F]talazoparib).

4.2 PARP as a Biomarker for Replicative Stress

PARP is an important enzyme within the DDR and as such a promising target as a biomarker for replicative stress. To evaluate this hypothesis, different cell lines were provided by the group of Prof. Dr. med. Lars Zender at the University Hospital Tuebingen.[324]

First, two PDAC-derived cell lines were used with and without forced myc expression (Kras Myc p53$^{-/-}$: high replicative stress, pink; Kras p53$^{-/-}$: low replicative stress, black). Cell lines were generated by either introducing myc in a pCAGGS plasmid via electroporation into pancreatic cells from KrasLSL p53loxp mice (high myc, Kras Myc p53$^{-/-}$) or, similarly, introducing Kras into pancreatic cells from p53loxp mice (low myc, Kras p53$^{-/-}$).[325]

The two cell lines were then incubated with the previously described PARP radiotracers and consistently showed higher radiotracer accumulation in the Kras Myc p53$^{-/-}$cell line with higher replicative stress compared to Kras p53$^{-/-}$ cells (exemplarily Figure 24 A, last columns to the right). This was observed for [^{18}F]PARPi and [^{18}F]FTT as well, always featuring a difference of approximately 2-fold (data not shown). With these promising results in hand, we hypothesized that the difference in PARP expression is correlated to the difference in replicative stress in these cells lines, and tested different cell lines for further evidence.

We then received liver progenitor cell-derived single cell clones that overexpress either myc and Kras (high replicative stress, K3C2 and K3C4, pink) or Kras only (low replicative stress, K1C1, K1C2, K5C2 and K5C4, black). Those cell lines were again generated by introduction of either Kras only or both Kras and myc via electroporation in liver cells from p53loxp mice. The cell lines were again incubated with PARP radiotracers to resolve the differences in uptake, together with the previous PDAC cell lines as control.

The liver progenitor cell lines did unfortunately not show consistent PARP radiotracer uptake as exemplarily shown for [^{18}F]FPyPARP (Figure 24 A). First, the clones with presumably high replicative stress, K3C2 and K3C4 (displayed in pink), did not show the highest radiotracer accumulation but were more in the middle range. Second, the relative uptake of the different cell lines to each other changed from experiment to experiment. These experiments were repeated with the reference PARP radiotracers [^{18}F]PARPi and [^{18}F]FTT, but did not yield in conclusive date (data not shown).

A Western blot analysis was performed to reliably quantify PARP1 levels. We observed a prominent band at the size of full-length PARP (116 kDa) and several smaller bands, which are probably caspase cleavage products with a main large fragment with a size of 89 kDa. PARP1 levels indeed differed among the cell lines, however, they seem to be not correlative to the supposed amount of replicative stress (Figure 24 B). Exemplarily, the clone K5C1 is supposed to have only low replicative stress but demonstrated high PARP1 expression in the

Western blot. Unfortunately, no further validation of replicative stress levels (for example DNA fiber assays) beyond the genotype was available.

Furthermore, two human cell lines from the NCI60 panel were tested.[310] As cell lines, ACHN cells (low replicative stress) and Hop63 cells (high replicative stress) were chosen as they showed best response to a newly developed drug targeting RPA3, confirmed by pRPA2 quantification. Again, incubation with different PARP radiotracers yielded inconsistent results and as a consequence, these cell lines were not pursued further (data not shown).
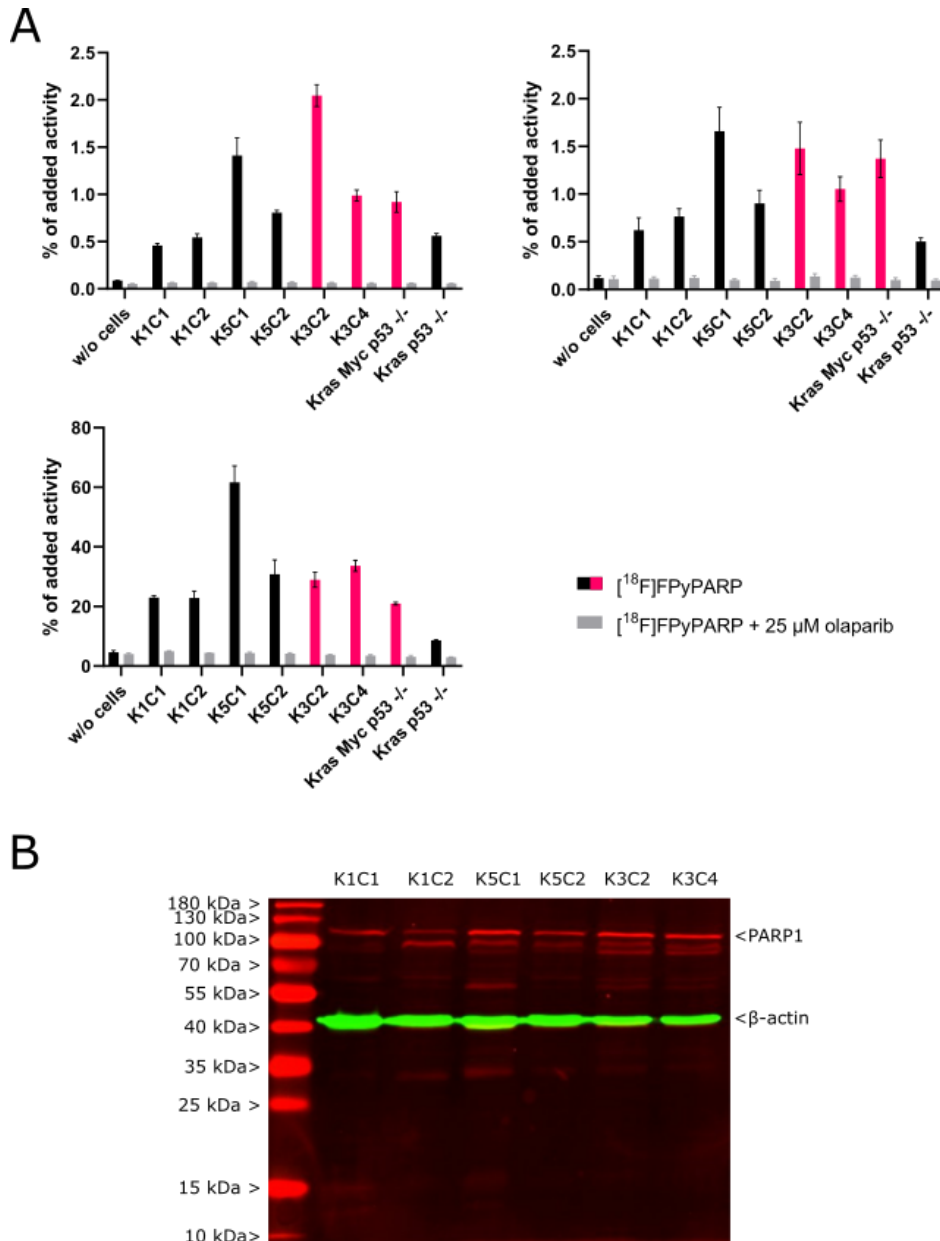
Figure 24: *In vitro* PARP radiotracer uptake experiments in cell lines with different levels of replicative stress. A [18F]FPyPARP uptake in PDAC and in liver progenitor cell lines with different levels of replicative stress (high replicative stress: Kras Myc p53$^{-/-}$, K3C2 and K3C4; low replicative stress: Kras p53$^{-/-}$, K1C1, K1C2, K5C2 and K5C4). Error bars represent the standard deviation of n = 3 biological replicates. **B** Western blot of the liver progenitor cell lines with anti-PARP antibody (full-length: 116 kDa, main cleavage product; 89 kDa).

Since we received mixed results from the cell models based on myc overexpression or patient-derived cell lines, we set out to generate a more reliable and controllable model for replicative stress. Myc is involved in many biological processes, and its overexpression might result in unexpected dysregulation of pathways that can influence the replicative stress response. In addition, our data suggest that the differences in PARP uptake could be caused by unpredictable 'day-to-day' differences in PARP expression, which would hamper applicability *in vivo.*

According to Sulkowski et al., 2-HG produced by mutated IDH suppresses HR and as such is postulated to induce replicative stress.[62] We aimed to utilize this potential connection and overexpressed either IDH as control or mIDH to generate intracellular 2-HG in a controlled fashion under a doxycycline-inducible promotor.[317] We chose two cancer cell lines that are suitable transfection hosts for this model: A neuroblastoma cell line (CHP) and the colorectal cancer line HCT116.

We successfully generated cell lines based on both CHP or HCT116 cells that express either wildtype IDH1 or the IDH1 mutant R132H (mIDH1) together with a FLAG tag for easier detection. Expression of the constructs after incubation with 0.1 µg/mL doxycycline was tested at different time points and found to be stable after 48 hours as determined by anti-FLAG tag Western blot (Figure 25 A). For the CHP IDH1 and the CHP mIDH1 cell line, a red band at the corresponding size of IDH1/mIDH1 appeared after as early as 12 hrs and increased further in intensity until 48 hrs after start of the doxycycline treatment. The same effect was confirmed for the HCT116 cells (data not shown).

2-HG accumulation was assessed with a commercial coupled fluorimetric assay kit (Figure 25 B and C upper images). Cells were incubated with doxycycline over several days (0 h, 24 h, 48 h, 72 h, 96 h, and 120 h) to induce sufficient 2-HG production, lysed, and subjected to colorimetric 2-HG analysis. Although the data fluctuated over time, more 2-HG was clearly observed in the CHP and HCT116 cell overexpressing the mutant IDH1. More fluctuation in the data was observed in the CHP cells, which was caused by rapid detachment of the cells during doxycycline treatment and therefore loss of cell material.

Then, cells treated with doxycycline were probed for [^{18}F]PARPi uptake. No difference in [^{18}F]PARPi uptake was observed between the untransfected and the transfected control cells and the mIDH expressing cells for both cell lines, neither between the groups nor over time. In consequence, this shows that increased 2-hydroxyglutarate levels did not correlate with increased [^{18}F]PARPi uptake (Figure 25 B and C lower images). Although the 2-HG quantification data are noisy, the clear lack of correlation discouraged us from repeating the experiment.

Additionally, we did not observe a correlation between 2-HG accumulation and expression of replicative stress biomarkers in Western blot (γH2AX, pRPA2, data not shown). This led to discontinuation of these cell lines for this project.
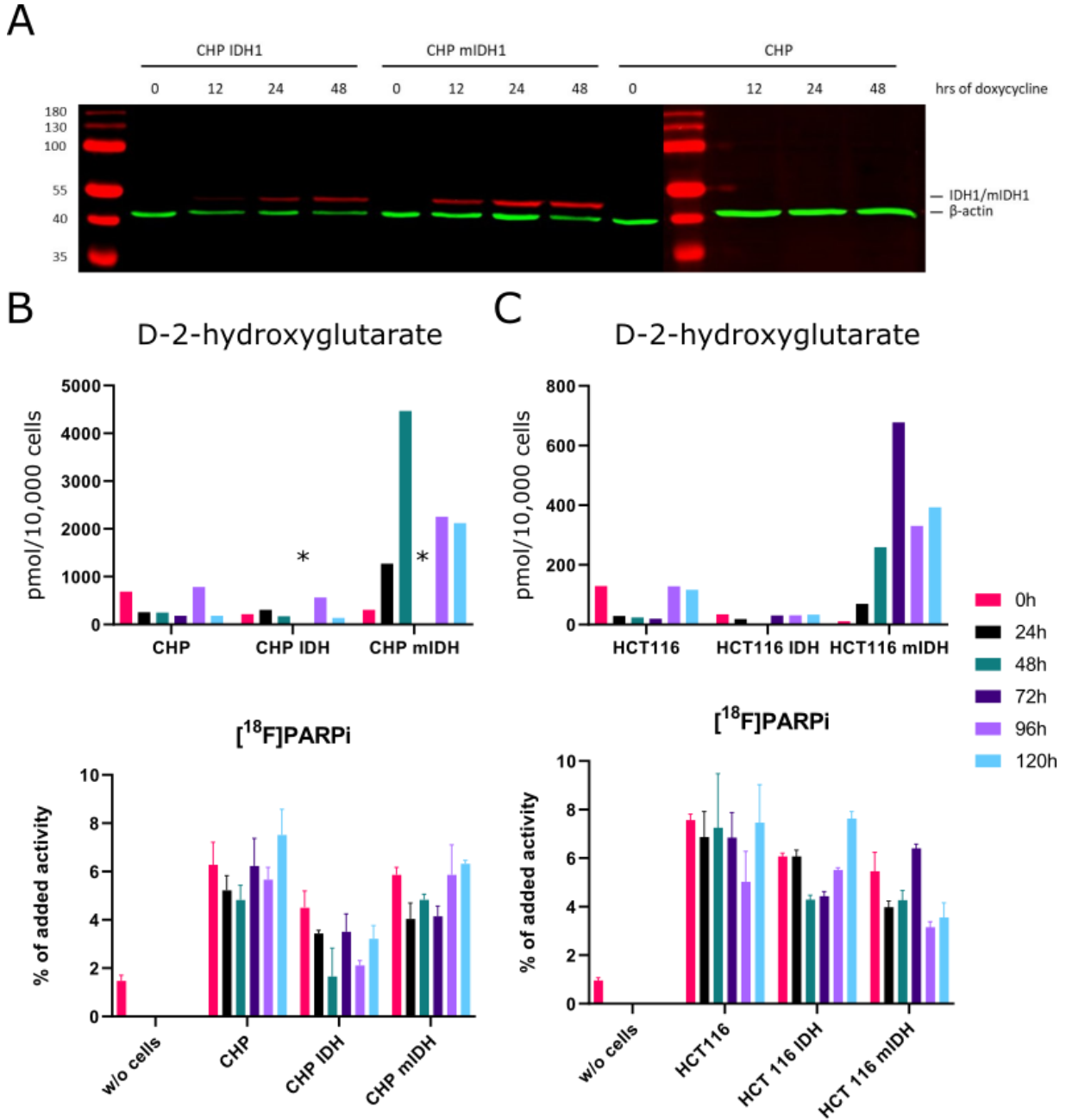
Figure 25: D-2-hydroxyglutarate levels and [^{18}F]PARPi uptake in cell lines overexpressing mIDH. A Western blot of CHP cells treated with doxycycline for different amounts of time. An anti-FLAG antibody was used for IDH/mIDH detection and anti-β-actin for loading control. **B** D-2-hydroxyglutarate levels and [^{18}F]PARPi uptake in untransfected CHP cells, CHP cells overexpressing IDH and CHP cells overexpressing mIDH. * indicates excluded data due to experimental error (n = 1). Error bars represent the standard deviation of n = 3 biological replicates. **C** The same experiment with HCT116 cells.

With the previous cell models, we could not determine if the models are just not exhibiting sufficiently increased levels of replicative stress for detection with [^{18}F]PARPi, or if other

cellular processes like a shift in translation rates interfere with radiotracer uptake. On the other hand, we were not yet able to exclude that PARP is a suitable biomarker for replicative stress. To study this further, we decided to chemically induce replicative stress according to published procedures with CPT and HU treatment.[109,311,312] CPT inhibits topoisomerase 1, a DNA-unwinding enzyme, and HU depletes the dNTP pool, both leading to increased replicative stress in cells.

HCT116 cells were treated with literature-known concentrations of CPT (1 µM) for 1 hour before [^{18}F]PARPi incubation. We did not observe any difference in [^{18}F]PARPi uptake in HCT116 cell treated with CPT (Figure 26 A). Also, we tested HU conditions provided by Zender Lab which they used as a control for induction of replicative stress in the PDAC cell lines and we did not observe any difference either (Figure 26 B). To ensure that slight changes in the protocol didn't have an effect on experimental outcome, these two cell lines were more extensively tested with a concentration range and different time points of HU treatment (1 mM, 2 mM, 1 h, 2 h). Again, we did not observe any difference in [^{18}F]PARPi uptake between the treatments, however, the 2-fold higher uptake in the Kras Myc p53$^{-/-}$ cells was still present (Figure 26 C and D).
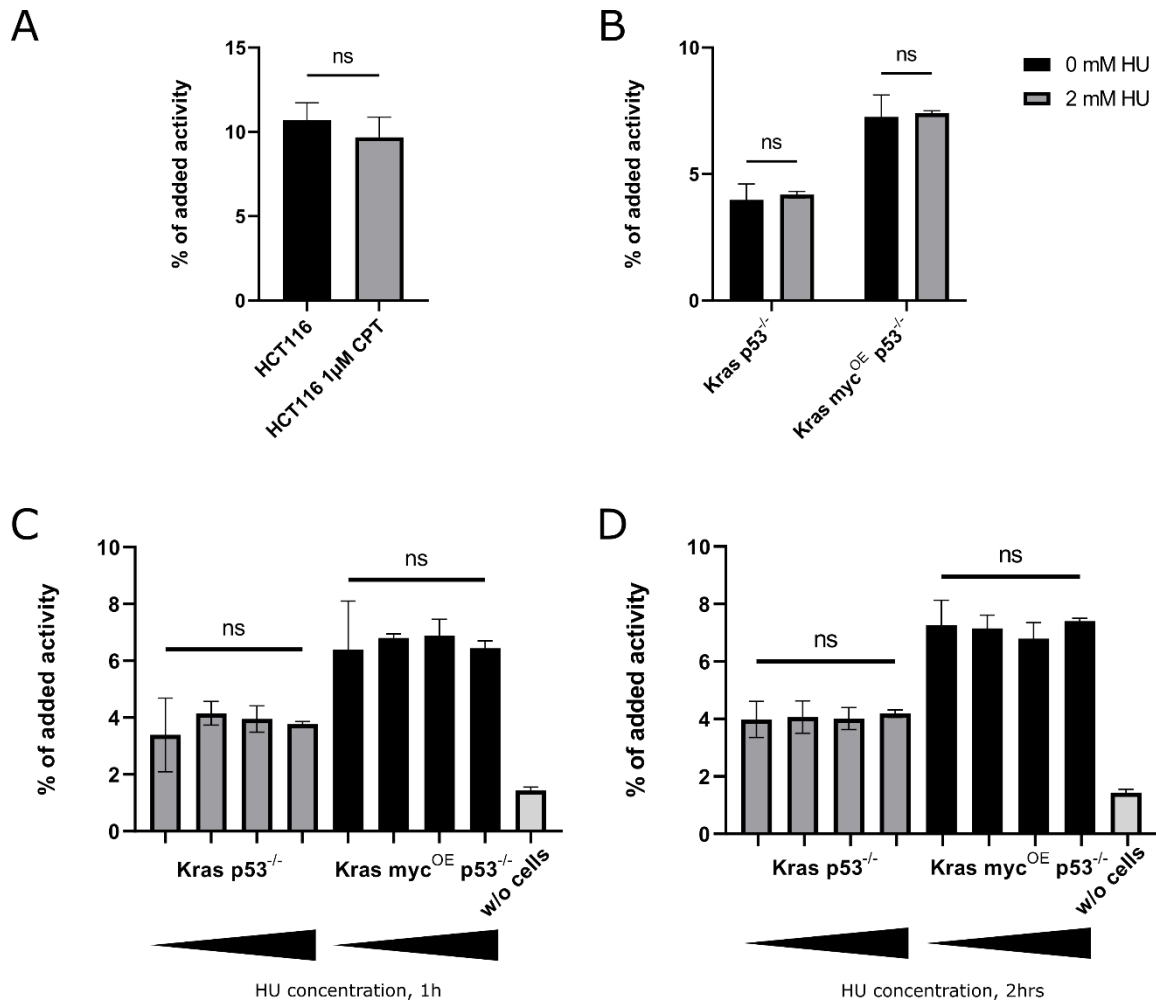
Figure 26: Cell uptake studies in chemically induced replicative stress models. A [^{18}F]PARPi uptake in HCT116 cells incubated with 1 µM CPT. **B** [^{18}F]PARPi uptake in a cell line with low replicative stress (Kras p53$^{-/-}$) and high replicative stress (Kras myc^{OE} p53$^{-/-}$) incubated with 2 mM HU for 2 h. **C** [^{18}F]PARPi uptake in the low/high stress cell lines with increasing concentrations of HU for 1 h. **D** [^{18}F]PARPi uptake in the low/high stress cell lines with increasing concentrations of HU for 2 h. HU concentrations include from left to right 0 mM, 0.5 mM, 1 mM and 2 mM. Error bars represent the standard deviation of n = 3 or n = 4 biological replicates.

Taken together, these results suggest that PARP is not a suitable biomarker for replicative stress. Although PARP is a good tumor biomarker in general, we haven't found evidence that PARP is upregulated during replicative stress conditions in several different cell models based on different approaches to induce replicative stress. If PARP enzymes play a role in replicative stress, it might be not based on increased expression of PARP1 but more on an increase in PARP activity or subcellular redistribution of the enzyme. Thus, PARP radiotracers are not suitable to determine levels of replicative stress as they can only reflect the absolute PARP enzyme levels and not their activity.

In order to determine a more suitable biomarker for replicative stress, we chose a set of potential target enzymes to evaluate. Those enzymes were chosen according to two criteria: first, they are involved in the signaling cascades of the replicative stress response, and second, small molecule drugs are available. The latter is a prerequisite for the development of specific radiotracers.

To assess whether the chosen targets are suitable as specific replicative stress biomarkers, Western blot analysis was performed with the PDAC cell models and chemically induced replicative stress with HU, as this was deemed the most reliable method to introduce replicative stress.

The expected increase in target expression between control cell lysates and cell lysates stressed with HU treatment was not observed for CHK1 and APOBEC (Figure 27). The other antigens were only tested at the highest HU concentration in a broader screening experiment, and did either not show any signal at the expected size (ATR and ATM) or a decrease in signal (Wee1, data not shown). Thus, those targets were not pursued further.
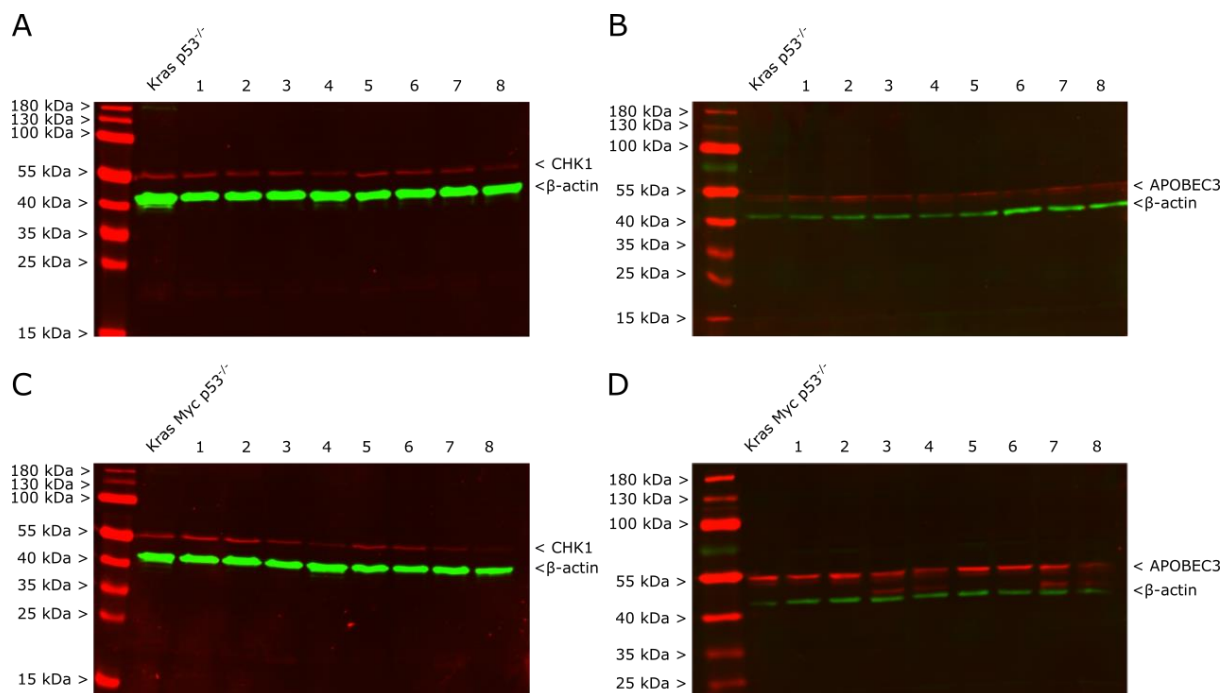
Figure 27: Representative Western blot images with Kras p53$^{-/-}$ and Kras Myc p53$^{-/-}$ cell lysates treated with HU. Cells were incubated with either 1 mM (1-4) or 2 mM (5-8) HU for 1, 2, 24, 48 hrs, respectively. **A** Anti-CHK1 Western blot with Kras p53$^{-/-}$ cell lysates. **B** Anti-APOBEC Western blot with Kras p53$^{-/-}$ cell lysates.**C** Anti-CHK1 Western blot with Kras Myc p53$^{-/-}$ cell lysates.**D** Anti-APOBEC Western blot with Kras Myc p53$^{-/-}$ cell lysates.

These findings suggest that the replicative stress response is a cascade of protein activation instead of expression, which is difficult to resolve with PET radiotracers. Genetically encoded reporters offer an alternative for longitudinal quantification of signaling pathway activation that might be a useful tool to study the dynamics of replicative stress and to assess response to newly developed therapies.

4.3 Design and Evaluation of Three Novel Reporter Gene Systems

In parallel to the identification of novel biomarkers for replicative stress, we set out to investigate HaloTag, SNAPTag and CLIPTag for their potential as nuclear RGS. We designed and synthesized radiotracers for each protein tag: [18F]FB-HTL targeting HaloTag, [18F]pFBG, [18F]mFBG, and [18F]FBBG for SNAPTag, and [18F]pFBC as a CLIPTag radiotracer (contributions according to Chapter 8.1). Here, [18F]mFBG was synthesized as an alternative to [18F]pFBG as we observed apparent defluorination *in vivo*. The radiotracers were designed considering potential BBB penetration, thus they feature moderate lipophilicity (clogP between 2.14 and 5.11) and a molecular weight below 500 Da ([18F]FB-HTL 345 Da, [18F]pFBG and [18F]mFBG 258 Da, [18F]FBBG 467 Da, and [18F]pFBC 218 Da).

[18F]FB-HTL was synthesized using [18F]SFB as synthon that was conjugated with the chloroalkane precursor. [18F]pFBG and [18F]mFBG were afforded by addition of the respective [18F]p/m-fluorobenzyl alcohol intermediate to DABCO-guaninyl chloride, while [18F]FBBG again utilized [18F]SFB and commercially available O^6-(4-aminomethyl-benzyl)guanine as precursor.[306] [18F]pFBC was synthesized using a copper-mediated radiofluorination reaction, [18F]TBAF, and a boropinacolate precursor. Since nitrogen-rich aromatic compounds like [18F]pFBC are known to be challenging for such reactions, the reaction conditions needed to be optimized with DoE.

The radiotracer syntheses were automated on our modules and yielded [18F]FB-HTL, [18F]pFBG, [18F]mFBG, [18F]FBBG and [18F]pFBC in good yields and radiochemical purity (Table 13).

Table 13: Synthesis data of the reporter radiotracers. n = 18 for [18F]FB-HTL,[2] n = 3 for [18F]pFBG, n = 3 for [18F]mFBG, n = 3 for [18F]pFBBG, and n = 2 for [18F]pFBC.[3]

	% RCY	RCP	MA (GBq/µmol)	SYNTHESIS TIME (min)
[18F]FB-HTL	16 ± 7	> 95 %	36 – 380	87
[18F]pFBG	22 ± 8	> 95 %	41 – 56	108
[18F]mFBG	44 ± 13	> 95 %	41 – 56	103
[18F]FBBG	12 ± 4	> 95 %	25 – 107	79
[18F]pFBC	25	> 95 %	165 – 248	61

[2] One radiosynthesis was excluded due to presence of non-radioactive fluoride residues in the reactor that influenced molar activity

[3] Here, only the results from the fully automated and optimized synthesis was used. Other syntheses using a tin precursor were used for experiments which yielded comparable results

In addition, the logD value was experimentally determined using the shake-flask method to measure lipophilicity and found to be 3.27 for [^{18}F]FB-HTL in line with the previously calculated clogP (3.45). A logD value between 1 and 3 is usually considered as suitable for BBB penetration.[326] Stability of the radiotracers was assessed in mouse serum, and no radiometabolites were detected over a time course of 240 minutes (Figure 28).
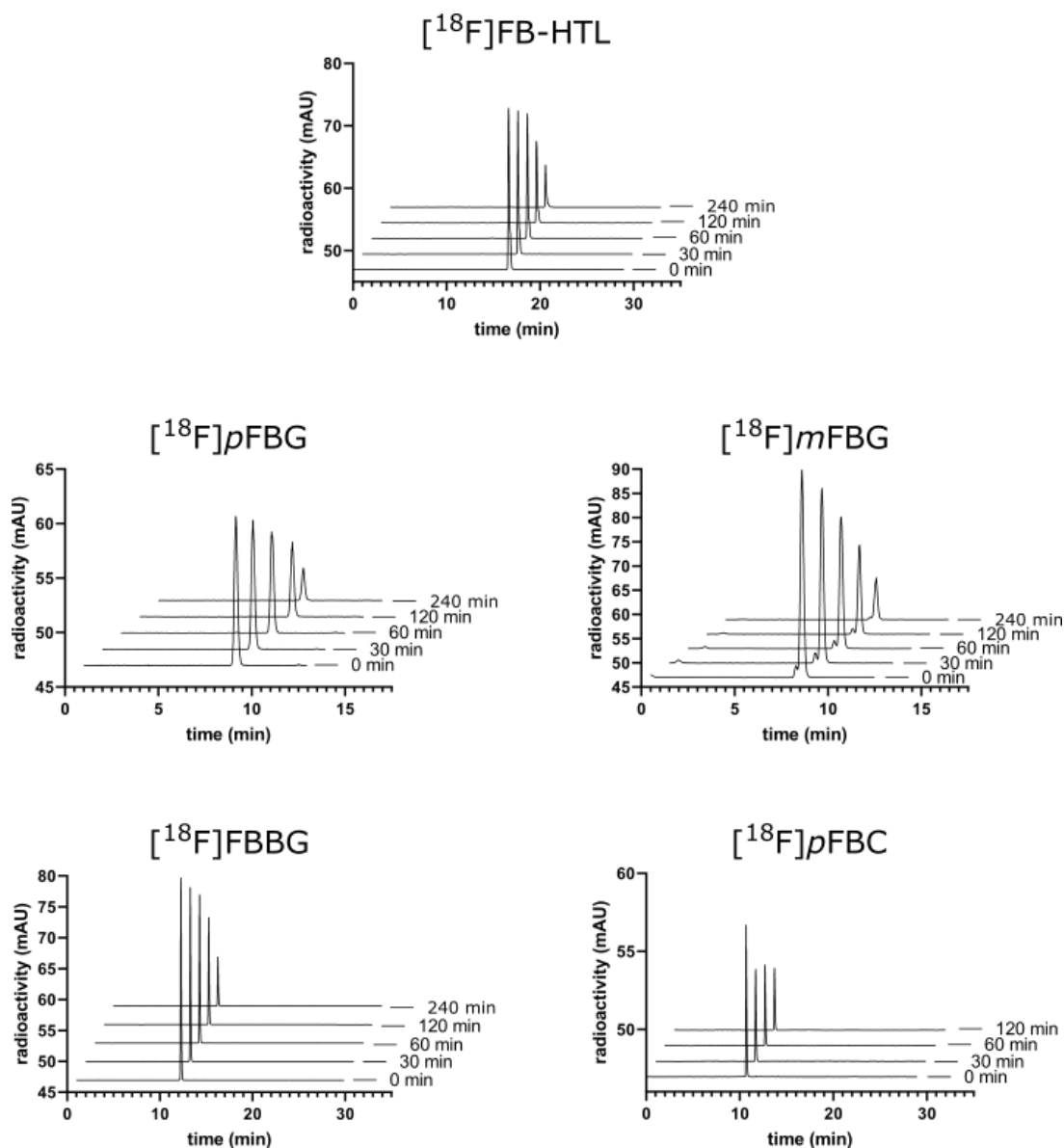
Figure 28: Serum stability analysis of the reporter radiotracers. Stability was assessed in mouse serum at 37°C.

4.3.1 Cell Model Generation and *In Vitro* Evaluation

As cell model, we generated HEK-reporter cell lines overexpressing the respective reporter under a constitutively active CMV promotor using a standard Lipofectamine 3000 transfection

protocol. The reporter sequence was flanked with an HA-tag as well as a myc-tag, coupled to an Ig-κ signal peptide for protein secretion at the *N*-terminus, and a *C*-terminal platelet-derived growth factor receptor (PDGFR) transmembrane domain for cell-surface-tethering (Figure 29 A). After selection and generation of stable cell lines using limiting serial dilution, we extensively characterized the transfected HEK-reporter cells for reporter expression on the cell surface.[327]

HEK-reporter lysates were tested for reporter expression with Western blot and an anti-myc antibody, revealing a clearly distinguishable band at the sizes of the respective reporter proteins (HaloTag contruct: 44 kDa, SNAPTag and CLIPTag construct: 30 kDa, Figure 29 B). We hypothesize that the weaker bands below the main reporter band correspond to reporter protein where potentially parts of the reporter proteins like the transmembrane domain or the HA-tag are cleaved off.

Confocal microscopy with commercially available ligands was performed to visualize and confirm cell surface expression (Figure 29 C). The microscopy images revealed strong fluorescence signal on the cell surface for all three cell lines. Additionally, the fluorescence was blockable by co-incubation with 1 μM of the respective non-radioactive standard (Figure 29 C).

We were able to synthesize and automate four main radiotracers for three different reporter proteins. One radiotracer was additionally synthesized as alternative. The chosen HEK293-based cell model reliably overexpresses the respective reporter in a sufficient amount on the cell surface, which renders the reporter protein more easily accessible by the radiotracers, as they don't need to cross the plasma membrane. The reporter proteins were tested for their functionality with commercial fluorescent ligands and showed high and specific fluorescent signal.

A
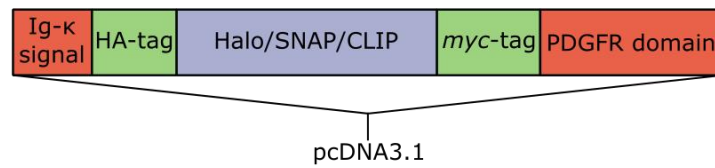
B
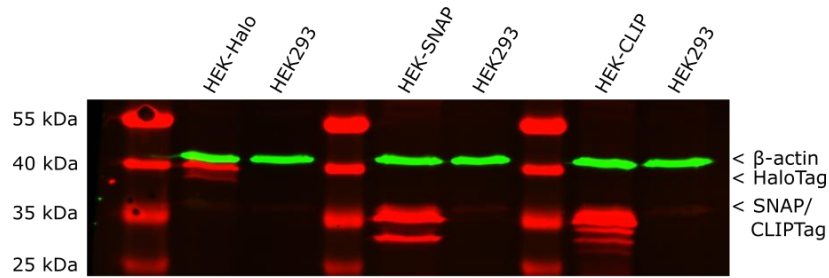
C
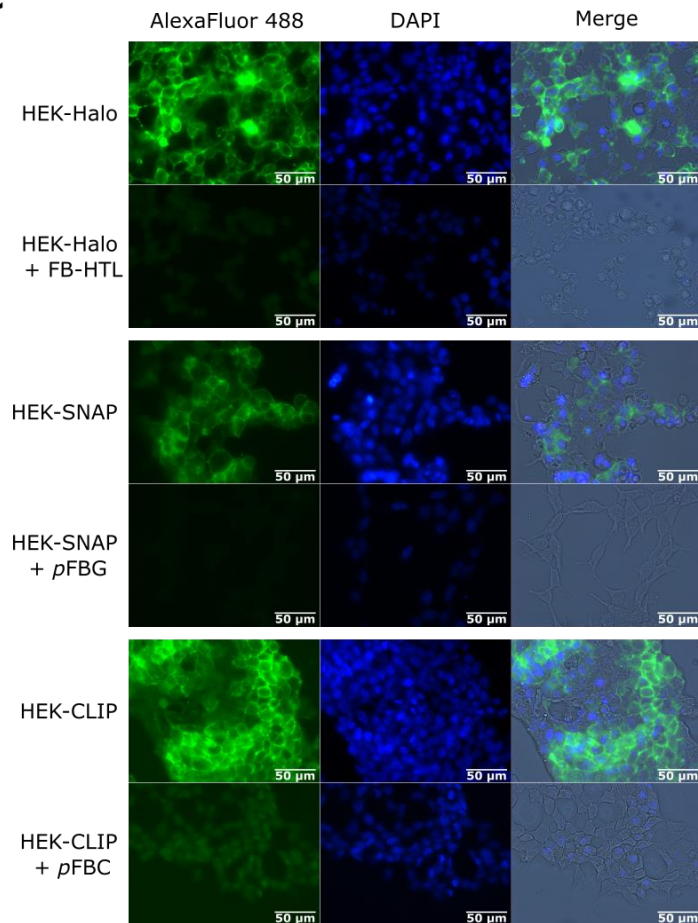
Figure 29: *In vitro* characterization of the HEK-reporter cells. A Schematic display of the reporter construct transfected into HEK293 cells. **B** Western blot analysis of HEK-reporter cell lysates with HEK293 cells as control; β-actin expression was visualized in green as loading control; myc-tag specific signal is displayed in red. **C** Microscopy images of HEK-reporter and HEK293 cells labeled with AlexaFluor 488 conjugated commercial ligands and DAPI in the presence or absence of excess non-fluorescent compound (1 µM FB-HTL, 1 µM *p*FBG and 1 µM *p*FBC).

RESULTS AND DISCUSSION

With both the cell model and the automated radiotracer syntheses in hand, specific binding of the respective radiotracer to the cell model was evaluated. HEK-reporter cells and untransfected control cells were incubated with the respective radiotracer, lysed, and analyzed by SDS-PAGE with subsequent autoradiography. The autoradiograph showed a band at the corresponding size of the reporter protein for all four reporter-radiotracer pairs ([^{18}F]FB-HTL and HaloTag, [^{18}F]pFBG and SNAPTag, [^{18}F]FBBG and SNAPTag and [^{18}F]pFBC and CLIPTag). These results were cross-validated by simultaneous Western blotting and subsequent staining of the gel with Coomassie as loading control (Figure 30 A). The Coomassie protein stain revealed similar protein load for HEK-reporter and HEK293 control cells, if not less for the control cells for [^{18}F]pFBG and [^{18}F]FBBG. The Western blots with anti-myc antibody showed a band at the size of the respective reporter protein (33 kDa for HaloTag and 20 kDa for SNAP- and CLIPTag).

This demonstrates specific and covalent binding of the radiotracers to the respective reporter protein. Also, slightly smaller bands than the main reporter protein band are visible in the autoradiograph, in line with the previously performed Western blot (Figure 29 B). This observation supports the hypothesis that those bands correspond to the partially cleaved reporter protein and that the cleavage products do not affect the binding pocket.

Further, HEK-reporter cells and control cells were incubated with the respective radiotracer and radiotracer accumulation was quantified by gamma-counting. Indeed, we observed a significantly higher radioactive signal in all HEK-reporter cells compared to HEK293 control cells (Figure 30 B, HEK-Halo: $p < 0.0001$, HEK-SNAP: $p < 0.0001$ for [^{18}F]pFBG, $p = 0.0001$ for [^{18}F]FBBG, Student's t-test with Welch's correction; HEK-CLIP: $p = 0.0037$, Student's t-test). In addition, the radioactive signal was blockable to baseline by co-incubation with the non-radioactive standard, verifying specificity of the radiotracers to the respective reporter protein (Figure 30 B, HEK-Halo: p < 0.0001, HEK-SNAP: p < 0.0001 for [^{18}F]pFBG, p = 0.0001 for [^{18}F]FBBG, HEK-CLIP: p = 0.0145, Student's t-test with Welch's correction).

Although all four radiotracer uptake experiments resulted in significant and clear accumulation, the relative change between control cells and HEK-reporter cells was highest for [^{18}F]pFBG (65.5-fold), followed by [^{18}F]FB-HTL (25.4-fold) and [^{18}F]FBBG (24.0-fold). As already visible in the graph, uptake of [^{18}F]pFBC, while still significant, was not as high directly compared to the other three reporter pairs (5.0-fold). Similarly, blocking was most effective for [^{18}F]pFBG (40.5-fold), followed by [^{18}F]FBBG (24.0-fold), [^{18}F]FB-HTL (22.2-fold) and [^{18}F]pFBC (5.6-fold). This could be either due to better reaction kinetics of HaloTag and SNAPTag, better specificity of the respective radiotracers, or differences in expression levels of the reporter proteins. However, these data do not necessarily predict *in vivo* performance, which was thus assessed in a xenograft study.

97
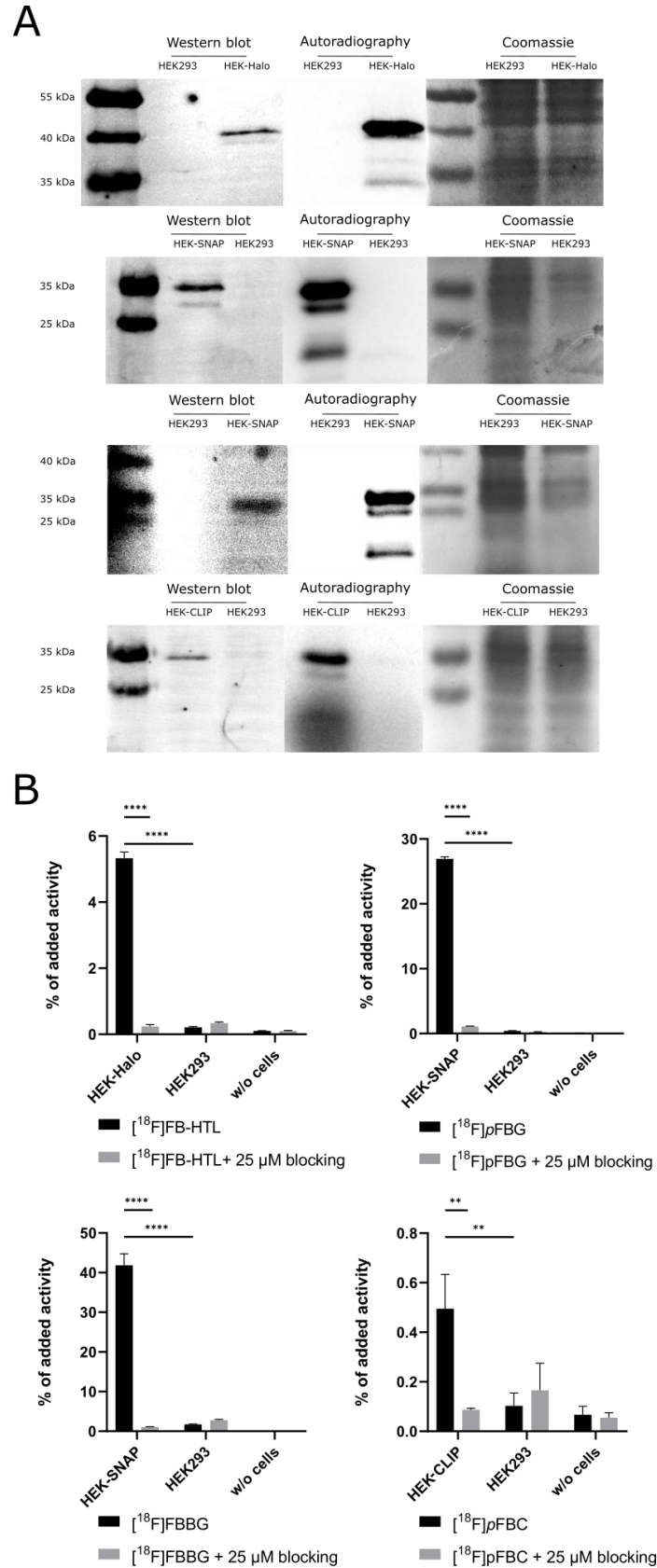
Figure 30: *In vitro* radiotracer uptake experiments. A SDS-PAGE autoradiography analysis of HEK-reporter and untransfected HEK293 cell lysates. Western blot analysis and Coomassie staining were performed as expression and loading control, respectively. **B** Cell uptake of the respective radiotracer in HEK-reporter and HEK293 cells with additional blocking with the corresponding non-radioactive compound. Error bars represent the standard deviation of n = 4 biological replicates. .

4.3.2 *In Vivo* Xenograft Study

In the pilot *in vivo* study, female NOD.CB17-*Prkdc^{scid}* mice (n = 5 per group) were injected with either HEK-reporter or HEK293 cells subcutaneously in the right flank. After xenograft growth, dynamic PET scans with were performed in order to visualize the distribution of the radiotracers in the animals (Figure 31).

[^{18}F]FB-HTL showed generally homogenous distribution of the radiotracer in the body. The kidneys and the bladder were clearly distinguishable from the surrounding tissue, and the liver showed moderate radiotracer accumulation. This points towards a mainly renal excretion of [^{18}F]FB-HTL and good clearance from background tissues. Notably, [^{18}F]FB-HTL showed non-specific signal in the brain, pointing out the ability to cross the BBB (Figure 31 A).
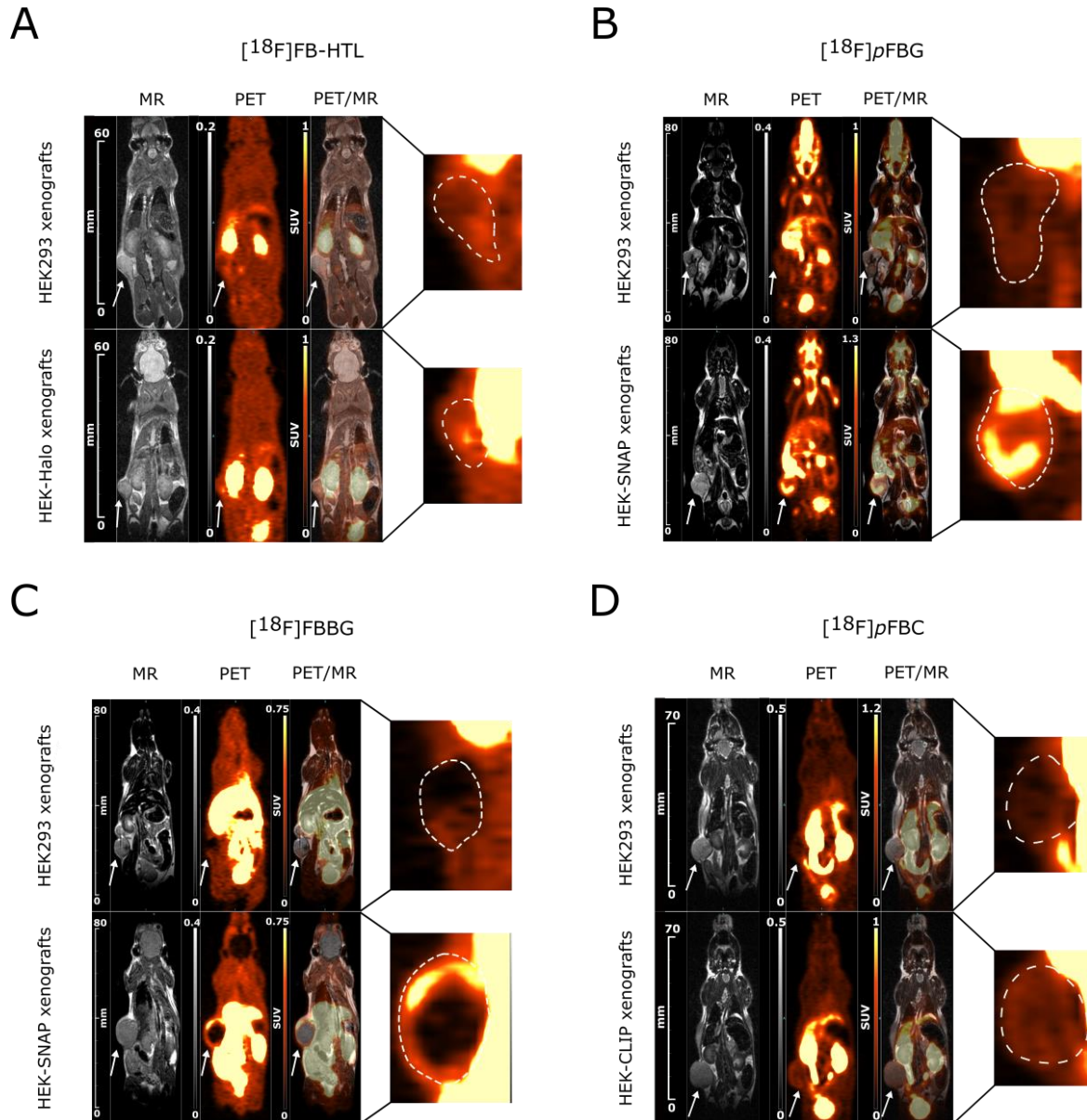
Figure 31: Representative PET and MR images of mice imaged with the reporter radiotracers. Images represent the last 10 min of a 1 h dynamic PET scan of mice injected with [^{18}F]FB-HTL (**A**), [^{18}F]pFBG (**B**), [^{18}F]FBBG (**C**), and [^{18}F]pFBC (**D**).

[^{18}F]pFBG showed moderate accumulation in liver and kidneys and the bladder (Figure 31 B). Clearly, most radioactive signal was visible in the bones, especially the skull, joints, ribs and spine. In the dynamic PET data, [^{18}F]pFBG signal started appearing in the bones starting already approximately 15 minutes after radiotracer administration, which is an indication of defluorination of the radiotracer. This means that the ^{18}F-label is cleaved off the radiotracer by phase I metabolism, and free fluoride accumulates in the bone.[328] In order to potentially increase the metabolic stability of the radiotracer, [^{18}F]mFBG was synthesized as shifting the radiolabel from the para to the meta position was reported to prevent dehalogenation for other molecules.[329] However, evaluation in naïve NOD.CB17-*Prkdc*^{scid} mice showed that the

shift of the label did not improve stability, and the radiotracer still showed high bone uptake (Figure 32).
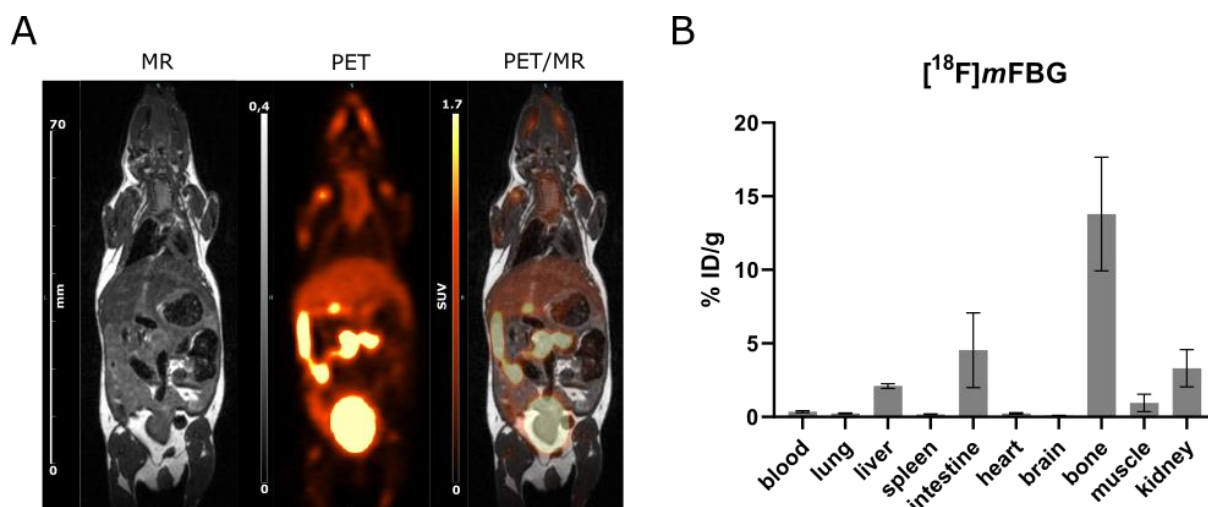
Figure 32: Representative PET and MR images and *ex vivo* biodistribution analysis of naïve mice injected with [¹⁸F]*m*FBG. A Representative PET and MR images of naive mice injected with [¹⁸F]*m*FBG. **B** *Ex vivo* biodistribution analysis of naïve mice 1.5 hrs p.i. Error bars represent the standard deviation of n = 3 mice.

[¹⁸F]FBBG presented with high uptake in the abdominal region, especially in liver, kidneys, bladder and intestine (Figure 31 C). From the PET images, [¹⁸F]FBBG was preferentially cleared hepatobiliarily as indicated by the high liver uptake in comparison to the kidneys. Otherwise, the radiotracer was distributed homogenously within the body, and no signs of bone uptake were visible. Notably, both [¹⁸F]*p*FBG and [¹⁸F]FBBG did not show baseline brain uptake in the PET images.

[¹⁸F]*p*FBC featured even lower background organ uptake in direct comparison to the other three reporter-radiotracer pairs, and had prominent uptake in kidneys and the bladder (Figure 31 D). Additionally, moderate liver uptake and accumulation in parts of the intestines was observed. [¹⁸F]*p*FBC thus seemed to be excreted favorably renally and has a promising low background. Also, no notable brain PET signal was observed.

For all four radiotracers, increased uptake in the HEK-reporter xenografts compared to HEK293 xenografts was observed. Interestingly, [¹⁸F]FB-HTL, [¹⁸F]*p*FBG, and [¹⁸F]FBBG displayed heterogenous xenograft enrichment with most of the radioactivity accumulating at the edges and low signal towards the xenograft core. In contrast, [¹⁸F]*p*FBC showed more homogenous distribution within the xenograft. This is partially due to inhomogeneous growth of the xenografts, with tumor sizes increasing rapidly towards the PET imaging time point. Over time, the xenografts could have lost the reporter protein expression in parts of the tumor, or the xenografts might have become necrotic towards the core due to large mass.

So far, only [¹⁸F]FB-HTL showed non-specific signal in the brain, pointing out the ability to cross the BBB (Figure 31 A). For [¹⁸F]*p*FBG, [¹⁸F]*m*FBG, [¹⁸F]FBBG and [¹⁸F]*p*FBC, no

persisting radioactive signal in the brain was visible in the PET data (Figure 31 B-D). However, the PET images only represent the last 10 minutes of a 1 hour dynamic PET scan, and efflux transporters might actively clear the brain from the radiotracer, Thus, it is important to analyze the brain TACs for a dynamic image of radiotracer perfusion and efflux.

Subsequently, after the PET and MRI scans, the mice were sacrificed, and organs of interest were collected for biodistribution analysis by gamma-counting (Figure 33 A). In line with the PET data, [^{18}F]FB-HTL displayed similarly moderate accumulation in all organs, except the kidney which was the organ with by far highest uptake. As expected, bone uptake of [^{18}F]pFBG was almost as high as the kidney uptake, confirming strong defluorination of the radiotracer. Also, varying intestine and moderate kidney uptake was visible. In contrast, [^{18}F]FBBG showed high liver, kidney and intestine uptake. [^{18}F]pFBC presented with expected high kidney uptake, and moderate intestine and liver accumulation.

To evaluate *in vivo* performance of the reporter-radiotracer pairs, HEK-reporter and HEK293 control xenograft radiotracer accumulation was compared. Mean absolute xenograft uptake and difference to control xenografts was highest for the SNAPTag radiotracers [^{18}F]pFBG and [^{18}F]FBBG ([^{18}F]pFBG: 3.9 vs 1.0 %ID/g, and [^{18}F]FBBG: 4.8 vs 0.7 %ID/g), followed by [^{18}F]FB-HTL (2.1 vs 1.2 %ID/g) and [^{18}F]pFBC (0.9 vs 0.5 %ID/g). Hence, the results are in line with the *in vitro* performance of the radiotracers.

To determine the ability of the radiotracers to delineate reporter expression from the surrounding tissue, the tumor-to-background ratios were compared, with the muscle as reference tissue. TMRs were consistently higher in HEK-reporter xenografts compared to controls. Like the absolute xenograft uptake, [^{18}F]pFBG and [^{18}F]FBBG featured the highest TMR in direct comparison to each other and the controls ([^{18}F]pFBG: 10.6 vs 1.7, and [^{18}F]FBBG: 7.5 vs 0.9). However, the variation was relatively high, as already indicated by the heterogenous radiotracer distribution in the xenografts in the PET data. Interestingly, [^{18}F]pFBC also exhibited a very good TMR with more homogeneous distribution (5 vs 1.7), which underlines the importance of using a reference tissue. [^{18}F]FB-HTL showed a good TMR (2.0 vs 1.1), and the data were very homogeneous. In comparison to the other control groups, HEK293 xenografts measured with [^{18}F]FB-HTL had a higher variance, which influenced the statistical significance analysis. Overall, statistical analysis confirmed a significant increase for all four radiotracers (Figure 33 B, HEK-Halo: p = 0.0034, Student's t-test; HEK-SNAP: p = 0.045 for [^{18}F]pFBG, p = 0.0343 for [^{18}F]FBBG, HEK-CLIP: p = 0.0379, Student's t-test with Welch's correction).

In order to compare radiotracer excretion, LKRs were calculated and showed mainly renal clearance for all four reporter radiotracers (Figure 33 C). As already visualized in the PET images, [^{18}F]FBBG had the highest LKR (0.66), indicating more balanced renal and

hepatobiliary clearance. In contrast, [^{18}F]pFBC showed almost exclusively renal clearance (0.10).
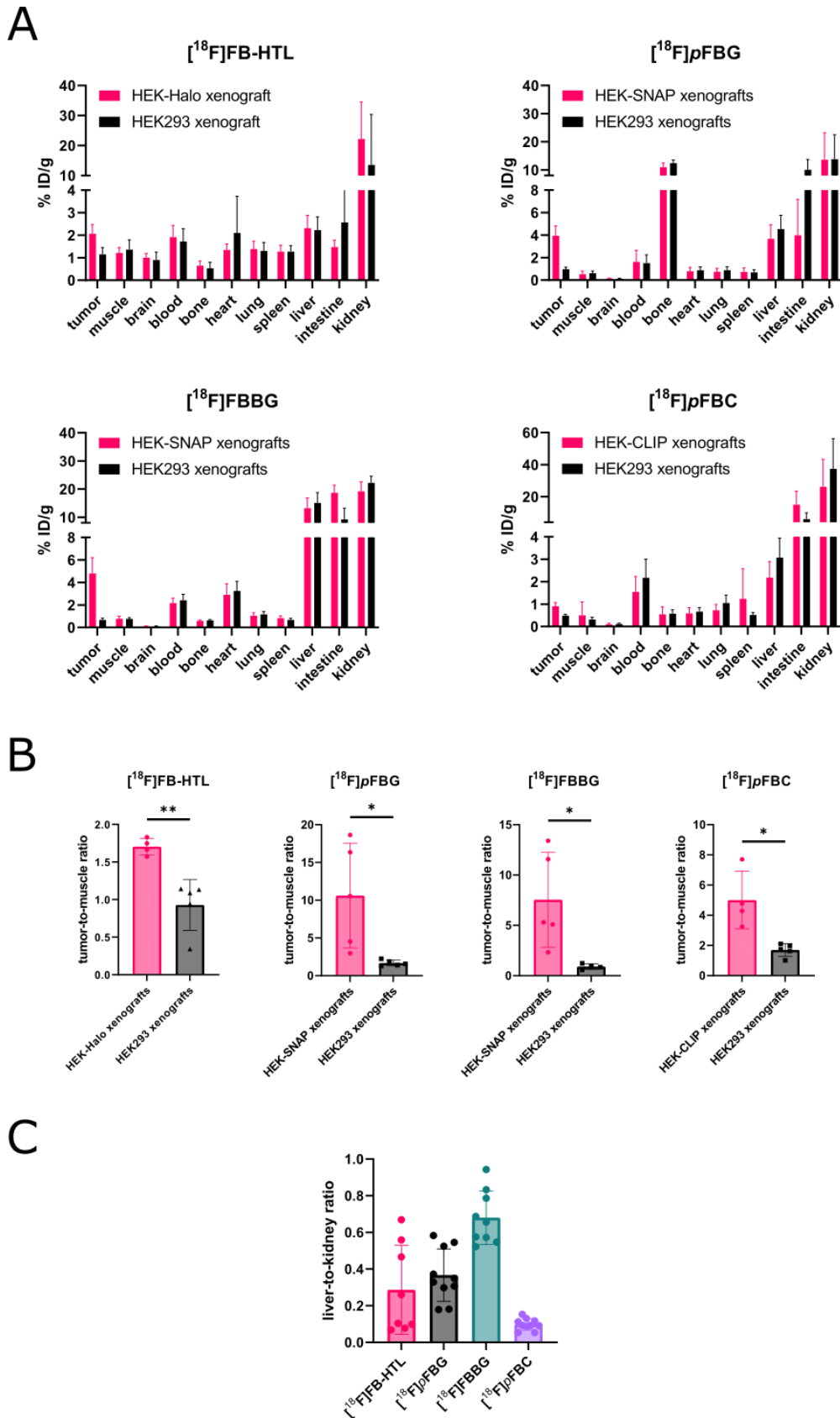
Figure 33: *Ex vivo* **quantification of radiotracer uptake. A** Quantification of residual radioactivity by gamma-counting of selected organs. Error bars represent the standard deviation of n = 4 ([^{18}F]FB-HTL, [^{18}F]FBBG control

xenografts, and [18F]pFBC) or n = 5 mice. **B** Calculated TMRs for all four reporter radiotracers; n = 4 ([18F]FB-HTL, [18F]FBBG control xenografts, and [18F]pFBC) or n = 5 mice. **C.** Comparison of the LKRs; n = 8 for [18F]FB-HTL, n = 10 for [18F]pFBG and [18F]pFBC, n = 9 for [18F]FBBG.

For more dynamic insights in radiotracer biodistribution within the first hour, two mice of each group underwent a dynamic PET scan. The TACs of the xenografts confirmed increased radiotracer uptake in the HEK-reporter xenografts for all four reporter-radiotracer pairs (Figure 34, HEK-reporter in pink). As expected, [18F]pFBG and [18F]FBBG showed the highest difference to control xenografts, but also the highest standard deviation.
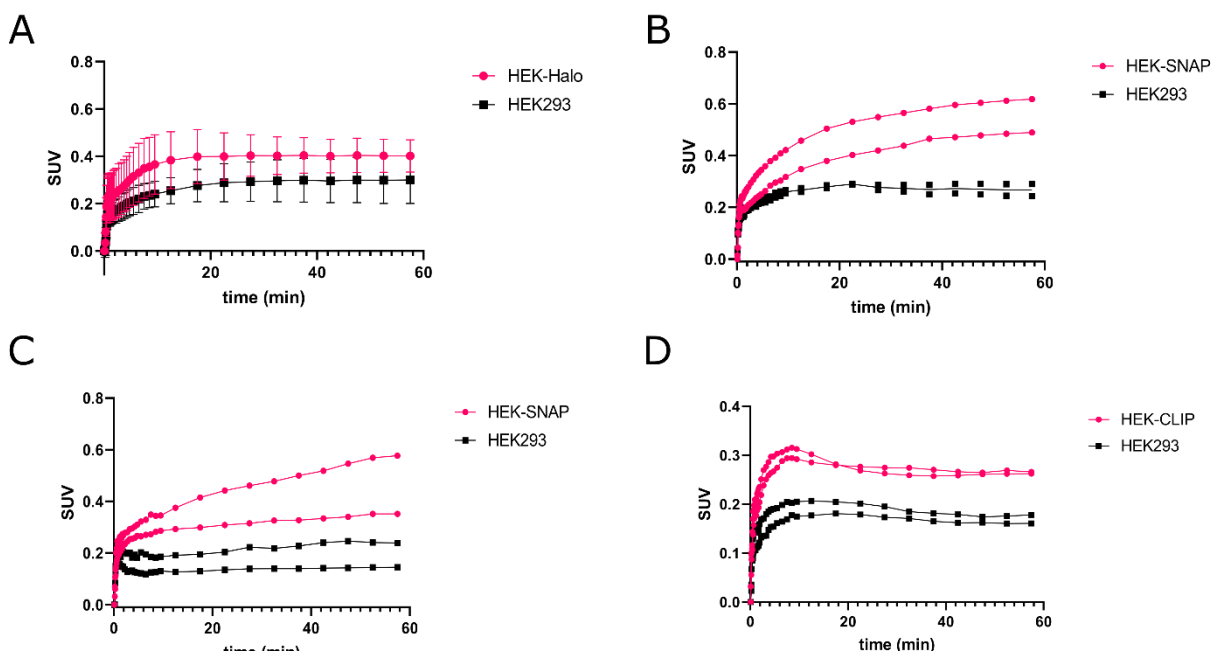
Figure 34: TACs of xenografts over a time course of 60 min p.i. A [18F]FB-HTL (Error bars represent the standard deviation of n = 5 mice). **B** [18F]pFBG (n = 2). **C** [18F]FBBG (n = 2). **D** [18F]pFBC (n = 2).

Liver and kidney TACs verified the excretion routes of the radiotracers. All radiotracers except for [18F]FBBG showed fast liver clearance and increasing radiotracer accumulation in the kidneys, while [18F]FBBG exhibited more balanced renal and hepatobiliary clearance.

The brain TACs were used to assess potential BBB penetration, since a perfusion peak in the TAC indicates initial brain uptake. It is generally agreed that an SUV above 1.5 is a good indicator of actual BBB penetration of radiotracers.[206] For both [18F]FB-HTL and [18F]pFBC, a clear perfusion peak with an SUV above 1.5 was observed in the brain TAC, and [18F]FB-HTL also exhibited persistent brain uptake (Figure 34). This hints towards unspecific brain uptake, and rapid efflux of [18F]pFBC from the brain tissue as no residual radioactivity in the brain was detected in the PET images and the *ex vivo* biodistribution data. The SNAPTag radiotracers did not show a clear perfusion peak, and the values were below an SUV of 1.5, thus they didn't seem to exhibit actual brain uptake.

The heart TAC was used to calculate the blood half-life using the two-phase decay fit in GraphPad Prism and found to be 8.4 min for [18F]FB-HTL, 3.5 min for [18F]pFBG, 1.1 min for

[^{18}F]FBBG and 5.9 min for [^{18}F]pFBC. Although there are substantial differences in the blood half-life, all four radiotracers showed sufficiently fast excretion from the blood pool.
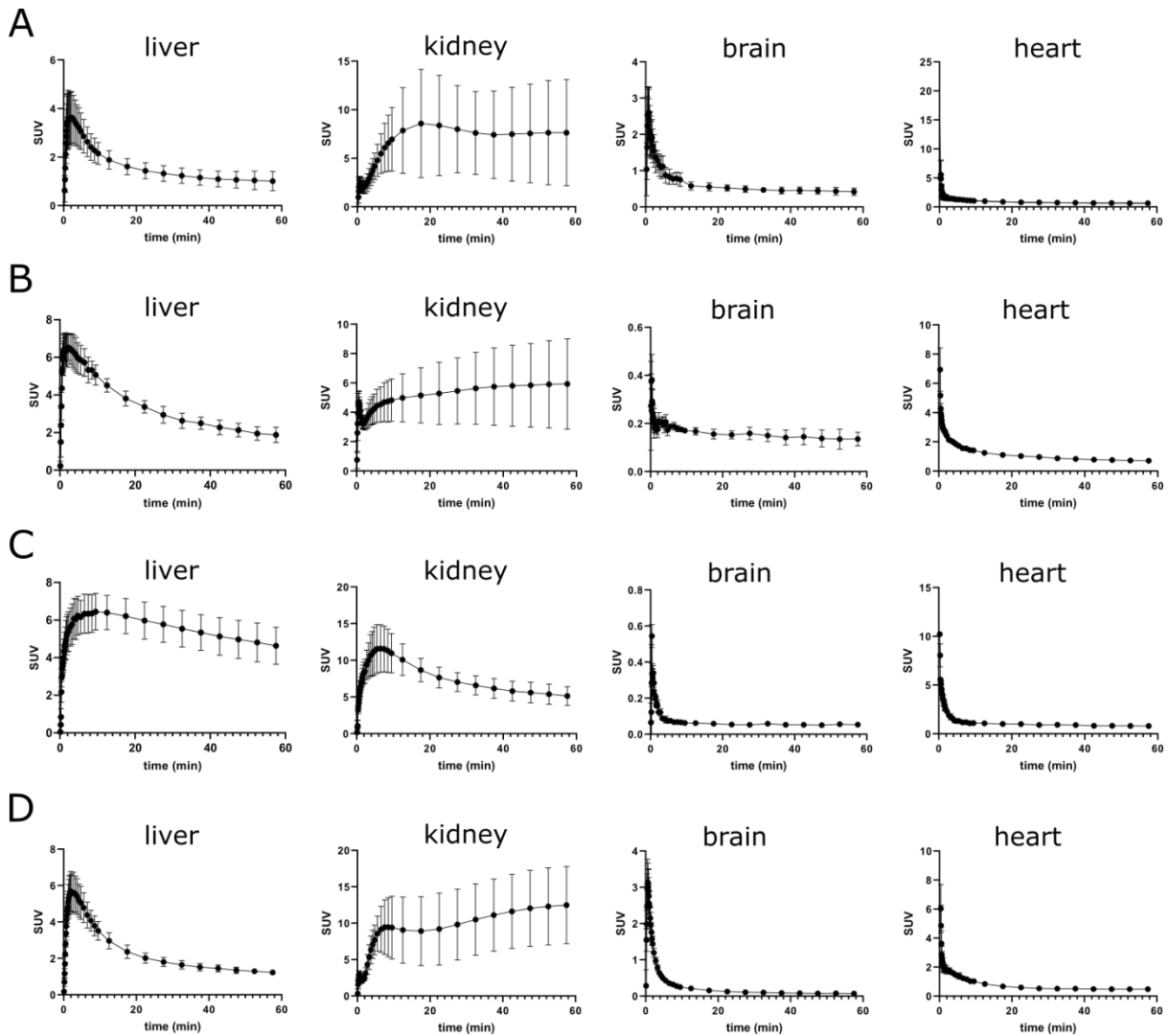
Figure 35: TACs of selected organs over a time course of 60 min p.i. A [^{18}F]FB-HTL. **B** [^{18}F]pFBG. **C** [^{18}F]FBBG. **D** [^{18}F]pFBC. Error bars represent the standard deviation of n = 5 ([^{18}F]FB-HTL) or n = 4 mice.

To verify the reporter expression in the xenografts, IF staining with an anti-myc antibody (red) was performed on paraffin-embedded xenograft slices (Figure 36). Additionally, slices were stained for proliferation (Ki67, blue), blood vessels (CD31, green) and nuclei (YO-PRO, grey) (contributions according to Chapter 8.1). Expectedly, all HEK-reporter xenografts showed good reporter expression on the cell surface of tumor cells, while no reporter expression was visible in the control xenografts. Most prominent in the HEK-Halo xenografts, but also observed in the HEK-SNAP xenografts, a loss of reporter expression towards the xenograft core was detected. Additionally, reporter expression was heterogeneous within the xenograft. This explains the observation of heterogenous radiotracer distribution in the PET data, and proves that the heterogenous reporter expression itself is the cause of this phenomenon and

not potential perfusion problems of the radiotracers. Especially for the HEK-Halo xenograft, the loss of reporter expression aligned with complete halt of proliferation, hinting towards beginning necrosis in the xenograft core due to the large tumor size.
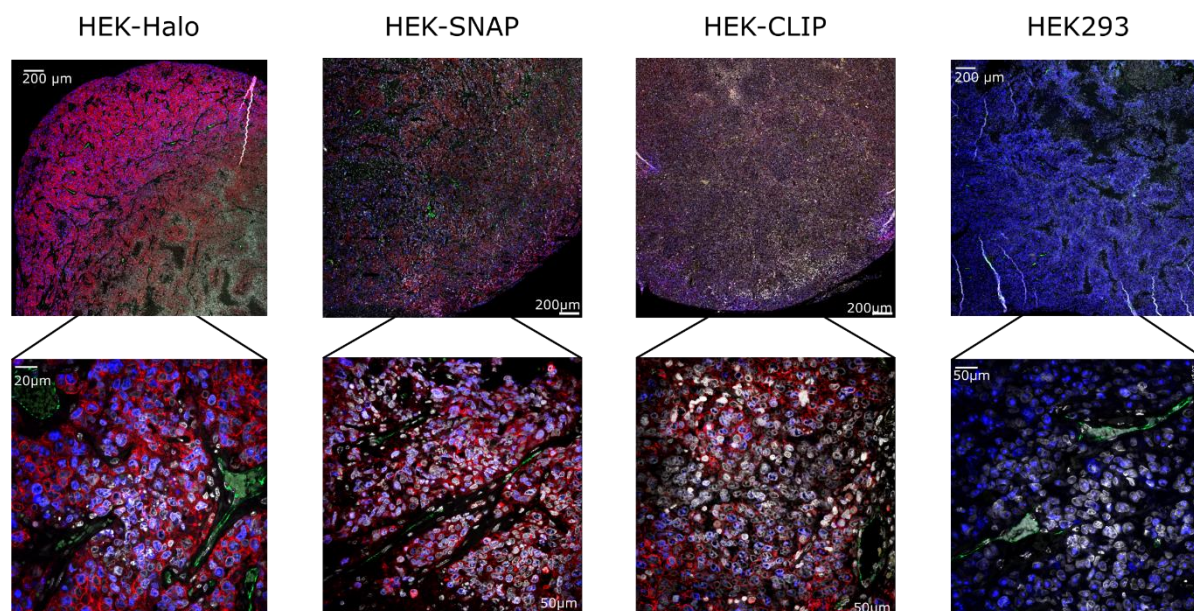
Figure 36: *Ex vivo* immunofluorescence staining of HEK-reporter and HEK293 control xenografts. Xenografts were stained for *myc*-tag expression (red), Ki67 (proliferation marker, blue), CD31 (blood vessels, green) and nuclei (grey).

In summary, all four reporter radiotracers proved their potential for RGS-PET and showed favorable pharmacokinetics and reporter-specific uptake in a HEK293-based cell model. This cell model was deemed not optimal, as the heterogenous tumor growth and radiotracer distribution influenced radiotracer performance. Here, more sophisticated models would greatly benefit the further development and applications.

[^{18}F]FB-HTL, [^{18}F]pFBG and [^{18}F]pFBC are cleared rapidly from non-target regions, and are excreted mainly renally, leading to low background uptake in the abdomen. [^{18}F]FBBG exhibited higher abdominal and liver uptake, but featured the highest target detection performance. [^{18}F]FB-HTL and [^{18}F]pFBC additionally exhibited unspecific brain uptake as verified by the biodistribution analysis and might thus serve as reporter for neurological models of disease or gene therapy. With these promising results, evaluation of those two reporter-radiotracer pairs in a neurological model to assess specific brain uptake was warranted.

4.3.3 Application of HaloTag for Neuroimaging

The results from the last section suggest that uptake of [^{18}F]FB-HTL and [^{18}F]pFBC in the brain is apparent. To explore suitability of the radiotracers for brain imaging, an *in vivo* metabolite study was carried out first to identify radiometabolites that might hamper specific targeting of the radiotracers in the brain. Despite presenting stable in serum, the complex interplay of metabolism in a living organism cannot be represented in an *in vitro* study and radiometabolites should be determined along with *in vivo* brain studies. Subsequently, an AAV carrying either the HaloTag or the CLIPTag sequence as already used for the HEK293 cell model was injected into the right striatum of female NOD.CB17-*Prkdc*^{scid} mice to induce reporter expression in the brain (**Figure 37**, n = 9). As control, all animals were sham-injected with PBS in the left striatum, and control animals were injected with an AAV carrying GFP only in the right striatum (n = 9). The PET scans were performed after 5 and 10 weeks after AAV injection to exclude any BBB leakage caused by the injection itself and to assess reporter expression longitudinally. After the second PET scan, mice were sacrificed for *ex vivo* analyses including autoradiography and light sheet microscopy.
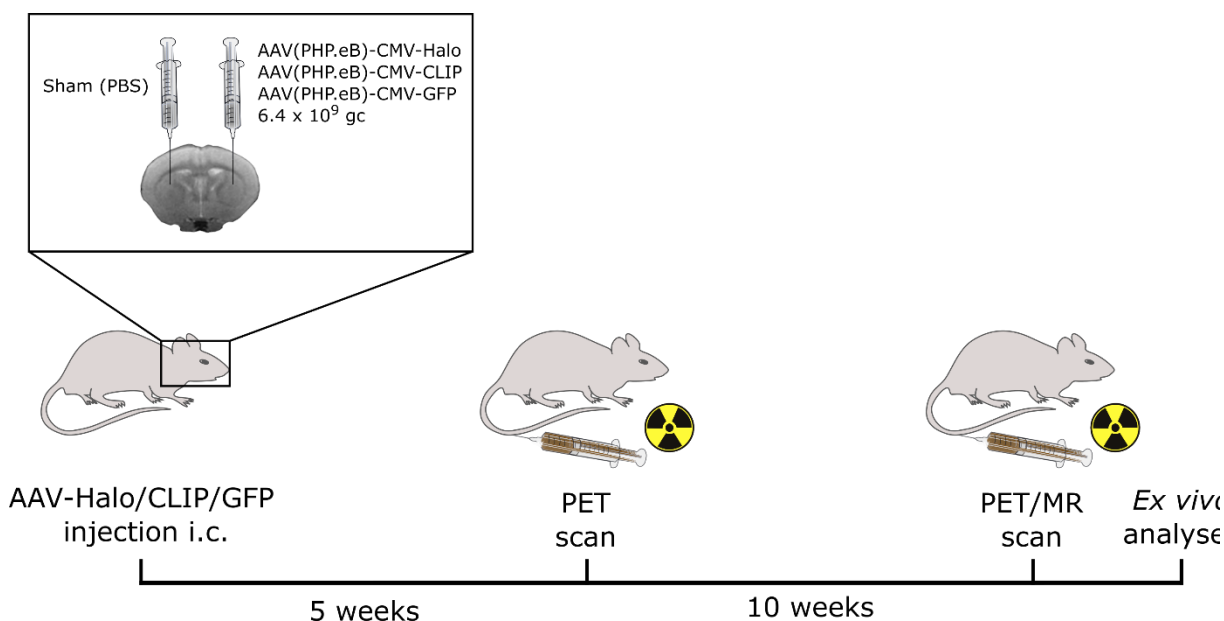
Figure 37: AAV study outline. Mice were injected with either 6.4 × 10^9 genome copies (gc) AAV(PHP.eB)-CMV-Halo or AAV(PHP.eB)-CMV-CLIP in the right striatum. The left side was sham-injected with PBS, and control animals received an AAV(PHP.eB)-CMV-GFP injection in the right striatum. After 5 and 10 weeks, PET scans were performed.

For radiometabolite analysis, naïve NOD.CB17-*Prkdc*^{scid} mice (n = 3 per time point) were injected with a high-dose bolus of radiotracer (approximately 100 MBq). After 5, 15 or 30 minutes, mice were sacrificed, blood serum and brain homogenate were collected and subjected to HPLC analysis. The area under the curve from the averaged HPLC

chromatograms was used for calculation of the percentage of intact radiotracer and radiometabolite.

[^{18}F]FB-HTL rapidly underwent liver metabolism, as indicated by 97 % of a more polar radiometabolite in the serum after only 5 minutes which further increased to over 99 % after 30 minutes (

Table **14**, Figure 38 A). The radiometabolite also reached the brain, but to an initially lower percentage (62 % after 5 minutes to over 97 % after 30 minutes). This indicates that both intact [^{18}F]FB-HTL and radiometabolite are able to cross the BBB. A proposed mechanism for [^{18}F]FB-HTL could be hydroxylation of the aromatic ring through cytochrome P450 phase I liver metabolism.[330] As the aromatic fluorobenzoyl ring is not mechanistically involved in the enzymatic reaction of the radioligand with the HaloTag, we hypothesize that the radiometabolite will not affect radiotracer uptake and might even bind to the HaloTag as well.

In contrast to [^{18}F]FB-HTL, [^{18}F]pFBC was more stable in serum and showed slower liver metabolism since 63 % of intact [^{18}F]pFBC were still present after 30 minutes. Two prominent radiometabolites were detected that were again more polar than the parent compound. However, for [^{18}F]pFBC the radiometabolites were not detectable in the brain, indicating that the radiometabolite is not able to cross the BBB (Table 15, Figure 38 B).

Table 14 Percentage of intact [^{18}F]FB-HTL and metabolite in serum and brain after 5, 15 and 30 min.

	% [^{18}F]FB-HTL	% Metabolite
Serum 5 min	3.02	96.98
Serum 15 min	0.58	99.42
Serum 30 min	0.38	99.62
Brain 5 min	37.83	62.17
Brain 15 min	5.03	94.97
Brain 30 min	2.31	97.69

Table 15: Percentage of intact [^{18}F]pFBC and metabolite in serum and brain after 5, 15 and 30 min.

	% [^{18}F]pFBC	% Metabolite
Serum 5 min	53.46	46.54
Serum 15 min	41.21	58.79
Serum 30 min	37.06	62.94
Brain 5 min	100.00	0.00
Brain 15 min	100.00	0.00
Brain 30 min	100.00	0.00
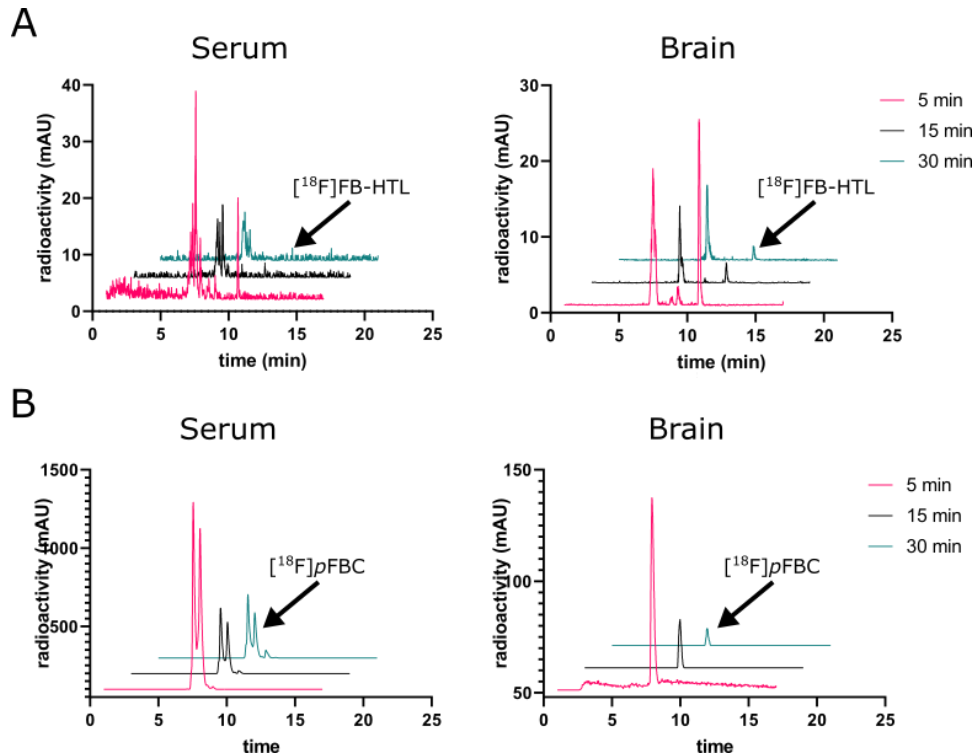
Figure 38: Chromatograms of the *in vivo* radiometabolite analysis. A [18F]FB-HTL and **B** [18F]*p*FBC. The respective peak from the intact radiotracers is marked with an arrow.

Although radiometabolites were detected for both [18F]FB-HTL and [18F]*p*FBC, we concluded that they would likely not critically interfere with radiotracer binding *in vivo*. Consequently, we moved on with the *in vivo* AAV study.

All animals survived the experimental procedures, and no neurotoxicity caused by AAV injection was observed in the behavior of the mice. The AAV-Halo injected animals showed clear evidence of accumulation of [18F]FB-HTL in the right striatum in the PET images compared to the sham-injected left striatum after both 5 and 10 weeks (Figure 39 A and B). Interestingly, it visually looked like there was more background radioactivity in the brains of AAV-GFP control animals compared to AAV-Halo inoculated animals, but this was not confirmed in the TAC analysis. It might be possible that the detected radiometabolite from the *in vivo* analysis also binds to the HaloTag in addition to intact [18F]FB-HTL and thereby contributes to the good signal.

The *in vivo* data were further supported by *ex vivo* autoradiography from striatal brain sections 10 weeks after virus inoculation, which were obtained directly after the second PET scan. Here, the strong signal in the right striatum was confirmed (Figure 39 C, n = 3 per group). Notably, for some brains, radioactive signal was not only observed in the striatum but also in the nigrostriatal pathway and the substantia nigra, highlighting the highly interconnected brain structures and the projection potential of striatal neurons into the substantia nigra.
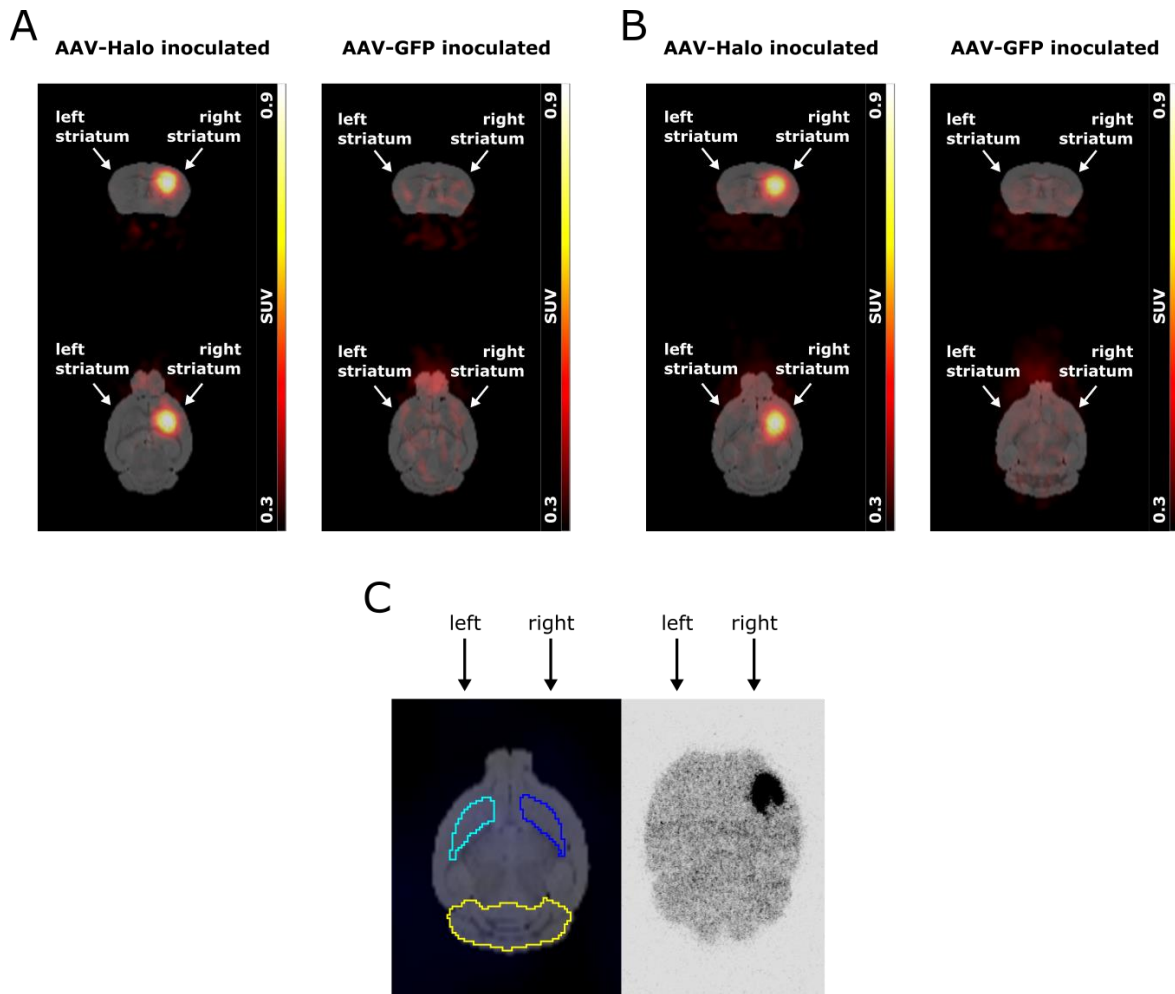
Figure 39: Representative PET images and autoradiograph of AAV-Halo inoculated animals. A Representative PET images 5 weeks after AAV inoculation. Images represent the last 10 min of a 60 min dynamic scan. **B** Representative PET images of the same mice 10 weeks after AAV inoculation. Images represent the last 10 min of a 60 min dynamic scan. **C** Autoradiograph of a striatal brain section 10 weeks after AAV inoculation. Images are co-registered to the Mirrione mouse brain atlas with the left and right striata highlighted in cyan and blue, respectively, and the cerebellum as reference region depicted in yellow.

PET scans were analyzed with the software pmod, as the PET data were co-registered to the Mirrione mouse brain atlas instead of MRI scans. The TACs showed a significant right to left (R-L) difference at both time points using whole striatum ROIs (5 weeks: p = 0.0005; 10 weeks: p = 0.0005, 2-way ANOVA) and 70 % isocontour ROIs according to the region with highest radioactivity (5 weeks: p < 0.0001; 10 weeks: p < 0.0001, 2-way ANOVA) for both 5 and 10 weeks after AAV inoculation (Figure 40 A, B: 5 weeks, D, E: 10 weeks). In contrast, no R-L difference was observed for the AAV-GFP inoculated animals (Figure 40 C: 5 weeks, F: 10 weeks, ns). The TAC data of the sham-injected left striatum showed rapid clearance from non-target tissue ($t_{1/2}$ left striatum: 60±15 s, n = 18, two phase decay fit).
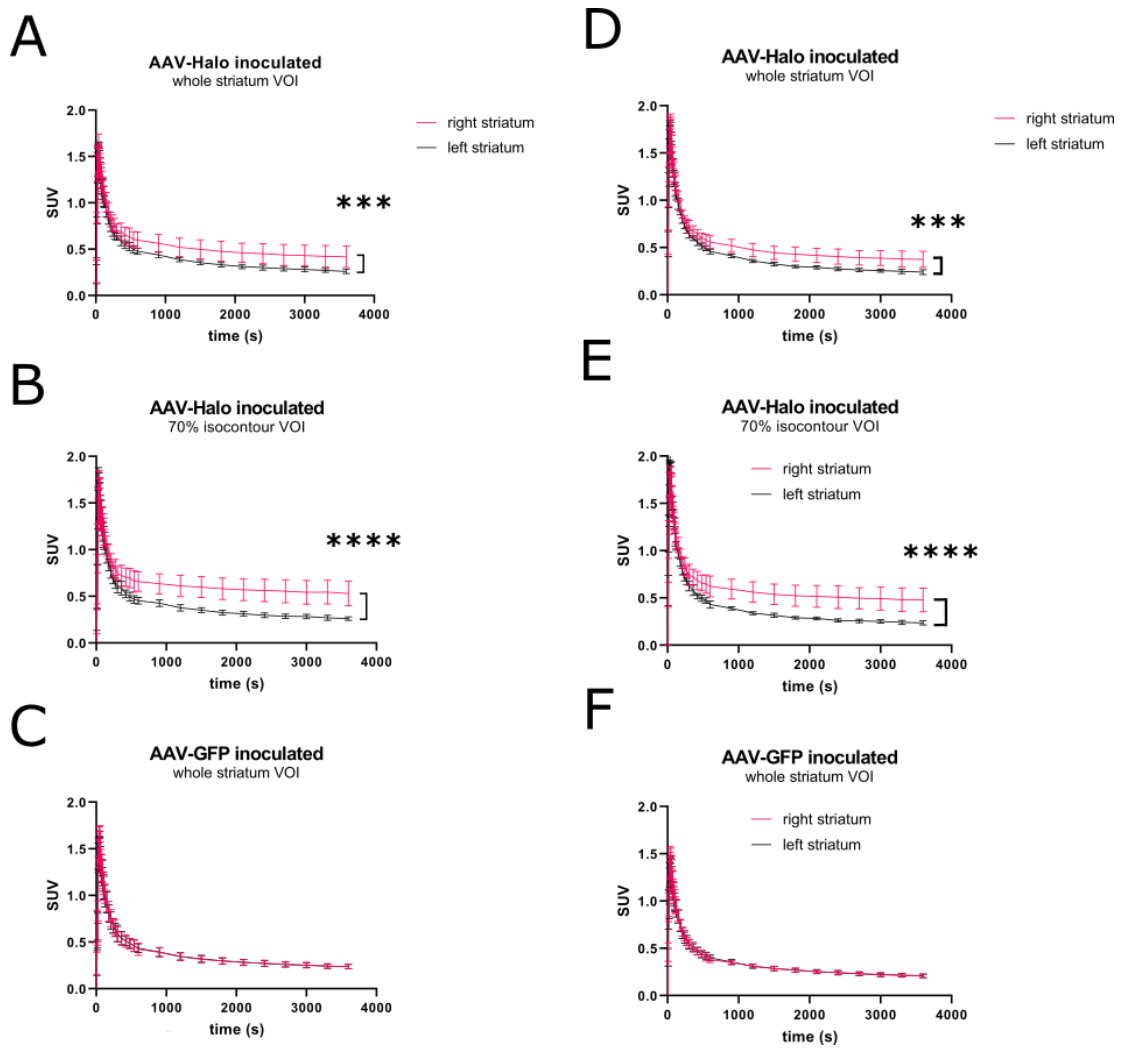
Figure 40: TACs of the right striatum (pink) compared to the left striatum (black) of AAV-Halo inoculated animals. TACs 5 weeks after virus administration using the whole striatum VOI (**A**, error bars represent the standard deviation of n = 7 mice) or a 70% isocontour VOI (**B**, n = 7) or of AAV-GFP inoculated control animals (**C**, n = 7) and 10 weeks after virus inoculation (**D-F**, n = 9).

The distribution volume ratio (DVR-1) was calculated using the cerebellum as reference region and confirmed the significant R-L differences in AAV-Halo inoculated animals (Figure 41 A-C and F-G, whole striatum ROI 5 weeks: $p = 0.0001$; 10 weeks: $p < 0.0001$; 70 % isocontour ROI 5 weeks: $p = 0.0001$; 10 weeks: $p < 0.0001$, 2-way ANOVA). Additionally, the binding potential (BP$_{ND}$) was calculated using the pmod kinetic modeling tool and the Logan reference tissue model. Although this model is not optimal for irreversible binding kinetics, the data correlated well with the ground-truth PET imaging data (in SUV, $R^2 = 0.9$, data not shown). Also here, the BP$_{ND}$ was significantly higher in the right striata of AAV-Halo inoculated animals with both whole striatum and 70 % isocontour volumes of interest (VOIs) at both time points (Figure 41 D-E and I-J, 5 weeks: $p = 0.0023$ (whole striatum ROI) and $p = 0.0002$ (70 % isocontour ROI); 10 weeks: $p = 0.0033$ (whole striatum ROI) and $p = 0.0017$ (70 % isocontour ROI), Student's t-test).

Interestingly, longitudinal changes in the PET signal were observed between the two time points, hinting towards changes in the reporter expression over time. Some animals exhibited higher uptake values after 10 weeks, while for others the uptake decreased over time. However, this could also be due to day-to-day fluctuation in the reporter expression or differences in daily radiotracer quality and requires further *ex vivo* validation.
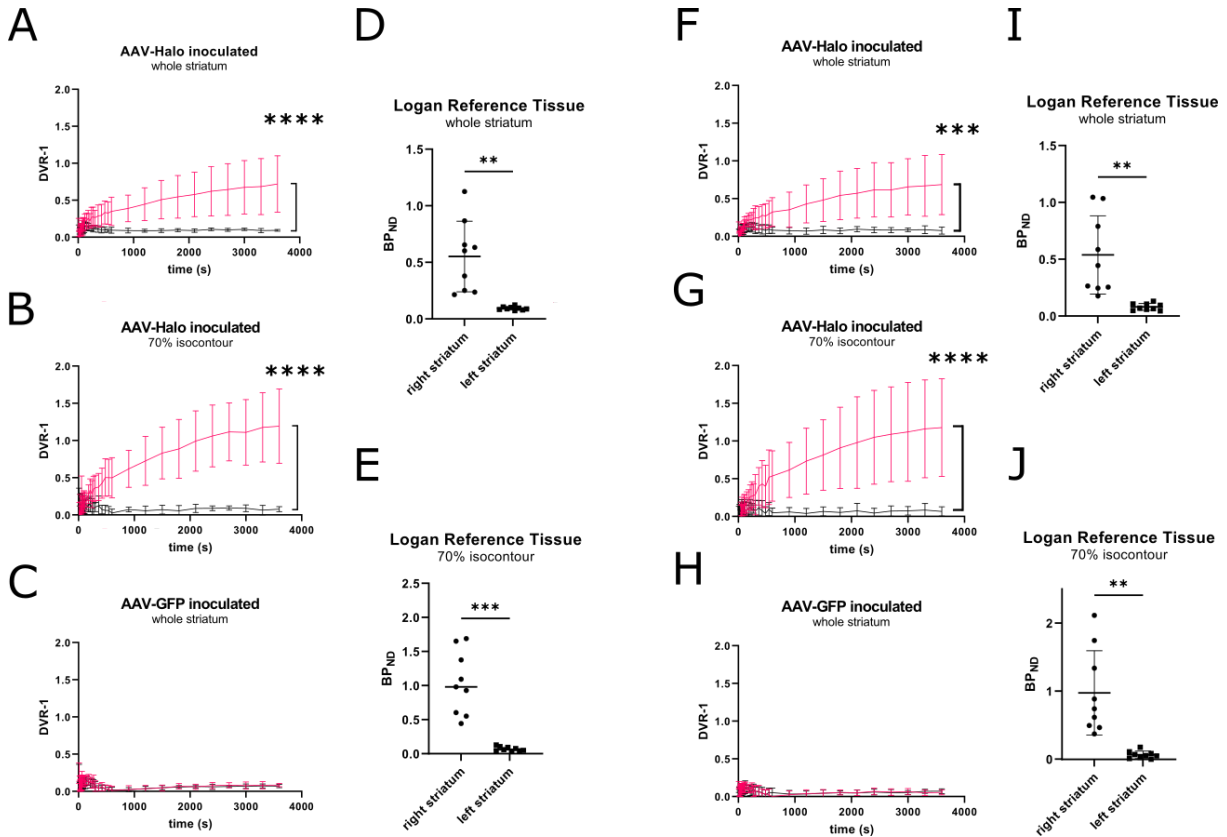
Figure 41: DVR-1 values of the right striatum (pink) compared to the left striatum (black) of AAV-Halo inoculated animals. DVR-1 values 5 weeks after AAV-Halo administration using the whole striatum VOI (**A**, error bars represent the standard deviation of n = 9 mice) or a 70% isocontour VOI (**B**, n = 9) or of AAV-GFP inoculated animals (**C**, n = 9) and the calculated BP_{ND} using the Logan reference tissue model (**D-E**, n = 9). Similarly, the DVR-1 values 10 weeks after AAV-Halo inoculation using the whole striatum VOI (**F**, n = 9) or a 70% isocontour VOI (**G**, n = 9) or of AAV-GFP inoculated animals (**H**, n = 9) and the calculated BP_{ND} using the Logan reference tissue model (**I-J**, n = 9).

Thus, the remaining brains from the animals not subjected to autoradiography were removed after vessel staining with Evans Blue and wheat germ agglutinin (WGA) and subjected to light sheet microscopy (n=4). HaloTag expression was detected using an anti-HaloTag antibody and quantified using the fluorescence signal obtained from light sheet microscopy. We indeed observed differences between the four brains in both the PET and light sheet microscopy data (Figure 42 A-B). However, these differences did not correlate between the modalities (Figure 42 C). While the PET signal is crisp and precisely localized, the light sheet microscopy images occur more diffuse. Additionally, high surface signal was apparent,

indicating incomplete penetration of the antibody. Thus, the light sheet microscopy images might not quantitatively represent the total expression levels without additional optimization of the protocol.
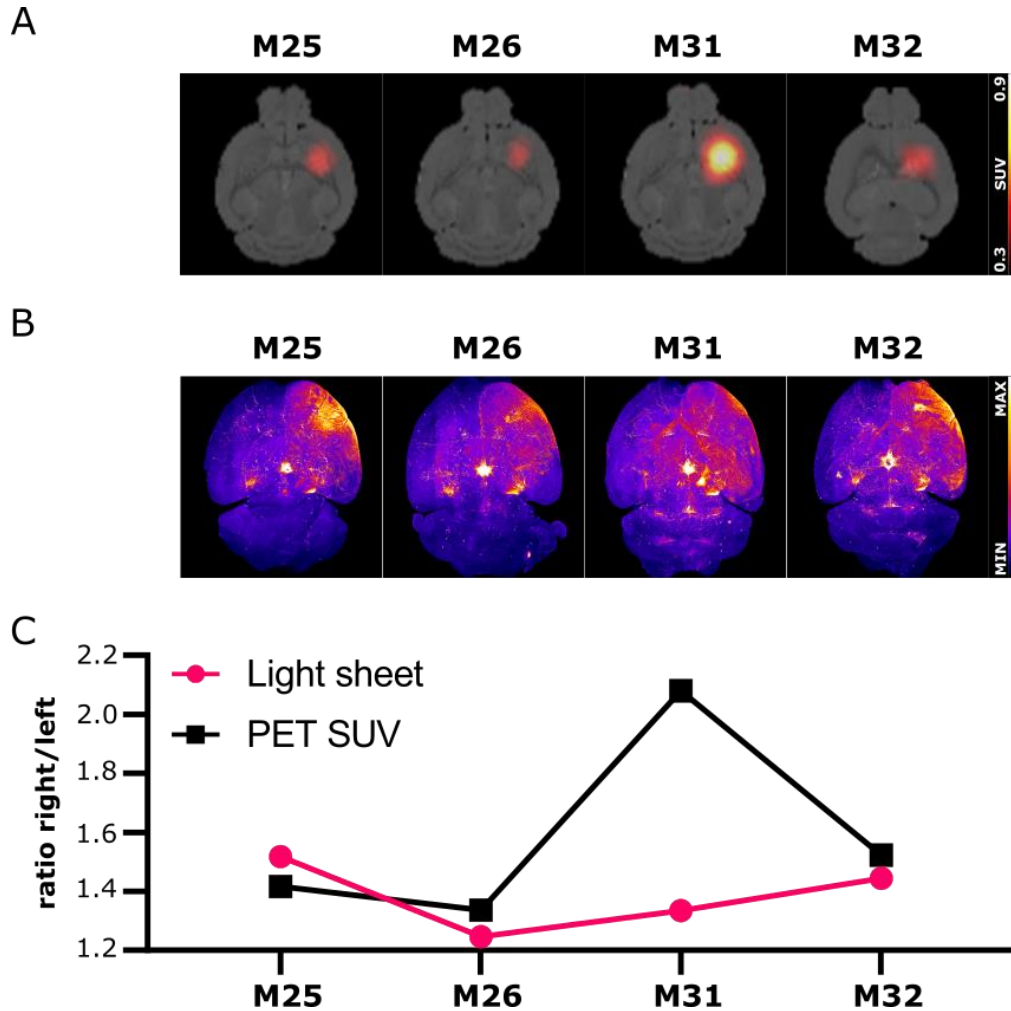
Figure 42: Comparison between light sheet microscopy quantification and PET SUVs. A PET images of four AAV-Halo inoculated brains. Images represent slices of the last 10 min of a 1 h dynamic PET scan. **B** Maximum intensity projections of the light sheet images of the same four brains stained with an anti-HaloTag antibody. **C** Comparison of the ratios between the right and the left striata of PET SUV and light sheet maximum intensity for n = 4 brains.

4.3.4 Application of CLIPTag for Neuroimaging

The same experimental procedure was performed for [^{18}F]pFBC. Here, we did not observe any signal in the PET images at both time points (**Figure 43** A and B). However, the autoradiograph of the striatal region clearly showed increased radioactivity in the right striatum in comparison to the left striatum (**Figure 43** C), Since we already suspected rapid efflux of [^{18}F]pFBC from brain tissue, we expected [^{18}F]pFBC uptake to be not as prominent as for [^{18}F]FB-HTL. We thus hypothesize that the lack of PET signal is due to rapid washout

from brain tissue, supposedly mediated by PgP. An additional factor is the size of the ROI, which is much smaller compared to [^{18}F]FB-HTL. As spatial resolution of PET is limited physically due to detector crystal size, positron range, and 3D image sampling, the partial volume effect might hamper detection of smaller lesions.[331] Furthermore, autoradiography is more sensitive than PET imaging due to longer exposure time and can resolve smaller lesions.
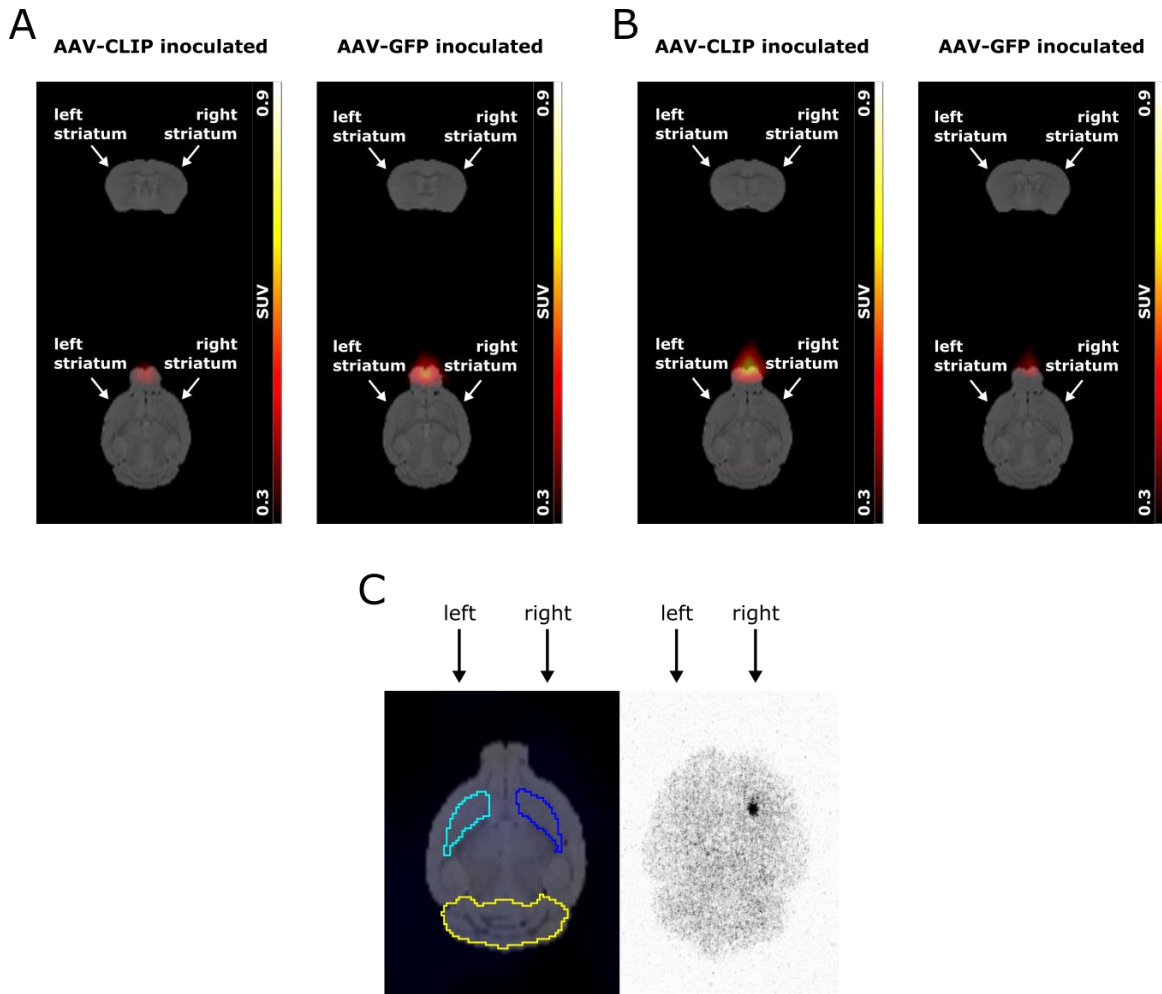
Figure 43: Representative PET images and autoradiograph of AAV-CLIP inoculated animals. A Representative PET images 5 weeks after AAV inoculation. Images represent the last 10 min of a 60 min dynamic scan. **B** Representative PET images 10 weeks after AAV inoculation. Images represent the last 10 min of a 60 min dynamic scan. **C** Autoradiograph of a striatal brain section 10 weeks after AAV inoculation. Images are co-registered to the Mirrione mouse brain atlas with the left and right striata highlighted in cyan and blue, respectively, and the cerebellum as reference region depicted in yellow.

The lack of R-L difference for AAV-CLIP inoculated animals was also evident in the TACs and the calculated DVR-1 at both time points, where no difference to AAV-GFP inoculated animals was observed (Figure 44 A-D AAV-CLIP inoculated animals, E-H AAV-GFP inoculated animals).
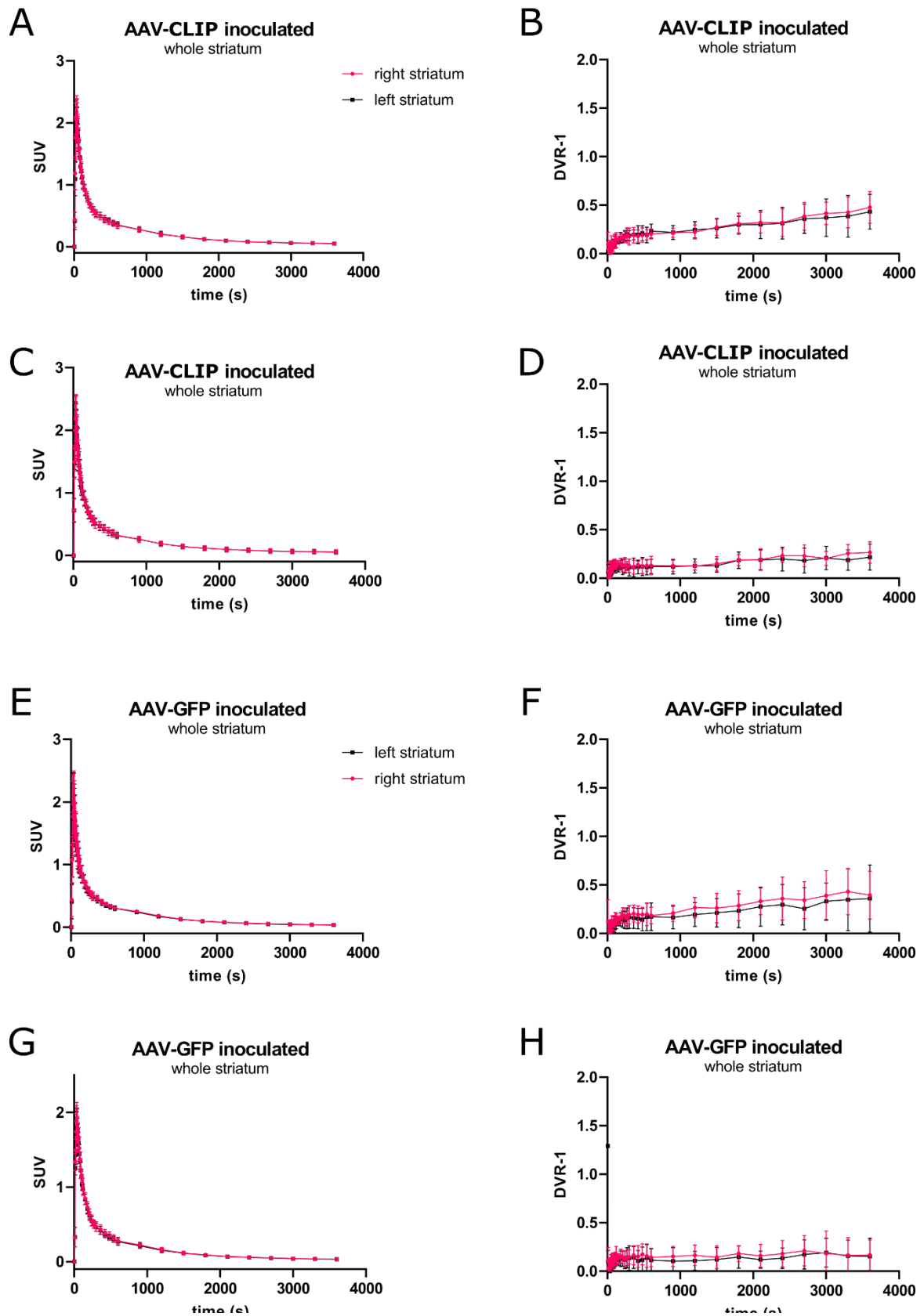
Figure 44: TACs and DVR-1 of the right striatum (pink) compared to the left striatum (black) of AAV-CLIP inoculated animals. TACs and DVR-1 of AAV-CLIP inoculated animals 5 weeks (**A-B**, n = 9) and 10 weeks (**C-D**, n = 9) after virus administration and of AAV-GFP inoculated animals (**E-F** 5 weeks, **G-H** 10 weeks, n = 9).

To verify whether we induced sufficient CLIPTag expression in the striatum, we again performed light sheet microscopy with the remaining brains (n = 6) and an anti-CLIPTag antibody. CLIPTag expression was clearly visible in the neurons of the right striatum, confirming the autoradiography images (Figure 45).

Figure 45: Representative light sheet images from a CLIP brain. A Overview image of the CLIPTag brain with visible blood vessels (Evans Blue, red), nuclei (green) and autofluorescence (blue) **B** Zoom-in of the striatal brain region of the same brain with visible CLIPTag signal (orange, indicated with a white arrow), nuclei (green) and autofluorescence (blue)**. C** Further zoom-in of a representative brain with CLIPTag signal (orange) visualizing the neurons and nuclei (blue).

Although [^{18}F]FB-HTL is metabolized quickly *in vivo*, sufficient radiotracer accumulation for visible detection of transduced areas was observed in the PET images. This supports our hypothesis of the metabolic route of [^{18}F]FB-HTL, oxidation of the fluorobenzoate, and that this modification is not critical for binding to the HaloTag. It could be possible that the metabolite is able to bind to the HaloTag as well. Since the metabolite is retained in the brain, it might cause the further increase in radioactive signal.

In contrast, [^{18}F]*p*FBC is not metabolized and the molecule seems to be more actively pumped out of the brain, which might be the reason that we do not see any increase in PET signal but detectable uptake in the more sensitive autoradiograph. The most obvious candidate transporter for this is PgP due to its large substrate range.[332] This could be assessed in future studies by PgP inhibition during PET imaging to determine whether this phenomenon persists.

Concluding, we successfully characterized the two reporter-radiotracer pairs HaloTag with [^{18}F]FB-HTL and CLIPTag with [^{18}F]*p*FBC in an *in vivo* study of AAV-mediated gene transfer in the brain. Despite some room for further improvements that need to be addressed in the future, like improving the metabolic stability of [^{18}F]FB-HTL and increasing the brain retention of [^{18}F]*p*FBC, both RGS work very well and are suitable for further development and second-generation radiotracers. Although initially designed as preclinical RGS, in particular CLIPTag bears translation potential into clinical applications of gene or cell transfer. The reporter protein is small, and, since its derived from human AGT, not likely to be immunogenic.

Overall, all three RGS bear great potential for future application. Although the SNAPTag radiotracers do not cross the BBB as of now, further development might improve BBB penetration. Additionally, chemical modification of [^{18}F]pFBG could prevent defluorination of the radiotracer. So far, SNAPTag and [^{18}F]FBBG feature the most favorable subcutaneous xenograft uptake, rendering is most suitable for applications outside of the brain.

The reporter genes developed within this thesis have proven their versatility and preclinical merit in both a xenograft model and a model of viral gene transfer to the brain. They could be used to assess biological processes or responses for which no specific imaging biomarker is yet available. One such example could be replicative stress. Currently, the analysis of responses to therapies targeting replicative stress is limited to *in vitro* experiments, which might not adequately predict the *in vivo* response. A potential *in vivo* model could comprise one of our RGS and a suitable readout, for example a specific promotor, and as such aid the further development of these promising therapies.

5. CONCLUSION

Targeting replicative stress for cancer therapy is a highly promising concept for personalized medicine. PET imaging of replicative stress would facilitate the development of novel therapeutics and the stratification of patients. In this work, we investigated PARP enzymes for their potential as biomarkers for replicative stress, aimed to identify novel biomarkers, and evaluated an alternative quantification method for validation of animal models using reporter genes.

We established the radiosynthesis of three literature-known PARP radiotracers and designed and synthesized two novel variants. The five PARP radiotracers were then compared in a head-to-head *in vivo* mouse study to determine the best applications. In parallel, we characterized different cellular models of replicative stress and checked for correlation of replicative stress levels with PARP radiotracer uptake. We found no evidence of this correlation, so we set out to identify novel, more specific biomarkers, using Western blot.

As an alternative, we chose to take a different route to quantify replicative stress with the use of reporter genes. We successfully established three novel nuclear RGS and proved specific uptake in a xenograft model. Two of them are suitable for whole-body use, which is important for unrestricted application possibilities, as shown in a murine model of viral gene transfer to the brain.

5.1 The Future of PARP

It is evident that PARP plays an important role in tumor development and progression. The multitude of clinically approved PARP inhibitors and the ongoing further development of novel drugs underline the great clinical interest. Just recently, a novel PARP inhibitor, pamiparib, was approved in China, featuring similar inhibitory potential as talazoparib and high specificity for PARP1/2.[333,334]

Consequently, the use of radiolabeled PARP inhibitors for PET imaging has emerged, as both a valuable tumor diagnostic and as a potential prognostic marker for progression-free survival.[335] Clinical translation of the gold-standard PARP radiotracers [^{18}F]PARPi (phase I) and [^{18}F]FTT (phase I) is underway. However, the development of novel PARP radiotracers is warranted by the high clinical interest and limitations of the current ones, for example high liver uptake for [^{18}F]PARPi, hampering its use for liver metastasis.

Our alternative to [^{18}F]PARPi is [^{18}F]FPyPARP, a logD-optimized variant with an improved pharmacokinetic profile. By replacing the fluorobenzoic acid with a fluoronicotinic acid, we were indeed able to shift the excretion route towards more renal clearance in comparison to [^{18}F]PARPi, although only to a minor degree. In a mouse xenograft model, PARP1 targeting was comparable between [^{18}F]PARPi, [^{18}F]FPyPARP and [^{18}F]FTT. Interestingly, [^{18}F]PARPi

showed already 30 % renal clearance in humans, indicating that [^{18}F]FPyPARP might be even more suitable for liver tumors and metastases in humans.

Another milestone within this work was the disclosure of the automated radiosynthesis of [^{18}F]talazoparib. Talazoparib is considered the 'next-generation' PARP inhibitor, since it has a 100-fold higher efficacy than the first approved PARP inhibitor olaparib. This is attributed to its drastically higher trapping capacity of PARP1 to the DNA, increasing single agent cytotoxicity.[336] To investigate how the improved trapping capacity influences PET imaging performance, we compared [^{18}F]talazoparib to [^{18}F]olaparib in the same mouse model. We were not able to detect notable differences in the pharmacokinetics of both radiotracers, and the xenograft uptake was in the same range. Thus, the PARP trapping ability seems not to influence [^{18}F]talazoparib performance and we found no evidence for an advantage in using [^{18}F]talazoparib over [^{18}F]olaparib regarding tumor delineation.

However, since the molecular mechanism and subtype specificity differs, [^{18}F]talazoparib could be suitable for additional scientific questions compared to other PARP radiotracers. Exemplarily, TNKS are PARPs that are not necessarily involved in replicative stress, but are important regulators of the Wnt pathway, a driver in tumorigenesis.[337] Despite developed to be selective for PARP1/2, some of the PARP inhibitors show a certain affinity towards TNKS1/2.[338] Talazoparib shows good inhibitory activity towards TNKS2 in the nanomolar range, thus, we hypothesize that some of the signal from [^{18}F]talazoparib might be attributed to binding to TNKS2. Specific TNKS signal could be determined indirectly by blocking PARP1/2-specific uptake with the more selective olaparib, but would require a high dose of PARP1/2 inhibitor. Alternatively, XAV939, a TNKS-specific inhibitor, showed good antitumor activity in neuroblastoma cells, and the chemical structure would allow radiolabeling towards a TNKS-specific radiotracer.[339] Since radiotracer development can be a time-consuming challenge, the use of [^{18}F]talazoparib might be a work-around for first *in vivo* evaluation of TNKS PET imaging if the signal can be separated from PARP1/2.

In the head-to-head comparison of all five PARP radiotracers, we observed significant differences in radiotracer accumulation in some organs, in particular the excreting organs. We conclude that the choice of PARP radiotracer for a specific purpose is dependent on the tissue of interest and the choice of reference tissue. In general, all PARP radiotracers present with high liver uptake, still hampering their potential use for liver cancer. Careful further modification of the molecules or development of novel radiotracers might result in the desired low liver background. Also, human metabolism is different from rodents, so preclinical PARP radiotracers with high liver signal in rodent models could nevertheless be suitable for clinical liver imaging. Currently however, clinical applications are limited as only [^{18}F]PARPi and [^{18}F]FTT have entered clinical trials and the approval process for human application of novel radiotracers is time- and resource-intensive.

For PARP radiotracers, brain penetration is important to effectively delineate brain tumors from healthy brain tissue in patients with intact BBB. PARP inhibitors, the basis for PARP radiotracers, are generally known to be PgP substrates, which is in line with our observation of no or very low brain uptake for most PARP radiotracers.[340] In contrast, the novel inhibitor pamiparib is reportedly no substrate of PgP, rendering it an interesting target for radiolabeling.[341] In summary, the development of novel PARP radiotracers with improved pharmacokinetic profile is warranted and ongoing.

5.2 Targeting the Tumor Stress Response for Theranostics

Targeting tumor stress is clearly not a trivial task, as the replicative stress response is complex and highly intertwined with other biological pathways. We evaluated PARP for its potential as a biomarker for replicative stress as PARP is heavily involved in DNA repair and considered a guardian of the genome. Although PARP seems to be commonly upregulated in cancers, which underlines its importance as tumor biomarker, a short-term upregulation in response to replicative stress could not be observed in any of our different cell models. We suspect that, since PARylation of target proteins is a very fast process and DNA SSB occurrence is frequent, PARP is not upregulated but activated upon replicative stress.[342,343] Cells with DNA damage need a fast repair mechanism, which can only be achieved by activation of already present PARP as a 'first responder'. With PARP radiotracers, it is only possible to quantify absolute PARP enzyme levels but not their activity or their intracellular recruitment to DNA lesions or stalled replication forks.

The potential for PARP as a biomarker for chronic replicative stress is even more challenging, as chronically increased stress in tumor cells goes hand-in-hand with a plethora of other increased molecular mechanisms, amongst others transcription, translation, proliferation, or changes in metabolism. In consequence, specific and isolated quantification of chronic replicative stress only seems nearly impossible.

The currently literature-known specific biomarkers for replicative stress are unfortunately not translatable to non-invasive *in vivo* imaging so far. In some cases, the method itself would be invasive, for example the DNA fiber assay. The biomarkers pRPA2, pCHK1, or γH2AX are biomarkers that detect protein activation status, which are great for *in vitro* assays but PET imaging of protein activation is not directly possible.

Protein activation is largely based on site-specific phosphorylation of the proteins. Antibodies can distinguish between phosphorylated and non-phosphorylated protein, but they are not able to cross the plasma membrane. As replicative stress is an intracellular process, radiolabeled antibodies are not suitable for quantification of PARP activity or other parts of the replicative stress signaling cascade.

Our attempts to identify more specific biomarkers for replicative stress with Western blots did not result in a clear biomarker. Most of the investigated protein levels were similar under mild acute replicative stress conditions. This again underlines that most of the replicative stress response is based on protein activation and not on upregulation, for example for ATM, which is nevertheless a promising target for replicative stress.[163]

Besides PARP-related radiotracers, other proteins of the replicative stress response are targeted by PET radiotracers: [^{18}F]ATRi, a radiolabeled analogue of the ATR inhibitor Ve-821, has proven feasibility of ATR-imaging in an *in vivo* xenograft study in mice.[344] However, this radiotracer suffered from high blood retention and was not tested for its correlation with replicative stress. Similarly, a ^{11}C-labeled ATM inhibitor (AZD1390) that assesses brain penetration in primates and humans to predict the therapeutic dosage of said inhibitor has been synthesized.[345,346] Although brain penetration was reported, the literature did not provide any further information on the biodistribution of [^{11}C]AZD1390 in other organs.

For optical imaging techniques, it is possible to directly assess protein activity, for example with activatable probes resulting in conformational changes that lead to Foerster or bioluminescence resonance energy transfer.[166] Due to the highly complex nature of replicative stress, combination biomarkers for multiple targets could shed light on proteins upregulated during replicative stress. Also, as they inhibit multiple pathways, the combination could result in a detectable difference through combination of slight specific increases in different protein levels. Focus on single proteins requires the difference in expression of this protein to be solely sufficient for PET detection.

Roberts et al hypothesize that ATM activity could be indirectly measured by assessing dCK activation utilizing 1-(2′-deoxy-2′-[^{18}F]fluoroarabinofuranosyl) cytosine ([^{18}F]FAC) as radiotracer.[166,347] It has been shown that [^{18}F]FAC tumor uptake, and thus dCK activity, was significantly enhanced upon ATM activation by irradiation, a common source of replicative stress and DSBs.[348] Although [^{18}F]FAC itself has only poor specificity in humans and is metabolized quickly, a highly specific and clinically translatable probe has been already developed (2-chloro-2′-deoxy-2′-fluoro-9-β-d-arabinofuranosyl-adenine (CFA)) which visualized dCK in humans.[349] The current main application of [^{18}F]FAC is the visualization of immune cell infiltrates in liver and brain, where the deoxyribonucleoside salvage pathway is upregulated as well, which might interfere with specific imaging of replicative stress.[350-352] However, those cells are highly proliferating and part of the signal might come from replicative stress. It has been shown that [^{18}F]FAC uptake is higher in irradiated tumors, pointing towards an increase upon DSB occurrence in addition to inflammatory procceses.[348] Also, [^{18}F]FAC accumulation was high in lymphoid organs and bone marrow, which could indicate uptake in organs with high levels of proliferating cells like immune cells.[350] The structurally similar drug gemcitabine is a known inhibitor of DNA synthesis, and

exacerbates replicative stress in ovarian cancer.[353,354] All this supports a potential correlation between [^{18}F]FAC uptake and replicative stress and should be considered in future studies.

Another reason for elevated [^{18}F]FAC uptake beside replicative stress could be increased transcription and translation and the subsequent increased need for nucleosides. Targeting global translation could indeed be another way to quantify replicative stress, as translation is intertwined with replicative stress responses.[355] This might have been also the reason for the distinct increase of PARP expression in the PDAC cell model with high replicative stress. Radiolabeled amino acids have been used in an attempt to quantify translation, but they follow complex metabolic routes and are thus not suitable. More recently, puromycin, a molecule mimicking tRNA, has been radiolabeled with ^{18}F used for this purpose, but has not been fully evaluated so far.[356] Nevertheless, translation needs to be kept in mind when dealing with replicative stress, both as a potential hindrance and as a way to indirectly quantify stress.

Besides translation, there are several indirect ways to bypass the direct detection of protein activation, from the use of reporter genes to targets from related pathways that are indirectly upregulated. As mentioned, replicative stress is highly intertwined with the DDR and other stress pathways. Thus, an alternative would be the indirect imaging of replicative stress by specific marker of other pathways like the DDR, or other stress responses like ER stress.

In particular the ER stress pathway seems to offer some promisingly specific targets. The three branches of ER stress involve the activation of transcription factors, whose promotor might be targetable by reporter gene expression. Additionally, inhibitors with good affinity are available for some ER stress-related proteins, for example for ATF6.[87] Proteins that are expressed upon activation of ER stress-specific transcription factors are also interesting targets. As in this case the actual expression of the proteins is increased, PET quantification would be possible.

Finding a biomarker for replicative stress has proven to be a challenging task. Taking the data presented in this work into account, there is so far no evidence that PARP is a biomarker for replicative stress. There are other promising targets that we evaluated by Western blot, but so far, none of it has been specific. It might well be that replicative stress cannot be characterized by one specific biomarker with PET, as the molecular response is relatively fast, and proteins involved are rather activated than upregulated.

Despite not being suitable as a biomarker, PARP is a promising target for anticancer therapy related to stress. PARP inhibitors are known to increase the replication fork speed and thus replicative stress levels.[108] This could be exploited when stratifying patients for tumor stress levels with a future specific biomarker, as PARP inhibitors might be more effective in tumors with high stress.

5.3 (Pre-)Clinical Relevance of Nuclear Reporter Systems

Since the use of reporter genes is a potential bypass to quantify replicative stress, the development of an RGS that is not limited to the periphery but can also be applied in the brain is warranted. There are only few suitable nuclear brain RGS, as most available RGS are based on endogenously expressed proteins or their radiotracers have no brain penetration. We therefore successfully developed two universal RGS based on HaloTag and on CLIPTag that do not have these shortcomings.

Reporter genes can be expressed under the control of disease-relevant promotors to study promotor activation under physiological and pathological conditions. In the context of replicative stress, promotors downstream of the DNA damage response proteins ATM/ATR might be used to express imaging reporter genes. Thus, they could quantify the response to DNA damaging agents or treatments exacerbating replicative stress in the whole body without the requirement to develop a novel stress-dedicated radiotracer. This could yield important information on effectiveness of the stress targeting agents and on potential sites of treatment-related toxicities induced by stress. Stress-inducing therapies are expected to play an important role in future cancer treatment and precision medicine, exploiting the vulnerability of cancer cells by increased cellular stress.[138]

The use of our novel RGS is not limited to stress-related application, but would also greatly benefit neurobiological research. In models of virus-mediated gene transfer or knockdown in the brain, reporter gene imaging could help assess successful viral transfection, thereby improving reliability of the collected data. Such applications would be of great interest not only for methodological research but also for models of neurological diseases or gene therapy.

Gene therapy was developed as a treatment option for patients suffering from inborn genetic defects in vital genes. Here, mainly viral vectors are used due to their better transfection efficacy in comparison to non-viral vectors.[357] Today, there is a broad range of gene therapeutics for various diseases, in addition oncolytic viruses for cancer therapy, cell therapy products for immunotherapy, and mRNA vaccines.[358,359] Gene therapies using AAVs as vectors are under investigation in clinical trials. A huge challenge here is gene delivery to the CNS.[360] A nuclear RGS suitable for brain imaging would aid to verify successful CNS gene delivery and expression, and could accelerate the strategy shift to alternative treatments in the case of unsuccessful transfer.

Improvement of viral vectors is another pillar of gene therapeutic research and application. For example, brain penetration of AAVs is dependent on the administration route.[361] A RGS could aid evaluation of novel AAV serotypes by visualizing their expression kinetics, distribution and expression persistence longitudinally throughout the whole body. Similarly,

CONCLUSION

this could be applied to for example visualization of the migration of dendritic cells to lymph nodes or mRNA vaccines to shed light on their biodistribution and translation efficacy.

For potential clinical applications of the RGS, immunogenicity is a factor to be kept in mind. HaloTag is derived from a bacterial enzyme, thus will likely be immunogenic in humans. That would limit its application to one-time use or to preclinical studies only. As SNAPTag and CLIPTag are based on human AGT, they are expected to elicit only very mild immune responses and thus in principle both be used in humans. However, the original protein exhibits several mutations and is optimized for fast kinetics and substrate preferences, still bearing the potential to cause immune reactions. This needs to be addressed before potential clinical translation.

Careful modification of the SNAPTag radiotracers should be applied before further development. The stability of [^{18}F]pFBG should be improved, and chemical changes could aim for to improved BBB penetrations. Further use of the SNAPTag RGS is undoubtedly warranted, as it featured the best performance in the xenograft model. Additionally, the SNAPTag radiotracers in particular need to be evaluated for their potential to target to the original human AGT enzyme. As no elevated background binding was observed in the HEK293 cell model, which is based on human kidney cells and should express normal levels of AGT, we are positive that the SNAPTag and AGT do not interfere with each other.

RGS are versatile tools for various purposes. Further applications can include the non-invasive tracking of cells, for example immune cells in immunotherapy. As CAR T cells are an emerging topic for the treatment of non-solid tumors, following their fate can help assessing therapy efficacy. Also, CAR T cell tracking could elucidate the mechanisms behind the limited efficacy in solid tumors and aid evaluating methods to improve tumor homing and penetration.

Tumor stress imaging would greatly benefit from RGS. The reporter can be inserted under a specific promotor or co-expressed with a protein of interest, respectively, to assess promotor activity and protein expression levels. Genetically modified mice that express a reporter can, under specific circumstances, serve as models to determine whether drugs or treatments increase replicative stress. Certainly, our RGS will play an important role in neurobiological and cancer research.

6. REFERENCES

1. Hanahan, D.; Weinberg, R. A., Hallmarks of cancer: the next generation. *Cell* **2011,** *144* (5), 646-74.

2. Ozaki, T.; Nakagawara, A., Role of p53 in cell death and human cancers. *Cancers (Basel)* **2011,** *3* (1), 994-1013.

3. Hanahan, D.; Weinberg, R. A., The hallmarks of cancer. *Cell* **2000,** *100* (1), 57-70.

4. Fouad, Y. A.; Aanei, C., Revisiting the hallmarks of cancer. *Am J Cancer Res* **2017,** *7* (5), 1016-36.

5. Witsch, E., et al., Roles for growth factors in cancer progression. *Physiology (Bethesda)* **2010,** *25* (2), 85-101.

6. Connolly, E. C., et al., Complexities of TGF-β targeted cancer therapy. *Int J Biol Sci* **2012,** *8* (7), 964-78.

7. Colak, S.; Ten Dijke, P., Targeting TGF-β Signaling in Cancer. *Trends Cancer* **2017,** *3* (1), 56-71.

8. Wang, K., et al., C-erbB-2 expression is related with pathological progression of gastric cancer: results of a non-radioactive in situ hybridization. *Int J Clin Exp Pathol* **2017,** *10* (9), 9649-53.

9. Wang, Z., ErbB receptors and cancer. *Methods Mol Biol* **2017,** *1652*, 3-35.

10. Oh, D. Y.; Bang, Y. J., HER2-targeted therapies - a role beyond breast cancer. *Nat Rev Clin Oncol* **2020,** *17* (1), 33-48.

11. Goutsouliak, K., et al., Towards personalized treatment for early stage HER2-positive breast cancer. *Nat Rev Clin Oncol* **2020,** *17* (4), 233-50.

12. Timar, J.; Kashofer, K., Molecular epidemiology and diagnostics of KRAS mutations in human cancer. *Cancer Metastasis Rev* **2020,** *39* (4), 1029-38.

13. Fang, B., RAS signaling and anti-RAS therapy: lessons learned from genetically engineered mouse models, human cancer cells, and patient-related studies. *Acta Biochim Biophys Sin (Shanghai)* **2016,** *48* (1), 27-38.

14. Hong, D. S., et al., KRAS(G12C) inhibition with sotorasib in advanced solid tumors. *N Engl J Med* **2020,** *383* (13), 1207-17.

15. Bahrami, A., et al., Targeting RAS signaling pathway as a potential therapeutic target in the treatment of colorectal cancer. *J Cell Physiol* **2018,** *233* (3), 2058-66.

16. Murray, A., Cell cycle checkpoints. *Curr Opin Cell Biol* **1994,** *6* (6), 872-6.

17. Donovan, J.; Slingerland, J., Transforming growth factor-β and breast cancer: Cell cycle arrest by transforming growth factor-β and its disruption in cancer. *Breast Cancer Res* **2000,** *2* (2), 116-24.

18. Hollstein, M., et al., p53 mutations in human cancers. *Science* **1991,** *253* (5015), 49-53.

REFERENCES

19. Lacroix, M., et al., Metabolic functions of the tumor suppressor p53: Implications in normal physiology, metabolic disorders, and cancer. *Mol Metab* **2020,** *33*, 2-22.

20. Lin, J.; Epel, E., Stress and telomere shortening: Insights from cellular mechanisms. *Ageing Res Rev* **2022,** *73*, 101507.

21. Shay, J. W., Role of telomeres and telomerase in aging and cancer. *Cancer Discov* **2016,** *6* (6), 584-93.

22. Guterres, A. N.; Villanueva, J., Targeting telomerase for cancer therapy. *Oncogene* **2020,** *39* (36), 5811-24.

23. D'Arcy, M. S., Cell death: a review of the major forms of apoptosis, necrosis and autophagy. *Cell Biol Int* **2019,** *43* (6), 582-92.

24. Lopez, J.; Tait, S. W., Mitochondrial apoptosis: killing cancer using the enemy within. *Br J Cancer* **2015,** *112* (6), 957-62.

25. Koff, J. L., et al., A time to kill: targeting apoptosis in cancer. *Int J Mol Sci* **2015,** *16* (2), 2942-55.

26. Carneiro, B. A.; El-Deiry, W. S., Targeting apoptosis in cancer therapy. *Nat Rev Clin Oncol* **2020,** *17* (7), 395-417.

27. Diepstraten, S. T., et al., The manipulation of apoptosis for cancer therapy using BH3-mimetic drugs. *Nat Rev Cancer* **2022,** *22* (1), 45-64.

28. He, S.; Sharpless, N. E., Senescence in health and disease. *Cell* **2017,** *169* (6), 1000-11.

29. Faget, D. V., et al., Unmasking senescence: context-dependent effects of SASP in cancer. *Nat Rev Cancer* **2019,** *19* (8), 439-53.

30. Zhu, Y., et al., Identification of a novel senolytic agent, navitoclax, targeting the Bcl-2 family of anti-apoptotic factors. *Aging Cell* **2016,** *15* (3), 428-35.

31. Baar, M. P., et al., Targeted apoptosis of senescent cells restores tissue homeostasis in response to chemotoxicity and aging. *Cell* **2017,** *169* (1), 132-47 e16.

32. Carmeliet, P., VEGF as a key mediator of angiogenesis in cancer. *Oncology* **2005,** *69 Suppl 3*, 4-10.

33. Baeriswyl, V.; Christofori, G., The angiogenic switch in carcinogenesis. *Semin Cancer Biol* **2009,** *19* (5), 329-37.

34. Ramakrishnan, S., et al., Vascular endothelial growth factor signaling in hypoxia and inflammation. *J Neuroimmune Pharmacol* **2014,** *9* (2), 142-60.

35. Ferrara, N., et al., Bevacizumab (Avastin), a humanized anti-VEGF monoclonal antibody for cancer therapy. *Biochem Biophys Res Commun* **2005,** *333* (2), 328-35.

36. Zhang, X.; Lawler, J., Thrombospondin-based antiangiogenic therapy. *Microvasc Res* **2007,** *74* (2-3), 90-9.

37. Klein, C. A., Cancer progression and the invisible phase of metastatic colonization. *Nat Rev Cancer* **2020,** *20* (11), 681-94.

38. Babaei, G., et al., EMT, cancer stem cells and autophagy; The three main axes of metastasis. *Biomed Pharmacother* **2021,** *133*, 110909.

39. Lamouille, S., et al., Molecular mechanisms of epithelial-mesenchymal transition. *Nat Rev Mol Cell Biol* **2014,** *15* (3), 178-96.

40. Talmadge, J. E.; Fidler, I. J., AACR centennial series: the biology of cancer metastasis: historical perspective. *Cancer Res* **2010,** *70* (14), 5649-69.

41. Gupta, G. P., et al., Identifying site-specific metastasis genes and functions. *Cold Spring Harb Symp Quant Biol* **2005,** *70*, 149-58.

42. Eyles, J., et al., Tumor cells disseminate early, but immunosurveillance limits metastatic outgrowth, in a mouse model of melanoma. *J Clin Invest* **2010,** *120* (6), 2030-9.

43. Townson, J. L.; Chambers, A. F., Dormancy of solitary metastatic cells. *Cell Cycle* **2006,** *5* (16), 1744-50.

44. Warburg, O., On the origin of cancer cells. *Science* **1956,** *123* (3191), 309-14.

45. Vander Heiden, M. G., et al., Understanding the Warburg effect: the metabolic requirements of cell proliferation. *Science* **2009,** *324* (5930), 1029-33.

46. Carvalho, K. C., et al., GLUT1 expression in malignant tumors and its use as an immunodiagnostic marker. *Clinics (Sao Paulo)* **2011,** *66* (6), 965-72.

47. Cho, H., et al., Overexpression of glucose transporter-1 (GLUT-1) predicts poor prognosis in epithelial ovarian cancer. *Cancer Invest* **2013,** *31* (9), 607-15.

48. Kunkel, M., et al., Overexpression of Glut-1 and increased glucose metabolism in tumors are associated with a poor prognosis in patients with oral squamous cell carcinoma. *Cancer* **2003,** *97* (4), 1015-24.

49. Wu, Q., et al., GLUT1 inhibition blocks growth of RB1-positive triple negative breast cancer. *Nat Commun* **2020,** *11* (1), 4205.

50. Zhang, S., et al., A GLUT1 inhibitor-based fluorogenic probe for Warburg effect-targeted drug screening and diagnostic imaging of hyperglycolytic cancers. *Anal Chim Acta* **2021,** *1167*, 338593.

51. Nguyen, T. L.; Duran, R. V., Glutamine metabolism in cancer therapy. *Cancer Drug Resist* **2018,** *1* (3), 126-38.

52. Zhang, Z., et al., ASCT2 (SLC1A5)-dependent glutamine uptake is involved in the progression of head and neck squamous cell carcinoma. *Br J Cancer* **2020,** *122* (1), 82-93.

53. van Geldermalsen, M., et al., ASCT2/SLC1A5 controls glutamine uptake and tumour growth in triple-negative basal-like breast cancer. *Oncogene* **2016,** *35* (24), 3201-8.

54. White, M. A., et al., Glutamine transporters are targets of multiple oncogenic signaling pathways in prostate cancer. *Mol Cancer Res* **2017,** *15* (8), 1017-28.

REFERENCES

55. Bott, A. J., et al., Oncogenic myc induces expression of glutamine synthetase through promoter demethylation. *Cell Metab* **2015,** *22* (6), 1068-77.

56. Duffy, M. J., et al., MYC as a target for cancer treatment. *Cancer Treat Rev* **2021,** *94*, 102154.

57. Dang, C. V., et al., MYC-induced cancer cell energy metabolism and therapeutic opportunities. *Clin Cancer Res* **2009,** *15* (21), 6479-83.

58. Sorolla, A., et al., Precision medicine by designer interference peptides: applications in oncology and molecular therapeutics. *Oncogene* **2020,** *39* (6), 1167-84.

59. Han, S., et al., IDH mutation in glioma: molecular mechanisms and potential therapeutic targets. *Br J Cancer* **2020,** *122* (11), 1580-9.

60. Tran, K. A., et al., The role of α-ketoglutarate-dependent proteins in pluripotency acquisition and maintenance. *Journal of Biological Chemistry* **2019,** *294* (14), 5408-19.

61. Parker, S. J.; Metallo, C. M., Metabolic consequences of oncogenic IDH mutations. *Pharmacol Ther* **2015,** *152*, 54-62.

62. Sulkowski, P. L., et al., 2-Hydroxyglutarate produced by neomorphic IDH mutations suppresses homologous recombination and induces PARP inhibitor sensitivity. *Sci Transl Med* **2017,** *9* (375).

63. Davis, M., et al., ML309: A potent inhibitor of R132H mutant IDH1 capable of reducing 2-hydroxyglutarate production in U87 MG glioblastoma cells. In *Probe Reports from the NIH Molecular Libraries Program*, Bethesda (MD), 2010.

64. Molenaar, R. J., et al., Radioprotection of IDH1-mutated cancer cells by the IDH1-mutant inhibitor AGI-5198. *Cancer Res* **2015,** *75* (22), 4790-802.

65. Xiao, Y.; Yu, D., Tumor microenvironment as a therapeutic target in cancer. *Pharmacol Ther* **2021,** *221*, 107753.

66. Webb, B. A., et al., Dysregulated pH: a perfect storm for cancer progression. *Nat Rev Cancer* **2011,** *11* (9), 671-7.

67. Jing, X., et al., Role of hypoxia in cancer therapy by regulating the tumor microenvironment. *Mol Cancer* **2019,** *18* (1), 157.

68. Hinshaw, D. C.; Shevde, L. A., The tumor microenvironment innately modulates cancer progression. *Cancer Res* **2019,** *79* (18), 4557-66.

69. Pages, F., et al., Immune infiltration in human tumors: A prognostic factor that should not be ignored. *Oncogene* **2010,** *29* (8), 1093-102.

70. Balkwill, F., et al., Smoldering and polarized inflammation in the initiation and promotion of malignant disease. *Cancer Cell* **2005,** *7* (3), 211-7.

71. Patel, S. A.; Minn, A. J., Combination cancer therapy with immune checkpoint blockade: Mechanisms and strategies. *Immunity* **2018,** *48* (3), 417-33.

72. Huang, R., et al., Recent advances in CAR-T cell engineering. *J Hematol Oncol* **2020,** *13* (1), 86.

REFERENCES

73. Hanahan, D., Hallmarks of cancer: New dimensions. *Cancer Discov* **2022,** *12* (1), 31-46.

74. Zhao, Y., et al., ROS signaling under metabolic stress: cross-talk between AMPK and AKT pathway. *Mol Cancer* **2017,** *16* (1), 79.

75. Jelic, M. D., et al., Oxidative stress and its role in cancer. *J Cancer Res Ther* **2021,** *17* (1), 22-8.

76. Khanzode, S. S., et al., Antioxidant enzymes and lipid peroxidation in different stages of breast cancer. *Free Radic Res* **2004,** *38* (1), 81-5.

77. Sekhar, K. R., et al., Glutathione peroxidase 4 inhibition induces ferroptosis and mTOR pathway suppression in thyroid cancer. *Sci Rep* **2022,** *12* (1), 19396.

78. Munir, R., et al., Lipid metabolism in cancer cells under metabolic stress. *Br J Cancer* **2019,** *120* (12), 1090-8.

79. Akman, M., et al., Hypoxia, endoplasmic reticulum stress and chemoresistance: dangerous liaisons. *J Exp Clin Cancer Res* **2021,** *40* (1), 28.

80. Walter, P.; Ron, D., The unfolded protein response: from stress pathway to homeostatic regulation. *Science* **2011,** *334* (6059), 1081-6.

81. Chen, X.; Cubillos-Ruiz, J. R., Endoplasmic reticulum stress signals in the tumour and its microenvironment. *Nat Rev Cancer* **2021,** *21* (2), 71-88.

82. Xu, D., et al., Endoplasmic reticulum stress targeted therapy for breast cancer. *Cell Commun Signal* **2022,** *20* (1), 174.

83. Wang, M., et al., Role of the unfolded protein response regulator GRP78/BiP in development, cancer, and neurological disorders. *Antioxid Redox Signal* **2009,** *11* (9), 2307-16.

84. Di Conza, G.; Ho, P. C., ER stress responses: An emerging modulator for innate immunity. *Cells* **2020,** *9* (3).

85. Abdullah, T. M., et al., Endoplasmic reticulum stress-induced release and binding of calreticulin from human ovarian cancer cells. *Cancer Immunol Immunother* **2022,** *71* (7), 1655-69.

86. Axten, J. M., et al., Discovery of 7-methyl-5-(1-[3-(trifluoromethyl)phenyl]acetyl-2,3-dihydro-1H-indol-5-yl)-7H-pyrrolo[2,3-d]pyrimidin-4-amine (GSK2606414), a potent and selective first-in-class inhibitor of protein kinase R (PKR)-like endoplasmic reticulum kinase (PERK). *J Med Chem* **2012,** *55* (16), 7193-207.

87. Gallagher, C. M.; Walter, P., Ceapins inhibit ATF6α signaling by selectively preventing transport of ATF6α to the Golgi apparatus during ER stress. *Elife* **2016,** *5*.

88. Cojocari, D., et al., New small molecule inhibitors of UPR activation demonstrate that PERK, but not IRE1alpha signaling is essential for promoting adaptation and survival to hypoxia. *Radiother Oncol* **2013,** *108* (3), 541-7.

89. Shimomura, I., et al., Selective targeting of KRAS-driven lung tumorigenesis via unresolved ER stress. *JCI Insight* **2021,** *6* (7).

REFERENCES

90. Watson, J. D.; Crick, F. H., Molecular structure of nucleic acids; a structure for deoxyribose nucleic acid. *Nature* **1953,** *171* (4356), 737-8.

91. Masai, H., et al., Eukaryotic chromosome DNA replication: where, when, and how? *Annu Rev Biochem* **2010,** *79*, 89-130.

92. Bleichert, F., Mechanisms of replication origin licensing: a structural perspective. *Curr Opin Struct Biol* **2019,** *59*, 195-204.

93. Carey, J. F., et al., DNA relaxation by human topoisomerase I occurs in the closed clamp conformation of the protein. *Proc Natl Acad Sci U S A* **2003,** *100* (10), 5640-5.

94. Hubscher, U., DNA replication fork proteins. *Methods Mol Biol* **2009,** *521*, 19-33.

95. Parker, N., et al., Microbiology. *OpenStax:* **2016**.

96. Wu, L., et al., Mechanism of chromosomal DNA replication initiation and replication fork stabilization in eukaryotes. *Sci China Life Sci* **2014,** *57* (5), 482-7.

97. Clarke, T. L.; Mostoslavsky, R., DNA repair as a shared hallmark in cancer and ageing. *Mol Oncol* **2022,** *16* (18), 3352-79.

98. Chatterjee, N.; Walker, G. C., Mechanisms of DNA damage, repair, and mutagenesis. *Environ Mol Mutagen* **2017,** *58* (5), 235-63.

99. Jackson, S. P.; Bartek, J., The DNA-damage response in human biology and disease. *Nature* **2009,** *461* (7267), 1071-8.

100. Hosoya, N.; Miyagawa, K., Targeting DNA damage response in cancer therapy. *Cancer Sci* **2014,** *105* (4), 370-88.

101. Nam, E. A.; Cortez, D., ATR signalling: more than meeting at the fork. *Biochem J* **2011,** *436* (3), 527-36.

102. Chou, W. C., et al., Initiation of the ATM-CHK2 DNA damage response through the base excision repair pathway. *Carcinogenesis* **2015,** *36* (8), 832-40.

103. Huang, R. X.; Zhou, P. K., DNA damage response signaling pathways and targets for radiotherapy sensitization in cancer. *Signal Transduct Target Ther* **2020,** *5* (1), 60.

104. Krokan, H. E.; Bjoras, M., Base excision repair. *Cold Spring Harb Perspect Biol* **2013,** *5* (4), a012583.

105. McKinnon, P. J.; Caldecott, K. W., DNA strand break repair and human genetic disease. *Annu Rev Genomics Hum Genet* **2007,** *8*, 37-55.

106. Shao, Z., et al., Persistently bound Ku at DNA ends attenuates DNA end resection and homologous recombination. *DNA Repair (Amst)* **2012,** *11* (3), 310-6.

107. Gupta, A., et al., Role of 53BP1 in the regulation of DNA double-strand break repair pathway choice. *Radiat Res* **2014,** *181* (1), 1-8.

108. Maya-Mendoza, A., et al., High speed of fork progression induces DNA replication stress and genomic instability. *Nature* **2018,** *559* (7713), 279-84.

109. Vesela, E., et al., Common chemical inductors of replication stress: focus on cell-based studies. *Biomolecules* **2017,** *7* (1).

110. Zeman, M. K.; Cimprich, K. A., Causes and consequences of replication stress. *Nat Cell Biol* **2014,** *16* (1), 2-9.

111. Barlow, J. H., et al., Identification of early replicating fragile sites that contribute to genome instability. *Cell* **2013,** *152* (3), 620-32.

112. Nick McElhinny, S. A., et al., Genome instability due to ribonucleotide incorporation into DNA. *Nat Chem Biol* **2010,** *6* (10), 774-81.

113. Macheret, M.; Halazonetis, T. D., DNA replication stress as a hallmark of cancer. *Annu Rev Pathol* **2015,** *10*, 425-48.

114. Kotsantis, P., et al., Mechanisms of oncogene-induced replication stress: Jigsaw falling into place. *Cancer Discov* **2018,** *8* (5), 537-55.

115. Kondratick, C. M., et al., Making choices: DNA replication fork recovery mechanisms. *Semin Cell Dev Biol* **2021,** *113*, 27-37.

116. Neelsen, K. J.; Lopes, M., Replication fork reversal in eukaryotes: from dead end to dynamic response. *Nat Rev Mol Cell Biol* **2015,** *16* (4), 207-20.

117. Petermann, E.; Helleday, T., Pathways of mammalian replication fork restart. *Nat Rev Mol Cell Biol* **2010,** *11* (10), 683-7.

118. Liao, H., et al., Mechanisms for stalled replication fork stabilization: new targets for synthetic lethality strategies in cancer treatments. *EMBO Rep* **2018,** *19* (9).

119. Carr, A. M.; Lambert, S., Replication stress-induced genome instability: the dark side of replication maintenance by homologous recombination. *J Mol Biol* **2013,** *425* (23), 4733-44.

120. Murga, M., et al., A mouse model of ATR-Seckel shows embryonic replicative stress and accelerated aging. *Nat Genet* **2009,** *41* (8), 891-8.

121. Taylor, A. M., et al., Ataxia-telangiectasia-like disorder (ATLD)-its clinical presentation and molecular basis. *DNA Repair (Amst)* **2004,** *3* (8-9), 1219-25.

122. Ubhi, T.; Brown, G. W., Exploiting DNA replication stress for cancer treatment. *Cancer Res* **2019,** *79* (8), 1730-9.

123. Durinikova, E., et al., Targeting the DNA damage response pathways and replication ctress in colorectal cancer. *Clin Cancer Res* **2022,** *28* (17), 3874-89.

124. Fokas, E., et al., Targeting ATR in DNA damage response and cancer therapeutics. *Cancer Treat Rev* **2014,** *40* (1), 109-17.

125. Patties, I., et al., The CHK1 inhibitor SAR-020106 sensitizes human glioblastoma cells to irradiation, to temozolomide, and to decitabine treatment. *J Exp Clin Cancer Res* **2019,** *38* (1), 420.

126. Parsels, L. A., et al., Gemcitabine sensitization by checkpoint kinase 1 inhibition correlates with inhibition of a Rad51 DNA damage response in pancreatic cancer cells. *Mol Cancer Ther* **2009,** *8* (1), 45-54.

REFERENCES

127. Vyas, S., et al., Family-wide analysis of poly(ADP-ribose) polymerase activity. *Nat Commun* **2014,** *5*, 4426.

128. Liu, C., et al., The role of poly ADP-ribosylation in the first wave of DNA damage response. *Nucleic Acids Res* **2017,** *45* (14), 8129-41.

129. Houl, J. H., et al., Selective small molecule PARG inhibitor causes replication fork stalling and cancer cell death. *Nat Commun* **2019,** *10* (1), 5654.

130. Eustermann, S., et al., Structural basis of detection and signaling of DNA single-strand breaks by human PARP-1. *Mol Cell* **2015,** *60* (5), 742-54.

131. Haince, J. F., et al., Ataxia telangiectasia mutated (ATM) signaling network is modulated by a novel poly(ADP-ribose)-dependent pathway in the early response to DNA-damaging agents. *J Biol Chem* **2007,** *282* (22), 16441-53.

132. Haince, J. F., et al., PARP1-dependent kinetics of recruitment of MRE11 and NBS1 proteins to multiple DNA damage sites. *J Biol Chem* **2008,** *283* (2), 1197-208.

133. Parsons, J. L., et al., Poly(ADP-ribose) polymerase-1 protects excessive DNA strand breaks from deterioration during repair in human cell extracts. *FEBS J* **2005,** *272* (8), 2012-21.

134. Hegde, M. L., et al., Early steps in the DNA base excision/single-strand interruption repair pathway in mammalian cells. *Cell Res* **2008,** *18* (1), 27-47.

135. Sugimura, K., et al., PARP-1 ensures regulation of replication fork progression by homologous recombination on damaged DNA. *J Cell Biol* **2008,** *183* (7), 1203-12.

136. Los, M., et al., Activation and caspase-mediated inhibition of PARP: a molecular switch between fibroblast necrosis and apoptosis in death receptor signaling. *Mol Biol Cell* **2002,** *13* (3), 978-88.

137. Langelier, M. F., et al., PARP family enzymes: regulation and catalysis of the poly(ADP-ribose) posttranslational modification. *Curr Opin Struct Biol* **2018,** *53*, 187-98.

138. Cybulla, E.; Vindigni, A., Leveraging the replication stress response to optimize cancer therapy. *Nature Reviews Cancer* **2023,** *23* (1), 6-24.

139. Pommier, Y., et al., Laying a trap to kill cancer cells: PARP inhibitors and their mechanisms of action. *Sci Transl Med* **2016,** *8* (362), 362ps17.

140. Zandarashvili, L., et al., Structural basis for allosteric PARP-1 retention on DNA breaks. *Science* **2020,** *368* (6486).

141. Kim, G., et al., FDA approval summary: Olaparib monotherapy in patients with deleterious germline BRCA-mutated advanced ovarian cancer treated with three or more lines of chemotherapy. *Clin Cancer Res* **2015,** *21* (19), 4257-61.

142. Audeh, M. W., et al., Phase II trial of the oral PARP inhibitor olaparib (AZD2281) in BRCA-deficient advanced ovarian cancer. *Journal of Clinical Oncology* **2009,** *27* (15_suppl), 5500-.

REFERENCES

143. Domchek, S. M., et al., Efficacy and safety of olaparib monotherapy in germline BRCA1/2 mutation carriers with advanced ovarian cancer and three or more lines of prior therapy. *Gynecol Oncol* **2016,** *140* (2), 199-203.

144. Ledermann, J., et al., Olaparib maintenance therapy in platinum-sensitive relapsed ovarian cancer. *N Engl J Med* **2012,** *366* (15), 1382-92.

145. Scott, L. J., Niraparib: First global approval. *Drugs* **2017,** *77* (9), 1029-34.

146. Dockery, L. E., et al., Rucaparib: the past, present, and future of a newly approved PARP inhibitor for ovarian cancer. *Onco Targets Ther* **2017,** *10*, 3029-37.

147. Shen, Y., et al., BMN 673, a novel and highly potent PARP1/2 inhibitor for the treatment of human cancers with DNA repair deficiency. *Clin Cancer Res* **2013,** *19* (18), 5003-15.

148. Hoy, S. M., Talazoparib: First global approval. *Drugs* **2018,** *78* (18), 1939-46.

149. Murai, J., et al., Stereospecific PARP trapping by BMN 673 and comparison with olaparib and rucaparib. *Mol Cancer Ther* **2014,** *13* (2), 433-43.

150. Faraoni, I.; Graziani, G., Role of BRCA mutations in cancer treatment with poly(ADP-ribose) polymerase (PARP) inhibitors. *Cancers (Basel)* **2018,** *10* (12).

151. Keung, M. Y., et al., Response of breast cancer cells to PARP inhibitors is independent of BRCA status. *J Clin Med* **2020,** *9* (4).

152. Colicchia, V., et al., PARP inhibitors enhance replication stress and cause mitotic catastrophe in MYCN-dependent neuroblastoma. *Oncogene* **2017,** *36* (33), 4682-91.

153. Li, X., et al., High PARP-1 expression predicts poor survival in acute myeloid leukemia and PARP-1 inhibitor and SAHA-bendamustine hybrid inhibitor combination treatment synergistically enhances anti-tumor effects. *EBioMedicine* **2018,** *38*, 47-56.

154. Puentes, L. N., et al., Evaluation of a low-toxicity PARP inhibitor as a neuroprotective agent for Parkinson's disease. *Mol Neurobiol* **2021,** *58* (8), 3641-52.

155. Liu, H., et al., Nuclear cGAS suppresses DNA repair and promotes tumorigenesis. *Nature* **2018,** *563* (7729), 131-6.

156. Luigi, A., et al., DNA fiber assay upon treatment with ultraviolet radiations. *Bio Protoc* **2017,** *7* (11), e2301.

157. James, D. I., et al., First-in-class chemical probes against poly(ADP-ribose) glycohydrolase (PARG) inhibit DNA repair with differential pharmacology to olaparib. *ACS Chem Biol* **2016,** *11* (11), 3179-90.

158. Pillay, N., et al., DNA replication stress and emerging prospects for PARG inhibitors in ovarian cancer therapy. *Prog Biophys Mol Biol* **2021,** *163*, 160-70.

159. King, D., et al., Increased replication stress determines ATR inhibitor sensitivity in neuroblastoma cells. *Cancers (Basel)* **2021,** *13* (24).

160. Liu, Q., et al., CHK1 is an essential kinase that is regulated by Atr and required for the G_2/M DNA damage checkpoint. *Genes Dev* **2000,** *14* (12), 1448-59.

REFERENCES

161. Zhang, Y.; Hunter, T., Roles of CHK1 in cell biology and cancer therapy. *Int J Cancer* **2014,** *134* (5), 1013-23.

162. Olcina, M. M., et al., Replication stress and chromatin context link ATM activation to a role in DNA replication. *Mol Cell* **2013,** *52* (5), 758-66.

163. Bakkenist, C. J.; Kastan, M. B., DNA damage activates ATM through intermolecular autophosphorylation and dimer dissociation. *Nature* **2003,** *421* (6922), 499-506.

164. Nadkarni, A., et al., ATM inhibitor KU-55933 increases the TMZ responsiveness of only inherently TMZ sensitive GBM cells. *J Neurooncol* **2012,** *110* (3), 349-57.

165. Jin, M. H.; Oh, D. Y., ATM in DNA repair in cancer. *Pharmacol Ther* **2019,** *203*, 107391.

166. Huang, C., et al., Sensors and Inhibitors for the Detection of Ataxia Telangiectasia Mutated (ATM) Protein Kinase. *Mol Pharm* **2021,** *18* (7), 2470-81.

167. Austin, W. R., et al., Nucleoside salvage pathway kinases regulate hematopoiesis by linking nucleotide metabolism with replication stress. *J Exp Med* **2012,** *209* (12), 2215-28.

168. Beyaert, M., et al., A crucial role for ATR in the regulation of deoxycytidine kinase activity. *Biochem Pharmacol* **2016,** *100*, 40-50.

169. Song, D., et al., DCK is a promising prognostic biomarker and correlated with immune infiltrates in hepatocellular carcinoma. *World J Surg Oncol* **2020,** *18* (1), 176.

170. Illuzzi, G., et al., PARG is dispensable for recovery from transient replicative stress but required to prevent detrimental accumulation of poly(ADP-ribose) upon prolonged replicative stress. *Nucleic Acids Res* **2014,** *42* (12), 7776-92.

171. Moiseeva, T. N., et al., WEE1 kinase inhibitor AZD1775 induces CDK1 kinase-dependent origin firing in unperturbed G1- and S-phase cells. *Proc Natl Acad Sci U S A* **2019,** *116* (48), 23891-3.

172. Aarts, M., et al., Forced mitotic entry of S-phase cells as a therapeutic strategy induced by inhibition of WEE1. *Cancer Discov* **2012,** *2* (6), 524-39.

173. Weber, A. M.; Ryan, A. J., ATM and ATR as therapeutic targets in cancer. *Pharmacol Ther* **2015,** *149*, 124-38.

174. Luczak, M. W.; Zhitkovich, A., Monoubiquitinated γH2AX: Abundant product and specific biomarker for non-apoptotic DNA double-strand breaks. *Toxicol Appl Pharmacol* **2018,** *355*, 238-46.

175. Rogakou, E. P., et al., Initiation of DNA fragmentation during apoptosis induces phosphorylation of H2AX histone at serine 139. *J Biol Chem* **2000,** *275* (13), 9390-5.

176. Bernadotte, A., et al., Markers of cellular senescence. Telomere shortening as a marker of cellular senescence. *Aging (Albany NY)* **2016,** *8* (1), 3-11.

177. White, R. R., et al., Controlled induction of DNA double-strand breaks in the mouse liver induces features of tissue ageing. *Nat Commun* **2015,** *6*, 6790.

REFERENCES

178. Venkatesan, S., et al., Induction of APOBEC3 exacerbates DNA replication stress and chromosomal instability in early breast and lung cancer evolution. *Cancer Discov* **2021,** *11* (10), 2456-73.

179. Roberts, S. A., et al., An APOBEC cytidine deaminase mutagenesis pattern is widespread in human cancers. *Nat Genet* **2013,** *45* (9), 970-6.

180. Kanu, N., et al., DNA replication stress mediates APOBEC3 family mutagenesis in breast cancer. *Genome Biol* **2016,** *17* (1), 185.

181. Yates, L. A., et al., A structural and dynamic model for the assembly of Replication Protein A on single-stranded DNA. *Nat Commun* **2018,** *9* (1), 5447.

182. Zou, Y., et al., Functions of human replication protein A (RPA): from DNA replication to DNA damage and stress responses. *J Cell Physiol* **2006,** *208* (2), 267-73.

183. Sleeth, K. M., et al., RPA mediates recombination repair during replication stress and is displaced from DNA by checkpoint signalling in human cells. *J Mol Biol* **2007,** *373* (1), 38-47.

184. Glanzer, J. G., et al., RPA inhibition increases replication stress and suppresses tumor growth. *Cancer Res* **2014,** *74* (18), 5165-72.

185. Bonilla, B., et al., RAD51 gene family structure and function. *Annu Rev Genet* **2020,** *54,* 25-46.

186. Shkundina, I. S., et al., New RAD51 inhibitors to target homologous recombination in human cells. *Genes (Basel)* **2021,** *12* (6).

187. Kotsantis, P., et al., Increased global transcription activity as a mechanism of replication stress in cancer. *Nat Commun* **2016,** *7,* 13087.

188. Zhang, S., et al., STAT3/c-myc axis-mediated metabolism alternations of inflammation-related glycolysis involve with colorectal carcinogenesis. *Rejuvenation Res* **2019,** *22* (2), 138-45.

189. Sheng, X., et al., IRE1α-XBP1s pathway promotes prostate cancer by activating c-myc signaling. *Nat Commun* **2019,** *10* (1), 323.

190. Wang, T., et al., c-Myc overexpression promotes oral cancer cell proliferation and migration by enhancing glutaminase and glutamine synthetase activity. *Am J Med Sci* **2019,** *358* (3), 235-42.

191. Myers, W. G., The first radioindicator study in the life sciences with a man-made radionuclide: "Radioactive indicators in the study of phosphorus metabolism in rats, by O. Chievitz and G. Hevesy, reprinted from Nature 136: 754-755, Nov. 9, 1935.". *J Nucl Med* **1975,** *16* (12), 1106-8.

192. Hutton, B. F., The origins of SPECT and SPECT/CT. *Eur J Nucl Med Mol I* **2014,** *41,* S3-S16.

193. Jones, T.; Townsend, D., History and future technical innovation in positron emission tomography. *J Med Imaging (Bellingham)* **2017,** *4* (1), 011013.

194. Kiessling, F., et al., Small Animal Imaging. 2 ed.; *Springer Cham:* **2017**.

REFERENCES

195. Jodal, L., et al., Positron range in PET imaging: An alternative approach for assessing and correcting the blurring. *Phys Med Biol* **2012,** *57* (12), 3931-43.

196. Nolting, D. D., et al., Molecular imaging probe development: a chemistry perspective. *Am J Nucl Med Mol Imaging* **2012,** *2* (3), 273-306.

197. Sun, X., et al., Positron emission tomography imaging using radiolabeled inorganic nanomaterials. *Acc Chem Res* **2015,** *48* (2), 286-94.

198. Conti, M.; Eriksson, L., Physics of pure and non-pure positron emitters for PET: a review and a discussion. *EJNMMI Phys* **2016,** *3* (1), 8.

199. Levin, C. S.; Hoffman, E. J., Calculation of positron range and its effect on the fundamental limit of positron emission tomography system spatial resolution. *Phys Med Biol* **1999,** *44* (3), 781-99.

200. Ballinger, J. R., Theranostic radiopharmaceuticals: established agents in current use. *Br J Radiol* **2018,** *91* (1091), 20170969.

201. Grover, V. P., et al., Magnetic resonance imaging: Principles and techniques: Lessons for clinicians. *J Clin Exp Hepatol* **2015,** *5* (3), 246-55.

202. Caldemeyer, K. S.; Buckwalter, K. A., The basic principles of computed tomography and magnetic resonance imaging. *J Am Acad Dermatol* **1999,** *41* (5 Pt 1), 768-71.

203. Giesel, F. L., et al., ^{68}Ga-FAPI PET/CT: Biodistribution and preliminary dosimetry estimate of 2 DOTA-containing FAP-targeting agents in patients with various cancers. *J Nucl Med* **2019,** *60* (3), 386-92.

204. Zippel, C., et al., Current status of PSMA-radiotracers for prostate cancer: Data analysis of prospective trials listed on clinicaltrials.gov. *Pharmaceuticals (Basel)* **2020,** *13* (1).

205. Banks, W. A., Characteristics of compounds that cross the blood-brain barrier. *BMC Neurol* **2009,** *9 Suppl 1*, S3.

206. Herfert, K., et al., Preclinical Experimentation in Neurology. In *Radiopharmaceutical Chemistry*, Lewis, J. S.; Windhorst, A. D.; Zeglis, B. M., Eds. Springer International Publishing: Cham, 2019; pp 583-606.

207. Schinkel, A. H., P-Glycoprotein, a gatekeeper in the blood-brain barrier. *Adv Drug Deliv Rev* **1999,** *36* (2-3), 179-94.

208. Schoder, H., et al., Safety and feasibility of PARP1/2 imaging with [^{18}F]PARPi in patients with head and neck cancer. *Clin Cancer Res* **2020,** *26* (13), 3110-6.

209. Carney, B., et al., Non-invasive PET imaging of PARP1 expression in glioblastoma models. *Mol Imaging Biol* **2016,** *18* (3), 386-92.

210. Carney, B., et al., Molecular imaging of PARP. *J Nucl Med* **2017,** *58* (7), 1025-30.

211. Reiner, T., et al., Synthesis and in vivo imaging of a ^{18}F-labeled PARP1 inhibitor using a chemically orthogonal scavenger-assisted high-performance method. *Angew Chem Int Ed Engl* **2011,** *50* (8), 1922-5.

REFERENCES

212. Zhou, D., et al., Synthesis, [^{18}F] radiolabeling, and evaluation of poly (ADP-ribose) polymerase-1 (PARP-1) inhibitors for in vivo imaging of PARP-1 using positron emission tomography. *Bioorg Med Chem* **2014,** *22* (5), 1700-7.

213. Stotz, S., et al., Two experts and a newbie: [^{18}F]PARPi vs [^{18}F]FTT vs [^{18}F]FPyPARP-a comparison of PARP imaging agents. *Eur J Nucl Med Mol Imaging* **2022,** *49* (3), 834-46.

214. Bowden, G. D., et al., DoE optimization empowers the automated preparation of enantiomerically pure [^{18}F]talazoparib and its in vivo evaluation as a PARP radiotracer. *J Med Chem* **2021,** *64* (21), 15690-701.

215. Bowden, G. D., et al., Scalable ^{18}F processing conditions for copper-mediated radiofluorination chemistry facilitate "design of experiments" (DoE) optimization dtudies and afford an improved dynthesis of [^{18}F]olaparib. Preprint, doi: 10.26434/chemrxiv.14547342.v1. **2021**.

216. Guibbal, F., et al., Manual and automated Cu-mediated radiosynthesis of the PARP inhibitor [^{18}F]olaparib. *Nat Protoc* **2020,** *15* (4), 1525-41.

217. Wilson, T. C., et al., PET imaging of PARP expression using [^{18}F]olaparib. *J Nucl Med* **2019,** *60* (4), 504-10.

218. Shuhendler, A. J., et al., [^{18}F]-SuPAR: A radiofluorinated probe for noninvasive imaging of DNA damage-dependent poly(ADP-ribose) polymerase activity. *Bioconjug Chem* **2019,** *30* (5), 1331-42.

219. Edmonds, C. E., et al., [^{18}F]FluorThanatrace uptake as a marker of PARP1 expression and activity in breast cancer. *Am J Nucl Med Mol Imaging* **2016,** *6* (1), 94-101.

220. Zhou, D., et al., Radiosynthesis and evaluation of talazoparib and its derivatives as PARP-1-targeting agents. *Biomedicines* **2021,** *9* (5).

221. Chen, Z., et al., Copper-mediated radiosynthesis of [^{18}F]rucaparib. *Org Lett* **2021,** *23* (18), 7290-4.

222. Guibbal, F., et al., [^{18}F]AZD2461, an insight on difference in PARP binding profiles for DNA damage response PET imaging. *Mol Imaging Biol* **2020,** *22* (5), 1226-34.

223. Naylor, L. H., Reporter gene technology: the future looks bright. *Biochem Pharmacol* **1999,** *58* (5), 749-57.

224. Li, S., et al., Overview of the reporter genes and reporter mouse models. *Animal Model Exp Med* **2018,** *1* (1), 29-35.

225. Livet, J., et al., Transgenic strategies for combinatorial expression of fluorescent proteins in the nervous system. *Nature* **2007,** *450* (7166), 56-62.

226. Soboleski, M. R., et al., Green fluorescent protein is a quantitative reporter of gene expression in individual eukaryotic cells. *FASEB J* **2005,** *19* (3), 440-2.

227. Stacer, A. C., et al., NanoLuc reporter for dual luciferase imaging in living animals. *Mol Imaging* **2013,** *12* (7), 1-13.

228. Williams, T. M., et al., Advantages of firefly luciferase as a reporter gene: application to the interleukin-2 gene promoter. *Anal Biochem* **1989,** *176* (1), 28-32.

REFERENCES

229. Ting, A. Y., et al., Genetically encoded fluorescent reporters of protein tyrosine kinase activities in living cells. *Proc Natl Acad Sci U S A* **2001,** *98* (26), 15003-8.

230. Gao, X., et al., In vivo cancer targeting and imaging with semiconductor quantum dots. *Nat Biotechnol* **2004,** *22* (8), 969-76.

231. Smith, A. M., et al., Bioimaging: second window for in vivo imaging. *Nat Nanotechnol* **2009,** *4* (11), 710-1.

232. Keereweer, S., et al., Optical image-guided cancer surgery: challenges and limitations. *Clin Cancer Res* **2013,** *19* (14), 3745-54.

233. Mukherjee, A., et al., Non-invasive imaging using reporter genes altering cellular water permeability. *Nat Commun* **2016,** *7*, 13891.

234. Yang, C., et al., MRI reporter genes for noninvasive molecular imaging. *Molecules* **2016,** *21* (5).

235. Brindle, K. M., Gene reporters for magnetic resonance imaging. *Trends Genet* **2022,** *38* (10), 996-8.

236. Schilling, F., et al., MRI measurements of reporter-mediated increases in transmembrane water exchange enable detection of a gene reporter. *Nat Biotechnol* **2017,** *35* (1), 75-80.

237. Shuboni-Mulligan, D. D., et al., Dynamic contrast-enhanced MRI of OATP dysfunction in diabetes. *Diabetes* **2019,** *68* (2), 271-80.

238. Bourdeau, R. W., et al., Acoustic reporter genes for noninvasive imaging of microorganisms in mammalian hosts. *Nature* **2018,** *553* (7686), 86-90.

239. Shapiro, M. G., et al., Genetically encoded reporters for hyperpolarized xenon magnetic resonance imaging. *Nat Chem* **2014,** *6* (7), 629-34.

240. Gao, T., et al., Reporter genes for brain imaging using MRI, SPECT and PET. *Int J Mol Sci* **2022,** *23* (15).

241. Thunemann, M., et al., Cre/lox-assisted non-invasive in vivo tracking of specific cell populations by positron emission tomography. *Nat Commun* **2017,** *8* (1), 444.

242. Alauddin, M. M.; Conti, P. S., Synthesis and preliminary evaluation of 9-(4-[18F]fluoro-3-hydroxymethylbutyl)guanine ([18F]FHBG): a new potential imaging agent for viral infection and gene therapy using PET. *Nucl Med Biol* **1998,** *25* (3), 175-80.

243. Gambhir, S. S., et al., A mutant herpes simplex virus type 1 thymidine kinase reporter gene shows improved sensitivity for imaging reporter gene expression with positron emission tomography. *Proc Natl Acad Sci U S A* **2000,** *97* (6), 2785-90.

244. Black, M. E., et al., Creation of drug-specific herpes simplex virus type 1 thymidine kinase mutants for gene therapy. *Proc Natl Acad Sci U S A* **1996,** *93* (8), 3525-9.

245. Yaghoubi, S. S., et al., Noninvasive detection of therapeutic cytolytic T cells with [18F]FHBG PET in a patient with glioma. *Nat Clin Pract Oncol* **2009,** *6* (1), 53-8.

REFERENCES

246. Alauddin, M. M., et al., In vivo evaluation of 2'-deoxy-2'-[18F]fluoro-5-iodo-1-beta-D-arabinofuranosyluracil ([18F]FIAU) and 2'-deoxy-2'-[18F]fluoro-5-ethyl-1-beta-D-arabinofuranosyluracil ([18F]FEAU) as markers for suicide gene expression. *Eur J Nucl Med Mol Imaging* **2007,** *34* (6), 822-9.

247. Nasu, Y., et al., Suicide gene therapy with adenoviral delivery of HSV-tK gene for patients with local recurrence of prostate cancer after hormonal therapy. *Mol Ther* **2007,** *15* (4), 834-40.

248. Yaghoubi, S., et al., Human pharmacokinetic and dosimetry studies of [18F]FHBG: a reporter probe for imaging herpes simplex virus type-1 thymidine kinase reporter gene expression. *J Nucl Med* **2001,** *42* (8), 1225-34.

249. Haywood, T., et al., Positron emission tomography reporter gene strategy for use in the central nervous system. *Proc Natl Acad Sci U S A* **2019,** *116* (23), 11402-7.

250. Mukherjee, J., et al., Pyruvate kinase M2 expression, but not pyruvate kinase activity, is up-regulated in a grade-specific manner in human glioma. *PLoS One* **2013,** *8* (2), e57610.

251. Beinat, C., et al., Development of [18F]DASA-23 for imaging tumor glycolysis through noninvasive measurement of pyruvate kinase M2. *Mol Imaging Biol* **2017,** *19* (5), 665-72.

252. Beinat, C., et al., A clinical PET imaging tracer ([18F]DASA-23) to monitor pyruvate kinase M2-induced glycolytic reprogramming in glioblastoma. *Clin Cancer Res* **2021,** *27* (23), 6467-78.

253. Sellmyer, M. A., et al., Quantitative PET reporter gene imaging with [11C]trimethoprim. *Mol Ther* **2017,** *25* (1), 120-6.

254. Sellmyer, M. A., et al., Bacterial infection imaging with [18F]fluoropropyl-trimethoprim. *Proc Natl Acad Sci U S A* **2017,** *114* (31), 8372-7.

255. Bushby, S. R.; Hitchings, G. H., Trimethoprim, a sulphonamide potentiator. *Br J Pharmacol Chemother* **1968,** *33* (1), 72-90.

256. Shimojo, M., et al., A genetically targeted reporter for PET imaging of deep neuronal circuits in mammalian brains. *EMBO J* **2021,** *40* (22), e107757.

257. Baril, P., et al., Visualization of gene expression in the live subject using the Na/I symporter as a reporter gene: applications in biotherapy. *Br J Pharmacol* **2010,** *159* (4), 761-71.

258. Schipper, M. L., et al., Efficacy of 99mTc pertechnetate and 131I radioisotope therapy in sodium/iodide symporter (NIS)-expressing neuroendocrine tumors in vivo. *Eur J Nucl Med Mol Imaging* **2007,** *34* (5), 638-50.

259. Miederer, M., et al., Iodine-124 PET quantification of organ-specific delivery and expression of NIS-encoding RNA. *EJNMMI Res* **2021,** *11* (1), 14.

260. Jiang, H.; DeGrado, T. R., [18F]Tetrafluoroborate ([18F]TFB) and its analogs for PET imaging of the sodium/iodide symporter. *Theranostics* **2018,** *8* (14), 3918-31.

261. Castanares, M. A., et al., Evaluation of prostate-specific membrane antigen as an imaging reporter. *J Nucl Med* **2014,** *55* (5), 805-11.

REFERENCES

262. Rowe, S. P., et al., [^{18}F]DCFPyL PET/CT for imaging of prostate cancer. *Nuklearmedizin* **2022,** *61* (3), 240-6.

263. Minn, I., et al., Imaging CAR T cell therapy with PSMA-targeted positron emission tomography. *Sci Adv* **2019,** *5* (7), eaaw5096.

264. Piron, S., et al., Radiation dosimetry and biodistribution of [^{18}F]PSMA-11 for PET imaging of prostate cancer. *J Nucl Med* **2019,** *60* (12), 1736-42.

265. Sterzing, F., et al., (68)Ga-PSMA-11 PET/CT: a new technique with high potential for the radiotherapeutic management of prostate cancer patients. *Eur J Nucl Med Mol Imaging* **2016,** *43* (1), 34-41.

266. Gust, J., et al., Endothelial activation and blood-brain barrier disruption in neurotoxicity after adoptive immunotherapy with CD19 CAR-T cells. *Cancer Discov* **2017,** *7* (12), 1404-19.

267. Wu, M. R., et al., Organic anion-transporting polypeptide 1B3 as a dual reporter gene for fluorescence and magnetic resonance imaging. *FASEB J* **2018,** *32* (3), 1705-15.

268. Patrick, P. S., et al., Dual-modality gene reporter for in vivo imaging. *Proc Natl Acad Sci U S A* **2014,** *111* (1), 415-20.

269. Wadas, T. J., et al., Coordinating radiometals of copper, gallium, indium, yttrium, and zirconium for PET and SPECT imaging of disease. *Chem Rev* **2010,** *110* (5), 2858-902.

270. Kimura, H., et al., Radiosynthesis of novel pitavastatin derivative [^{18}F]PTV-F1 as a tracer for hepatic OATP using a one-pot synthetic procedure. *J Labelled Comp Radiopharm* **2016,** *59* (13), 565-75.

271. Sellmyer, M. A., et al., Imaging CAR T cell trafficking with eDHFR as a PET reporter gene. *Mol Ther* **2020,** *28* (1), 42-51.

272. Traversari, C., et al., The potential immunogenicity of the TK suicide gene does not prevent full clinical benefit associated with the use of TK-transduced donor lymphocytes in HSCT for hematologic malignancies. *Blood* **2007,** *109* (11), 4708-15.

273. Yonemori, K., et al., Disruption of the blood brain barrier by brain metastases of triple-negative and basal-type breast cancer but not HER2/neu-positive breast cancer. *Cancer* **2010,** *116* (2), 302-8.

274. Sweeney, M. D., et al., Blood-brain barrier breakdown in Alzheimer disease and other neurodegenerative disorders. *Nat Rev Neurol* **2018,** *14* (3), 133-50.

275. Arvanitis, C. D., et al., The blood-brain barrier and blood-tumour barrier in brain tumours and metastases. *Nat Rev Cancer* **2020,** *20* (1), 26-41.

276. Serres, S., et al., Molecular MRI enables early and sensitive detection of brain metastases. *Proc Natl Acad Sci U S A* **2012,** *109* (17), 6674-9.

277. Yang, H., et al., Inhibition of checkpoint kinase 1 sensitizes lung cancer brain metastases to radiotherapy. *Biochem Biophys Res Commun* **2011,** *406* (1), 53-8.

REFERENCES

278. Baschnagel, A. M., et al., ATR inhibitor M6620 (VX-970) enhances the effect of radiation in non-small cell lung cancer brain metastasis patient-derived xenografts. *Mol Cancer Ther* **2021,** *20* (11), 2129-39.

279. Tao, M., et al., Niraparib as maintenance therapy in germline ATM-mutated and somatic BRCA2-mutated ovarian cancer with brain metastases: A case report and literature review. *Onco Targets Ther* **2020,** *13*, 12979-86.

280. Janssen, D. B., Evolving haloalkane dehalogenases. *Curr Opin Chem Biol* **2004,** *8* (2), 150-9.

281. Pries, F., et al., Histidine 289 is essential for hydrolysis of the alkyl-enzyme intermediate of haloalkane dehalogenase. *J Biol Chem* **1995,** *270* (18), 10405-11.

282. Los, G. V., et al., HaloTag: a novel protein labeling technology for cell imaging and protein analysis. *ACS Chem Biol* **2008,** *3* (6), 373-82.

283. England, C. G., et al., HaloTag technology: a versatile platform for biomedical applications. *Bioconjug Chem* **2015,** *26* (6), 975-86.

284. Chen, W., et al., Recent biomedical advances enabled by HaloTag technology. *Biocell* **2022,** *46* (8), 1789-801.

285. Machleidt, T., et al., NanoBRET - A novel BRET platform for the analysis of protein-protein interactions. *ACS Chem Biol* **2015,** *10* (8), 1797-804.

286. Peier, A., et al., NanoClick: A high throughput, target-agnostic peptide cell permeability assay. *ACS Chem Biol* **2021,** *16* (2), 293-309.

287. Hakariya, H., et al., Non-genetic cell-surface modification with a self-assembling molecular glue. *Chem Commun (Camb)* **2021,** *57* (12), 1470-3.

288. Kosaka, N., et al., In vivo stable tumor-specific painting in various colors using dehalogenase-based protein-tag fluorescent ligands. *Bioconjug Chem* **2009,** *20* (7), 1367-74.

289. Hong, H., et al., HaloTag as a reporter gene: positron emission tomography imaging with ^{64}Cu-labeled second generation HaloTag ligands. *Am J Transl Res* **2013,** *5* (3), 291-302.

290. Christmann, M., et al., O^6-Methylguanine-DNA methyltransferase (MGMT) in normal tissues and tumors: enzyme activity, promoter methylation and immunohistochemistry. *Biochim Biophys Acta* **2011,** *1816* (2), 179-90.

291. Damoiseaux, R., et al., Synthesis and applications of chemical probes for human O^6-alkylguanine-DNA alkyltransferase. *Chembiochem* **2001,** *2* (4), 285-7.

292. Hotta, T., et al., O^6-alkylguanine-DNA alkyltransferase activity of human malignant glioma and its clinical implications. *J Neurooncol* **1994,** *21* (2), 135-40.

293. Vaidyanathan, G., et al., O^6-3-[^{131}I]iodobenzylguanine: improved synthesis and further evaluation of a potential agent for imaging of alkylguanine-DNA alkyltransferase. *Bioconjug Chem* **2004,** *15* (2), 402-8.

294. Zheng, Q. H., et al., Synthesis and preliminary biological evaluation of radiolabeled O^6-benzylguanine derivatives, new potential PET imaging agents for the DNA repair

protein O6-alkylguanine-DNA alkyltransferase in breast cancer. *Nucl Med Biol* **2003,** *30* (4), 405-15.

295. Wang, J. Q., et al., Synthesis and preliminary biological evaluation of O6-[4-(2-[18F]fluoroethoxymethyl)benzyl]guanine as a novel potential PET probe for the DNA repair protein O6-alkylguanine-DNA alkyltransferase in cancer chemotherapy. *Bioorg Med Chem* **2005,** *13* (20), 5779-86.

296. Kindermann, M., et al., Synthesis and characterization of bifunctional probes for the specific labeling of fusion proteins. *Bioorg Med Chem Lett* **2004,** *14* (11), 2725-8.

297. Keppler, A., et al., Labeling of fusion proteins of O^6-alkylguanine-DNA alkyltransferase with small molecules in vivo and in vitro. *Methods* **2004,** *32* (4), 437-44.

298. Juillerat, A., et al., Directed evolution of O^6-alkylguanine-DNA alkyltransferase for efficient labeling of fusion proteins with small molecules in vivo. *Chem Biol* **2003,** *10* (4), 313-7.

299. Keppler, A., et al., A general method for the covalent labeling of fusion proteins with small molecules in vivo. *Nat Biotechnol* **2003,** *21* (1), 86-9.

300. Keppler, A., et al., Labeling of fusion proteins with synthetic fluorophores in live cells. *Proc Natl Acad Sci U S A* **2004,** *101* (27), 9955-9.

301. Xu-Welliver, M., et al., Role of codon 160 in the sensitivity of human O^6-alkylguanine-DNA alkyltransferase to O^6-benzylguanine. *Biochem Pharmacol* **1999,** *58* (8), 1279-85.

302. Cole, N. B., Site-specific protein labeling with SNAP-tags. *Curr Protoc Protein Sci* **2013,** *73*, 30 1 1- 1 16.

303. Provost, C. R.; Sun, L., Fluorescent labeling of COS-7 expressing SNAPtag fusion proteins for live cell imaging. *J Vis Exp* **2010,** (39).

304. Depke, D. A., et al., A novel ^{18}F-labeled clickable substrate for targeted imaging of SNAP-tag expressing cells by PET in vivo. *Chem Commun (Camb)* **2021,** *57* (77), 9850-3.

305. Li, X., et al., Development of a radiotracer for PET imaging of the SNAPtag. *ACS Omega* **2022,** *7* (9), 7550-5.

306. Stotz, S., et al., Covalent ^{18}F-radiotracers for SNAPTag: A new toolbox for reporter gene imaging. *Pharmaceuticals (Basel)* **2021,** *14* (9).

307. Gautier, A., et al., An engineered protein tag for multiprotein labeling in living cells. *Chem Biol* **2008,** *15* (2), 128-36.

308. Gautier, A., et al., Selective cross-linking of interacting proteins using self-labeling tags. *J Am Chem Soc* **2009,** *131* (49), 17954-62.

309. Wilhelm, J., et al., Kinetic and structural characterization of the self-labeling protein tags HaloTag7, SNAPtag, and CLIPtag. *Biochemistry* **2021,** *60* (33), 2560-75.

310. Shoemaker, R. H., The NCI60 human tumour cell line anticancer drug screen. *Nat Rev Cancer* **2006,** *6* (10), 813-23.

REFERENCES

311. Rybaczek, D., Hydroxyurea-induced replication stress causes poly(ADP-ribose) polymerase-2 accumulation and changes its intranuclear location in root meristems of Vicia faba. *J Plant Physiol* **2016,** *198*, 89-102.

312. Ganz, M., et al., The oncoprotein DEK affects the outcome of PARP1/2 inhibition during mild replication stress. *PLoS One* **2019,** *14* (8), e0213130.

313. Bowden, G. D., et al., Scalable ^{18}F processing conditions for copper-mediated radiofluorination chemistry facilitate DoE optimization studies and afford an improved synthesis of [^{18}F]olaparib. *Org Biomol Chem* **2021,** *19* (32), 6995-7000.

314. Singh, V., et al., Genetically encoded multispectral labeling of proteins with polyfluorophores on a DNA backbone. *J Am Chem Soc* **2013,** *135* (16), 6184-91.

315. Bowden, G. D., et al., A design of experiments (DoE) approach accelerates the optimization of copper-mediated ^{18}F-fluorination reactions of arylstannanes. *Sci Rep* **2019,** *9* (1), 11370.

316. Bowden, G. D., et al., Automated synthesis of [^{18}F]O6-[(4-[^{18}F]fluoro)benzyl]guanine ([^{18}F]pFBG) via [^{18}F]fluorobenzyl alcohol ([^{18}F]4FBnOH) from an optimized copper mediated radiofluorination (CMRF). *Journal of Labelled Compounds and Radiopharmaceuticals* **2019,** *62* (S1), S123-S588.

317. Lewis, C. A., et al., Tracing compartmentalized NADPH metabolism in the cytosol and mitochondria of mammalian cells. *Mol Cell* **2014,** *55* (2), 253-63.

318. Mirrione, M. M., et al., A novel approach for imaging brain-behavior relationships in mice reveals unexpected metabolic patterns during seizures in the absence of tissue plasminogen activator. *Neuroimage* **2007,** *38* (1), 34-42.

319. Logan, J., et al., Distribution volume ratios without blood sampling from graphical analysis of PET data. *J Cereb Blood Flow Metab* **1996,** *16* (5), 834-40.

320. Wilson, T. C., et al., A one-pot radiosynthesis of [^{18}F]PARPi. *J Labelled Comp Radiopharm* **2020,** *63* (9), 419-25.

321. Robert Mach, S. R., Mehran Makvandi, Kuiying Xu, Daniel Pryma Radiolabeled and fluorescent PARP inhibitors for imaging and radiotherapy. 2018.

322. Wang, B., et al., Discovery and characterization of (8S,9R)-5-fluoro-8-(4-fluorophenyl)-9-(1-methyl-1H-1,2,4-triazol-5-yl)-2,7,8,9-te   trahydro-3H-pyrido[4,3,2-de]phthalazin-3-one (BMN 673, talazoparib), a novel, highly potent, and orally efficacious poly(ADP-ribose) polymerase-1/2 inhibitor, as an anticancer agent. *J Med Chem* **2016,** *59* (1), 335-57.

323. Bertucci, F., et al., PARP1 expression in soft tissue sarcomas is a poor-prognosis factor and a new potential therapeutic target. *Mol Oncol* **2019,** *13* (7), 1577-88.

324. Zender, L., et al., Identification and validation of oncogenes in liver cancer using an integrative oncogenomic approach. *Cell* **2006,** *125* (7), 1253-67.

325. Jackson, E. L., et al., Analysis of lung tumor initiation and progression using conditional expression of oncogenic K-ras. *Genes Dev* **2001,** *15* (24), 3243-8.

REFERENCES

326. Friden, M., et al., Identification of positron emission tomography (PET) tracer candidates by prediction of the target-bound fraction in the brain. *EJNMMI Res* **2014,** *4* (1), 50.

327. Stotz, S. Evaluation of novel radiotracers for reporter gene imaging. Master Thesis, Eberhard Karls University Tuebingen, 2019.

328. Blau, M., et al., ^{18}F-fluoride for bone imaging. *Semin Nucl Med* **1972,** *2* (1), 31-7.

329. Cavina, L., et al., Design of radioiodinated pharmaceuticals: structural features affecting metabolic stability towards in vivo deiodination. *European J Org Chem* **2017,** *2017* (24), 3387-414.

330. Zhao, M., et al., Cytochrome P450 enzymes and drug metabolism in humans. *Int J Mol Sci* **2021,** *22* (23).

331. Soret, M., et al., Partial-volume effect in PET tumor imaging. *J Nucl Med* **2007,** *48* (6), 932-45.

332. Seelig, A., P-Glycoprotein: One mechanism, many tasks and the consequences for pharmacotherapy of cancers. *Front Oncol* **2020,** *10*, 576559.

333. Markham, A., Pamiparib: First approval. *Drugs* **2021,** *81* (11), 1343-8.

334. Wang, H., et al., Discovery of pamiparib (BGB-290), a potent and selective poly(ADP-ribose) polymerase (PARP) inhibitor in clinical development. *J Med Chem* **2020,** *63* (24), 15541-63.

335. Molnar, S., et al., The prognostic value of PARP expression in high-grade epithelial ovarian cancer. *Pathol Oncol Res* **2020,** *26* (4), 2549-55.

336. Hopkins, T. A., et al., PARP1 trapping by PARP inhibitors drives cytotoxicity in both cancer cells and healthy bone marrow. *Mol Cancer Res* **2019,** *17* (2), 409-19.

337. Wang, Z., et al., The Wnt signaling pathway in tumorigenesis, pharmacological targets, and drug development for cancer therapy. *Biomark Res* **2021,** *9* (1), 68.

338. Carney, B., et al., Target engagement imaging of PARP inhibitors in small-cell lung cancer. *Nat Commun* **2018,** *9* (1), 176.

339. Tian, X. H., et al., XAV939, a tankyrase 1 inhibitior, promotes cell apoptosis in neuroblastoma cell lines by inhibiting Wnt/β-catenin signaling pathway. *J Exp Clin Cancer Res* **2013,** *32* (1), 100.

340. Bruin, M. A. C., et al., Pharmacokinetics and Pharmacodynamics of PARP Inhibitors in Oncology. *Clin Pharmacokinet* **2022,** *61* (12), 1649-75.

341. Xiong, Y., et al., Pamiparib is a potent and selective PARP inhibitor with unique potential for the treatment of brain tumor. *Neoplasia* **2020,** *22* (9), 431-40.

342. Kruger, A., et al., Real-time monitoring of PARP1-dependent PARylation by ATR-FTIR spectroscopy. *Nat Commun* **2020,** *11* (1), 2174.

343. Rudolph, J., et al., Poly(ADP-ribose) polymerase 1 searches DNA via a 'monkey bar' mechanism. *Elife* **2018,** *7*.

REFERENCES

344. Carlucci, G., et al., Evaluation of [^{18}F]ATRi as PET tracer for in vivo imaging of ATR in mouse models of brain cancer. *Nucl Med Biol* **2017,** *48*, 9-15.

345. Durant, S. T., et al., The brain-penetrant clinical ATM inhibitor AZD1390 radiosensitizes and improves survival of preclinical brain tumor models. *Sci Adv* **2018,** *4* (6), eaat1719.

346. Jucaite, A., et al., Brain exposure of the ATM inhibitor AZD1390 in humans - A positron emission tomography study. *Neuro Oncol* **2021,** *23* (4), 687-96.

347. Radu, C. G., et al., Molecular imaging of lymphoid organs and immune activation by positron emission tomography with a new ^{18}F-labeled 2'-deoxycytidine analog. *Nat Med* **2008,** *14* (7), 783-8.

348. Bunimovich, Y. L., et al., Deoxycytidine kinase augments ATM-Mediated DNA repair and contributes to radiation resistance. *PLoS One* **2014,** *9* (8), e104125.

349. Kim, W., et al., [^{18}F]CFA as a clinically translatable probe for PET imaging of deoxycytidine kinase activity. *Proc Natl Acad Sci U S A* **2016,** *113* (15), 4027-32.

350. Chen, B. Y., et al., [^{18}F]FAC PET visualizes brain-infiltrating leukocytes in a mouse model of multiple sclerosis. *J Nucl Med* **2020,** *61* (5), 757-63.

351. Salas, J. R., et al., [^{18}F]FAC PET selectively images liver-infiltrating CD4 and CD8 T cells in a mouse model of autoimmune hepatitis. *J Nucl Med* **2018,** *59* (10), 1616-23.

352. Laing, R. E., et al., Visualizing cancer and immune cell function with metabolic positron emission tomography. *Curr Opin Genet Dev* **2010,** *20* (1), 100-5.

353. Konstantinopoulos, P. A., et al., A replication stress biomarker is associated with response to gemcitabine versus combined gemcitabine and ATR inhibitor therapy in ovarian cancer. *Nat Commun* **2021,** *12* (1), 5574.

354. Cavalcante, L. D.; Monteiro, G., Gemcitabine: Metabolism and molecular mechanisms of action, sensitivity and chemoresistance in pancreatic cancer. *Eur J Pharmacol* **2014,** *741*, 8-16.

355. Henriksson, S., et al., Distinct mechanistic responses to replication fork stalling induced by either nucleotide or protein deprivation. *Cell Cycle* **2018,** *17* (5), 568-79.

356. Ramakrishnan, N. K., et al., Automated radiosynthesis and preclinical in vivo evaluation of [^{18}F]fluoroethylpuromycin as a potential radiotracer for imaging protein synthesis with PET. *Nuclear Medicine and Biology* **2022,** *114-115*, 71-7.

357. Robbins, P. D.; Ghivizzani, S. C., Viral vectors for gene therapy. *Pharmacol Therapeut* **1998,** *80* (1), 35-47.

358. Liang, M., Oncorine, the world first oncolytic virus medicine and its update in china. *Curr Cancer Drug Tar* **2018,** *18* (2), 171-6.

359. Cashman, S. M., et al., Adenovirus-mediated delivery of Factor H attenuates complement C-3 induced pathology in the murine retina: a potential gene therapy for age-related macular degeneration. *J Gene Med* **2015,** *17* (10-12), 229-43.

360. Hocquemiller, M., et al., Adeno-associated virus-based gene therapy for CNS diseases. *Human Gene Therapy* **2016,** *27* (7), 478-96.

REFERENCES

361. Mathiesen, S. N., et al., CNS Transduction Benefits of AAV-PHP.eB over AAV9 Are Dependent on Administration Route and Mouse Strain. *Mol Ther-Meth Clin D* **2020,** *19*, 447-58.

7. LIST OF TABLES

8. LIST OF FIGURES

9. DECLARATION OF CONTRIBUTIONS

This work was written by the author in its entirety.

Large parts of this work are already published in peer-reviewed journals (see section 10) or are in preparation to publication (HaloTag- and CLIPTag-related chemistry, *in vitro* and *in vivo* studies). In the publications relevant to this work (see chapter 10, 1.-3.), the contributions are listed in detail in the publication.

Compounds and synthesis strategies were designed and executed by Dr. Andreas Maurer, Dr. Gregory D. Bowden and Dr. Jonathan M. Cotton. Organic synthesis and radiosynthesis, including characterization of the compounds for publication, were performed by Dr. Gregory D. Bowden, Dr. Jonathan M. Cotton, Dr. Andreas Maurer, and Johannes Kinzler. Routine radiotracer syntheses were carried out by Elena Kimmerle and Ramona Stremme, who also performed the HPLC runs during the serum stability and *in vivo* metabolite analysis.

The reporter constructs were designed by Dr. Andreas Maurer. The *in vitro* and *in vivo* studies were planned, executed and analyzed by the author (partially under the supervision of Dr. Andreas Maurer) with the following exceptions: The HEK-reporter cell lines were generated by Natalie Hermann who also supported some *in vitro* studies. Animal experiments were in part supported by the technical assistants of the Werner Siemens Imaging Center (Linda Schramm, Natalie Hermann, Maren Harant, Miriam Owczorz, Sandro Aidone, Matthias Dahms, and Siaolan Huang). The *in vivo* metabolite analysis was performed together with Sabrina Haas and analyzed by the author. The author received advice on the analysis of the AAV brain studies from Sabrina Haas and Prof. Dr. Kristina Herfert. *Ex vivo* immunofluorescence staining was performed by Birgit Fehrenbacher at the Department of Dermatology, University Hospital Tuebingen. Light sheet microscopy was performed in cooperation with Gina Dunkel who also analyzed the data (under supervision of Prof. Dr. Bettina Weigelin).

Statistical analyses were performed by the author with GraphPad Prism Version 9 using standard statistic tests (t-test, ANOVA).

10. PEER-REVIEWED SCIENTIFIC PUBLICATIONS

1. Bowden, G.D., Stotz, S., Kinzler, J., Geibel, C., Lämmerhofer, M., Pichler, B.J., Maurer, A. **DoE optimization empowers the automated preparation of enantiomerically pure [^{18}F]talazoparib and its in vivo evaluation as a PARP radiotracer.** J Med Chem 64(21):15690-15701 (2021)
doi: 10.1021/acs.jmedchem.1c00903

2. Stotz, S., Kinzler, J., Nies, A.T., Schwab, M., Maurer, A. **Two experts and a newbie: [^{18}F]PARPi vs [^{18}F]FTT vs [^{18}F]FPyPARP-a comparison of PARP imaging agents.** Eur J Nucl Med Mol Imaging (2021)
doi: 10.1007/s00259-021-05436-7.

3. Stotz, S., Bowden, G.D., Cotton, J.M., Pichler, B.J., Maurer, A. **Covalent ^{18}F-radiotracers for SNAPTag: a new toolbox for reporter gene imaging.** Pharmaceuticals (Basel), 14(9):897. (2021)
doi: 10.3390/ph14090897

4. Stotz, S., Bleher, D., Kalbacher, H., Maurer, A. **Grassystatin-derived peptides selectively inhibit cathepsin E and have low affinity to cathepsin D.** Biochem Biophys Res Commun, 527 238 (2020).
doi: 10.1016/j.bbrc.2020.04.070

5. Aichem, A., Anders, S., Catone, N. Roessler, P., Stotz, S., Berg, A., Schwab, R., Scheuermann, S., Bialas, J., Schuetz-Stoffregen, MC. Schmidtke, G., Peter, C., Groetrupp, M., Wiesner, S. **The structure of the ubiquitin-like modifier FAT10 reveals an alternative targeting mechanism for proteasomal degradation.** Nat Commun 9, 3321 (2018).
doi: 10.1038/s41467-018-05776-3

11. CONTRIBUTIONS TO SCIENTIFIC MEETINGS

9.1 Oral Presentations

<u>Stotz, S.</u>, Buss, S., Kinzler, J., Herfert, K., Pichler, B.J., Maurer, A. **A Covalent ^{18}F-labeled Radiotracer for Reporter Gene Imaging of Viral Gene Transfer in the Brain.** European Molecular Imaging Meeting (2022, Thessaloniki, Greece)
Young Investigator Award Runner-up

<u>Stotz, S.</u>, Bowden, G.D., Buss, S., Dunkel, G., Weigelin, B., Herfert, K., Pichler, B.J., Maurer, A. **[^{18}F]*p*FBC is a Covalent CLIPTag Radiotracer for PET Reporter Gene Imaging of Viral Gene Transfer in the Murine Brain.** World Molecular Imaging Conference (2022, Miami, FL, USA)
Young Investigator Award Runner-up

<u>Stotz, S.</u>, Bowden, G.D., Buss, S., Dunkel, G., Weigelin, B., Herfert, K., Pichler, B.J., Maurer, A. **[^{18}F]*p*FBC is a Covalent CLIPTag Radiotracer for PET Reporter Gene Imaging of Viral Gene Transfer in the Murine Brain.** European Molecular Imaging Meeting (2023, Salzburg, Austria)
Same abstract and title as WMIC 2022 due to invitation by WMIS & ESMI

9.2 Poster Presentations

<u>Stotz, S.</u>, Pichler, B.J., Maurer, A. **Accelerating Neuroimaging Research: [^{18}F]FB-HTL as a Reporter Gene Tracer with Potential for *in vivo* Brain Imaging.** European Molecular Imaging Meeting (2020, virtual)

<u>Stotz, S.</u>, Kinzler, J., Pichler, B.J., Maurer, A. **Next-Generation PARP Imaging with [^{18}F]FPyPARP – A Comparison with the Benchmark Radiotracers [^{18}F]PARPi and [^{18}F]FTT.** World Molecular Imaging Conference (2020, virtual)

<u>Stotz, S.</u>, Bowden, G.D., Cotton, J.M., Pichler, B.J., Maurer, A. **Characterization of Three Novel Covalent ^{18}F-Radiotracers for *In Vivo* Nuclear Imaging of SNAPtag as a Novel Toolbox for Reporter Gene Imaging.** European Molecular Imaging Meeting (2021, Göttingen, Germany)

CONTRIBUTIONS TO SCIENTIFIC MEETINGS

<u>Stotz, S.</u>, Bowden, G.D., Pichler, B.J., Maurer, A. **Preclinical Evaluation of [^{18}F]Talazoparib as Next Generation PARP Imaging Agent.** World Molecular Imaging Conference (2021, virtual)

<u>Stotz, S.</u>, Buss, S., Kinzler, J., Herfert, K., Pichler, B.J., Maurer, A. **Imaging of AAV-mediated Gene Transfer in the Brain using a Novel PET Reporter Gene Tracer.** International Symposium on Radiopharmaceutical Sciences (2022, Nantes, France)

<u>Stotz, S.</u>, Buss, S., Kinzler, J., Herfert, K., Pichler, B.J., Maurer, A. **PET Imaging of Viral Gene Transfer in the Brain with a Covalently Binding ^{18}F-labeled HaloTag Ligand.** Turku PET Symposium (2022, Turku, Finland)

<u>Stotz, S.</u>, Bowden, G.D., Pichler, B.J., Maurer, A. **Systematic Side-by-Side Comparison of [^{18}F]Olaparib and [^{18}F]Talazoparib as PARP Imaging Agents in an HR-Deficient Breast Cancer Xenograft Model. '**Image-Guided and Functionally Instructed Tumor Therapies' iFIT2023 (2023, Zell am See, Austria)

<u>Stotz, S.</u>, Bowden, G.D., Kinzler, J., Pichler, B.J., Maurer, A. **Systematic Side-by-Side Comparison of Five Different PARP Radiotracers in an HR-Deficient Breast Cancer Xenograft Model.** International Symposium on Radiopharmaceutical Sciences (2023, Honolulu, Hawaii, USA)